

MSc Thesis

# Development of a Robust and Time Efficient Modelling Strategy for the Analysis of As-Manufactured CPVs

Chiara Ardemani



# MSc Thesis

## Development of a Robust and Time Efficient Modelling Strategy for the Analysis of As-Manufactured CPVs

by

Chiara Ardemani

For obtaining the degree of Master of Science in  
Aerospace Engineering - Structures and Materials  
at the Delft University of Technology.

Student number: 4429575  
Project duration: January 1, 2021 – September 24, 2021  
Supervisors: Dipl. Ing. M. Nebe cellcentric GmbH & Co.KG  
Prof Dr. Ir. J.M.J.E. van Campen Delft University of Technology

*This report is confidential*

# Preface

This document practically and symbolically encloses all that these six years have been for me: lots of work, lots of satisfaction, and lots of composites. Without a doubt, my first *thank you* goes to this great institution that some wise Dutch king decided to locate in the idillic town on Delft. Today I graduate as Aerospace Engineer, but to speak truthfully the greatest lessons I have learnt here go far beyond this title. Delft University of Technology has taught me the value of curiosity, dedication, entrepreneurship, internationality, collaboration, forward thinking and fun.

Throughout my time in Delft, I have met an incredible amount of capable and inspiring professionals. One in particular has accompanied me since the very first day. Prof. Julien van Campen was there when I stepped into Lecture Room A for my first Statics lecture, and he supervised my bachelor graduation project. He recommended me for an internship at Daimler AG, and he is here today, as I specialize in Aerospace Structures and Materials. I am grateful for the unmatched support he has provided throughout this endeavor and for the many opportunities he has opened for me. I am glad to finish this chapter guided by an expert that I deeply value both on a professional and a personal level.

Unarguably one of the most intense phases of my studies started when I joined the Hydrogen Tank Team at Daimler AG (later at cellcentric GmbH). Here, I was introduced to outstanding specialists that have set a strong example for me inside and outside the office. My greatest *thank you* is reserved for Martin Nebe, for supervising my research and teaching me how to work with professionalism. I value his example immensely, because he has shown me what it means to be a knowledgeable engineer, a dedicated leader, and a genuinely inspiring person. *Thank you* also to Clemens Braun - I have truly valued his technical insight, and appreciated greatly his authentic and sharp demeanor. A special *thanks* goes to my colleague Antonio Johman - a wonderful person and a good friend. The knowledge he shared all along and his daily moral support have helped me more than he may realize. Not to mention, the existential topics of conversation crossing our overthinking minds have made my days in Stuttgart incredibly stimulating. Finally, a *thank you* to the students that have been here before and with me - Daniel, Ana, Tom, Benoit, Alex, Eleonora, Alejandro and Antonio. As last man standing, I am honored to end what you guys started.

In this adventure called University, I met some of the most stellar companions one could ever hope to find. Probably unconsciously, they have contributed to this work and to all that came before to the greatest extent. I am grateful to my international friends, for quickly becoming my family in the Netherlands; to my Delft Hyperloop team, that taught me that there is nothing that hard work and good collaboration cannot achieve; to my housemates at the Bagijnhof and at the Neckartor, who gave me inconditionate brotherly and sisterly support; to my friends in Stuttgart, who made Germany my home and the place where I want to settle; finally, to my *HB4B*, an inspiring group of brilliant, fun and warm-hearted women. To all of them, *thank you* also for putting up with my never-ending drama.

One of the most valuable lessons I have learnt far from my beloved Italy is how lucky I am to be part of team Ardemani. *Team* is the word I want to use because rarely I have had the chance to experience similar levels of mutual support and respect. I am grateful to the persons I admire the most, Filippo and Giulia, for the spectacular examples they show me every day. I never stop looking up to their success, their ambitions, and their caring spirits. Finally, the most special *thank you* goes to my parents, Paola and Antonio, for always supporting my impulsive decisions, for teaching me that there is no distance that rooted relationships cannot bridge, and for showing me what it means to bend over backwards for the people you love. Needless to say, I miss home every day.

While being fully aware that a page is not nearly enough to show gratitude to all the great people I have met along this journey, it is time to move on to the next chapter of my life (and of this document).

Thank y'all, it's been a wonderful odyssey.

Chiara Ardemani  
Delft, 24 September 2021

# Abstract

The recent drive towards carbon-neutral transportation has led the automotive industry towards the development of fuel cell electric vehicles (FCEV). A crucial part of these systems is the hydrogen storage solution. This is often a Type IV composite pressure vessel (CPV), where gaseous hydrogen is compressed to 70 MPa according to automotive specifications. CPVs are among the most sophisticated composite structures and a thorough understanding is yet to be achieved. Carbon fiber reinforced polymer (CFRP) is usually selected for these vessels, as it ensures high mechanical performance at low weight. CFRP is however expensive, and minimizing its usage is fundamental to lower the costs of the tank system.

This research aims to contribute to the understanding of CPVs by developing an analysis strategy which captures the mechanical response of the vessels during pressurization in a robust and time-efficient manner. The study is performed in collaboration with cellcentric GmbH, where a unique experimental setup for pressurization and burst testing allows to validate the numerical results. The techniques used to gather this data include stripe light projection and digital image correlation (DIC).

The study initially simulates the implications of the manufacturing process on the geometry and material composition of CPVs. An analytical adjustment to the vessel architecture replicates the effects of compaction during filament winding. Furthermore, modifications to the predicted vessel contour ensure that the complex dome geometry is represented realistically. The adjusted vessel specifications are then used to set up a finite element (FE) model in the Abaqus software. The model generation is fully automated, allowing the analysis of a variety of configurations. Several numerical adjustments are implemented to minimize the computational expenses of the simulation and maximize its accuracy. The model size is reduced drastically by decreasing the angle of revolution by which the laminate contour is rotated to generate the part. For all the results presented in the document, this is set to 5 degrees. The axial and through-thickness discretization is adjustable according to the desired resolution. In this report, the vessel is discretized axially in 242 points. A per-ply-group discretization is chosen to capture most through-thickness effects at low computational time.

Within the Abaqus environment, two models are developed. The first one uses a solid element formulation. This element type is inherited from previous studies, granting a direct comparison with the pre-existing benchmark. The second one uses a continuum shell element formulation, which allows to simulate efficiently material degradation due to damage according to Hashin Rotem failure criterion. The performance of the two frameworks is evaluated for three vessel configurations with regards to three main parameters. Firstly, the predicted outer strains at 105 MPa internal pressure are compared to the experimental data. Then, the burst pressure is estimated from the stress-state extracted from Abaqus at the same pressure level. In this case, the Puck and the maximum stress failure criteria are applied to extrapolate linearly the burst pressure based on a first ply failure approach. This considers tensile fiber fracture as only possible failure mode. Again, experimental data is used to check the validity of the method. Finally, the computational time is assessed.

This approach leads to a twofold modelling strategy, that can be tuned according to the needs of the user. The solid element model provides reasonably accurate results at very low computational times (lower than 5 minutes for all investigated cases) and it is useful in preliminary design phases. The continuum shell element model leads to much more accurate results and insights on the failure sequence. However, it comes at higher computational costs (between 30 and 80 minutes for the investigated cases). This framework is best implemented within detailed design phases. In both cases, the accuracy and computational efficiency of the model exceeds greatly that of the pre-existing benchmark. Both modelling strategies are able to predict the trends in deformational behavior of the CPV closely. For the three vessel configurations in analysis, the discrepancy between the simulation results and the experimental data does not exceed 8% for both outer tangential and meridional strains. Failure is also predicted realistically, both in the dome and in the cylinder. The discrepancy in this case is lower than 10% for all configurations. One of the most remarkable achievement of the research is the successful prediction of dome burst, anticipated with an accuracy of 99%. Dome burst is rarely investigated due to the high complexity of the geometry and the material composition of the region.

In future research the model may be applied to a wider set of laminate configurations and vessel geometries to further scrutinize its validity for different scenarios. Particular emphasis should be put towards the dome laminate architecture as the varying layer orientations, layer thicknesses and material properties complicate an accurate numerical reproduction of this region.



# Contents

1	Introduction	1
1.1	Composite Pressure Vessels in the Automotive Industry	2
1.2	Manufacturing of Composite Pressure Vessels	4
1.2.1	Introduction to Filament Winding	4
1.2.2	Filament Path Definition and Thickness Accumulation	6
1.2.3	Effects of Fiber Tension	8
1.3	Research Focus and Thesis Structure	11
2	Research Framework	13
2.1	Analysis Strategies for CPVs	13
2.1.1	Analytical Models	14
2.1.2	Numerical Models	16
2.1.3	Previous Research at cellcentric GmbH	17
2.2	Experimental Setup at cellcentric GmbH	18
2.3	Overview of Layups in Analysis	20
2.4	Research Questions and Objectives	21
3	Computationally Efficient Modelling of CPVs	23
3.1	Model Specifications	24
3.2	Model Size Determination	25
3.2.1	Setup for Model Size Reduction	25
3.2.2	Method for the Adjustment of the Model Geometry	26
3.2.3	Relevance of the Model Size Reduction Approach	27
3.3	Partitioning Methods	28
3.3.1	Through-Thickness Partitioning	29
3.3.2	Axial Partitioning	29
3.3.3	Evaluation of Partitioning Strategy	30
3.4	Overview of Modelling Method	30
4	Geometry and Material Definition of CPVs	33
4.1	Geometrical Definition of Vessel Thickness	33
4.1.1	Description of Input Geometry	33
4.1.2	Layer Re-Arrangement at Turnaround Points	35
4.1.3	Comparison with Measured Vessel Contour	37
4.1.4	Evaluation of Vessel Geometry Adjustments	39
4.2	Material Properties Definition	39
4.2.1	Effect of Compaction on the Definition of Material Properties	40
4.2.2	Engineering Approach for the Adjustment of Per-Ply Properties	41
4.2.3	Validation Approach	44
4.2.4	Evaluation of the Procedure for the Correction of Material Properties	46
4.3	Propagation of Damage	49
4.3.1	Mathematical Description of Hashin Rotem Failure Criterion	49
4.3.2	Implementation of Damage Propagation in Abaqus	51
5	Results and Assessment of Model Performance	53
5.1	Performance of the Solid Model	54
5.1.1	Prediction of Deformational Behavior	54
5.1.2	Considerations on Stresses and Estimation of Burst	56
5.2	Performance of the Continuum Shell Model	61
5.2.1	Prediction of Deformational Behavior	61
5.2.2	Considerations on Stresses and Estimation of Burst	64

---

5.3	Evaluation of Computational Time . . . . .	74
6	Model Applicability for the Design of CPVs . . . . .	76
6.1	A Twofold Potential . . . . .	76
6.2	Adjustment of Vessel Properties on Different Vessel Configurations. . . . .	78
6.3	Minimizing Computational Time . . . . .	80
7	Conclusions and Outlook . . . . .	82
7.1	Summary . . . . .	82
7.1.1	Numerical Framework . . . . .	82
7.1.2	Results and Applicability. . . . .	83
7.2	Conclusions. . . . .	83
7.3	Recommendations for Future Research. . . . .	85
A	Appendix: Mesh Refinement Study . . . . .	87
B	Appendix: Investigation on Matrix-Dominated Stresses . . . . .	89
C	Appendix: Investigation on Per-ply Failure Indices and Considerations on Burst . . . . .	91
	Bibliography . . . . .	93

# Nomenclature

## Abbreviations

BEV	Battery Electric Vehicles
CDM	Continuum Damage Mechanics
CFRP	Carbon Fiber Reinforced Polymer
CLT	Classical Lamination Theory
CPV	Composite Pressure Vessel
CT	Computed Tomography
DIC	Digital Image Correlation
EPA	Environmental Protection Agency
FE	Finite Element
FEA	Finite Element Analysis
FCEV	Fuel Cell Electric Vehicles
ICE	Internal Combustion Engine
OEM	Original Equipment Manufacturer
R&D	Research and Development
UMAT	User-defined material subroutine in Abaqus
USDFLD	User-defined field subroutine in Abaqus

## Latin Symbols

$A$	Extensional stiffness matrix	$[N/m]$
$a$	Major semi-axis of ellipse	$[m]$
$B$	Bending-extension coupling stiffness matrix	$[N]$
$B$	Bandwidth	$[m]$
$b$	Minor semi-axis of ellipse	$[m]$
$C$	Number of wound circuits	$[-]$
$D$	Bending stiffness matrix	$[Nm]$
$d$	Damage variable	$[-]$
$E$	Elastic modulus	$[Pa]$
$E_r$	Radial elastic modulus	$[Pa]$
$E_\theta$	Tangential elastic modulus	$[Pa]$
$F$	Failure index	$[-]$
$F_n$	Normal load on the lamina during winding	$[N]$
$F_t$	Tension load on the lamina during winding	$[N]$
$f$	Shear factor in Hashin Rotem failure criterion	$[-]$
$f_n$	Normal load on filament	$[N]$
$f_r$	Resultant force on filament	$[N]$
$f_s$	Transverse force on filament	$[N]$
$h$	Cylinder wall thickness	$[m]$
$L_c$	Characteristic element length	$[m]$
$M$	Artificial damage operator	$[-]$
$M$	Moment	$[Nm]$
$m$	Ply cross-sectional area	$[m^2]$
$m_R$	Count of pseudo-ply in cylinder	$[-]$
$N$	Load	$[N]$
$N_s$	Meridional normal force	$[N]$
$N_t$	Circular normal force	$[N]$

$N_\theta$	Tangential loading	[N]
$N_\phi$	Longitudinal loading	[N]
$n_R$	Total number of pseudo-plyies	[-]
$n_{tow}$	Number of tows	[-]
$p$	Internal pressure	[Pa]
$Q$	Stiffness matrix	[Pa]
$R$	Cylinder radius	[m]
$r$	Radial coordinate with respect to origin	[m]
$r_b$	Radius at one bandwidth from turn-around point	[m]
$r_{2b}$	Radius at two bandwidths from turn-around point	[m]
$r_c$	Radius at cylinder-dome transition	[m]
$r_o$	Radius at turnaround point	[m]
$S$	Shape functions	[-]
$S^L$	Shear strength of the lamina	[Pa]
$t$	Laminate thickness	[m]
$t_c$	Cylinder thickness	[m]
$t_d$	Dome thickness	[m]
$t_p$	Tow thickness	[m]
$t_r$	Ply thickness	[m]
$u_r$	Radial displacement with respect to the vessel's longitudinal axis	[m]
$v_f$	Fiber volume fraction	[%]
$W_{tow}$	Weight of one tow	[kg]
$X$	Longitudinal strength property	[Pa]
$Y$	Transverse strength property	[Pa]
$Z$	Ply through-thickness location with respect to the liner	[m]

## Greek Symbols

$\alpha$	Fiber orientation angle	[deg]
$\alpha_0$	Fiber orientation angle in cylinder	[deg]
$\gamma$	Curvature of elliptical dome	[m <sup>-1</sup> ]
$\delta^0$	Initial displacement for damage initiation	[m]
$\delta^f$	Displacement at final failure	[m]
$\epsilon$	Strain	[-]
$\epsilon_s$	Meridional strain	[-]
$\epsilon_\phi$	Tangential strain	[-]
$\epsilon^0$	Midplane strain in classical lamination theory	[-]
$\kappa$	Laminate curvature	[m <sup>-1</sup> ]
$\lambda$	Coefficient of slippage	[-]
$\nu$	Poisson ratio	[-]
$\nu_r$	Poisson ratio in the radial direction	[-]
$\nu_\theta$	Poisson ratio in the tangential direction	[-]
$\rho_f$	Fiber density	[kg/m <sup>3</sup> ]
$\sigma$	Normal stress on fibers	[Pa]
$\sigma_r$	Stress on fibers in the radial direction	[Pa]
$\sigma_\theta$	Stress on fibers in the tangential direction	[Pa]
$\tau$	Shear stress on fibers	[Pa]

# Introduction

Climate change is a reality that requires immediate action. The quick response of the industry to this emergency is fundamental to limit the damage of human action on the environment and reduce global emissions. This growing awareness has manifested itself in an expanding social movement demanding for meaningful effort for a sustainable future. Industrial parties must react promptly to remain competitive on the market.

The automotive industry has gradually started to explore several options in terms of vehicle propulsion, with the purpose to eventually embrace the transition towards carbon-neutral means of transportation. This does not only pose an interesting alternative to partly solve the issue of climate change, but also a convenient solution to avoid the extreme fluctuations of oil prices. In this context, most original equipment manufacturers (OEMs) are investing on the hybridization and electrification of vehicle fleets. Battery electric vehicles (BEVs) have therefore become a largely implemented alternative to regular internal combustion engine (ICE) vehicles. In general, an electric powertrain has the benefit of achieving high torque through a highly efficient conversion of chemical energy into electrical energy, making the performance of BEVs virtually competitive with that of the widely used ICEs.

Nevertheless, BEVs have several limitations: firstly, the substantial weight of commercial batteries, necessary to achieve the relatively long ranges that the automotive industry requires. The average energy density of currently available battery packs does not exceed 0.15 kWh/kg, translating to a required battery weight of 650 kg to achieve a range of 500 km on a 180Wh/km power consumption. Therefore, batteries of large power capacity are rather unrealistic. Furthermore, commercial batteries typically have slow recharging times which limit the applicability of BEVs to short-distance travel. To give an example, a discharged 75kWh Tesla Model S from 2019 would require 21 to 27 hours to charge to full capacity, using a commercial 3.6 kW plug [1]. Although, the charging time can be reduced significantly to approximately 30 minutes when a Tesla fast-charging socket is used, the slow charging capabilities of commercial batteries has led the automotive industry to favor the implementation of BEVs only for private transportation, rather than commercial movement of goods.

The impact of the trucking industry on the climate should however not be underestimated. To put things in perspective, according to a statistic released by the Environmental Protection Agency (EPA) in 2018, the medium- and heavy- duty trucks constitute only 1% of the traffic on American highways, and yet they contribute to more than 23% of the greenhouse gas emission that the transportation sector is responsible for [2]. The applicability of BEVs only to limited ranges has important implications for the trucking industry, where BEVs are intuitively only a valid alternative to ICE vehicles for short-distance travels. As consequence, a different long-range solution must be found to limit the large impact of the trucking industry on the climate. A valid alternative to partly mitigate this issue is offered by hybrid vehicles that combine batteries to ICEs. Hybrid vehicles benefit from the advantages of ICEs over long distances, without giving up the convenience of electric drivetrains on short ranges. Nevertheless, the efficacy of hybrid vehicles on the reduction of emissions is intuitively only marginal.

A more interesting solution is offered by fuel cell electric vehicles (FCEVs), mainly thanks to their high gravimetric energy density and their faster refueling possibility. As introduced by Ehsani et al. [3], the fuel cell technology relies on an electrical powertrain fed by the output of the electromechanical process which occurs in a galvanic cell. Hydrogen, which serves as fuel, is provided to the anodic side of the cell, causing the

release of free electrons. This creates a potential difference within the system, which generates a voltage and therefore an electric flow similar to that of a chemical battery.

Within the fuel cell system, hydrogen can be stored in liquid or gaseous form. In the first case, storage is attained under cryogenic conditions, due the low volumetric energy density of hydrogen at room temperature. A more commonly used solution implies the storage of compressed gaseous hydrogen, achieved similarly as for the already well-established compressed natural gas (CNG). In this context, pressurizing hydrogen is necessary due to its low density at atmospheric pressure and temperature, approaching 0.09 g/L. In fact, as approximately 1 kg of fuel is needed every 100 km of range for regular passenger cars, the introduced hydrogen needs to be highly pressurized to store an adequate amount of fuel and therefore achieve significant ranges. This becomes even more relevant for trucks, for which the fuel consumption ranges between 8 and 10 kg every 100 km.

High levels of pressurization, however, constitute a challenge for the design of the fuel cell system. Compressed hydrogen is explosive, and a robust tank is needed to withstand the high loads imposed by the internal pressure and guarantee the maximum safety of the vehicle. The purpose of this work is therefore to investigate this complex loading condition and contribute to the understanding of pressure vessels, to ensure high reliability at minimum cost. With the aim to provide an overview of the research framework and its scope, a summary of the evolution of pressure vessels in the automotive industry is presented in the next section. This is followed by a description of the manufacturing method suitable for their production. Finally, a brief summary of the structure of this thesis is provided to allow the reader to familiarize with the document.

## 1.1. Composite Pressure Vessels in the Automotive Industry

Within the automotive sector, pressure vessels must comply with a series of requirements. Firstly, given the proximity of the tank to the passengers and the strict laws that regulate the automotive industry, pressure vessels shall ensure maximum safety. To this purpose, it is important that they are completely airtight, as hydrogen is notoriously flammable [4] and any leak could potentially endanger the passengers. Secondly, they shall provide the necessary structural soundness to withstand the high internal pressure loads, without causing massive weight increase to the vehicle. This would inherently lead to a higher fuel consumption. Thirdly, they shall allow for maximum storage volume, as intuitively the higher the capacity of the tank system, the longer the achievable range of the vehicle. Finally, they shall be cheap, such that FCEVs remain competitive on the market and can be deemed convenient as compared to their ICE counterpart.

The geometry and material of the tank are determined based on these requirements. The structure of the pressure vessels developed within the automotive industry typically includes a cylindrical section confined by two close-to-spherical end-caps, as shown in the example in Figure 1.1. This geometry is chosen as a space-efficient extension of the fully-spherical alternative, convenient from a loading perspective as it guarantees the sole development of membrane loads [5]. At the same time, it allows for an increase in volumetric capacity, thanks to the elongated cylindrical main body.

The shape of the end-caps is selected according to the application of the vessel, the materials used and the geometry of the central structure. Theoretically, their shape can range from flat end-caps to hemispherical domes. The former causes high stress concentrations and bending moments at the cylinder edge. On the other hand, the latter is particularly inconvenient in terms of space efficiency, as it occupies a rather significant volume with respect to the internal capacity that it offers. Therefore, an ellipsoidal shape is usually preferred as compromise between the formerly explained solutions [5, 6]. This option features a much more gradual change in geometry compared to the flat end-caps, while ensuring higher storage volume compared to the hemispherical domes.

Depending on the maturity of development, the purpose of the application and the structural requirements of the storage solution, different vessel types have been explored in the automotive sector [8, 9]:

- **Type I** : Consist of a fully metallic pressure vessel;
- **Type II** : Consist of a metallic pressure vessel locally reinforced by composite material in the cylindrical section;
- **Type III**: Consist of a composite laminate structure wound around a metallic gas-sealing liner;
- **Type IV**: Consist of a composite laminate structure wound around a polymeric gas-sealing liner;
- **Type V**: Consist of a composite pressure vessel without liner.

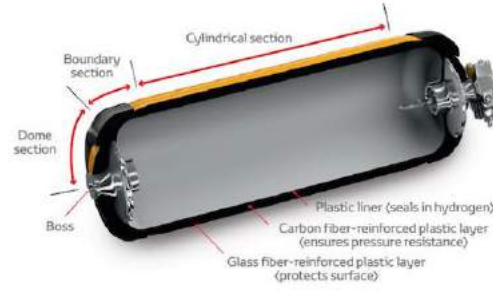


Figure 1.1: Overview of pressure vessel sections, from [7].

A graphical representation of the listed pressure vessel types is presented in Figure 1.2 [10]. Despite being designed for similar loading conditions, the pressure vessel types progressively decrease in mass while increasing in percentage use of composite material and structural complexity.

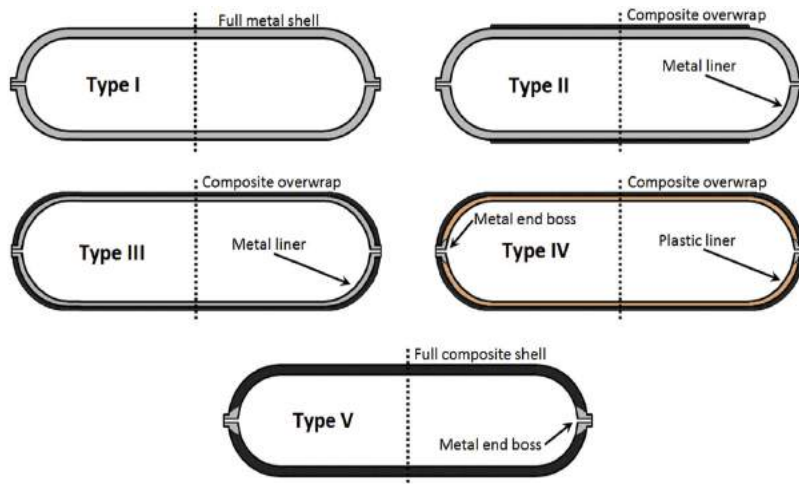


Figure 1.2: Overview of vessel types according to their structural design, from [11].

Type I and Type II pressure vessels have been implemented in the transportation industry prior to the advent of FCEVs as a feasible solution for the storage of Compressed Natural Gas (CNG). CNG offers a valid alternative to regular combustion engines thanks to lower emissions and up to 50% lower operating costs [9]. As gaseous hydrogen, CNG is stored at high pressures, requiring an infrastructure similar to that of FCEVs. Therefore, when FCEVs were first introduced, the option of implementing the same system was logically investigated. At later development stages, the designs of Type III and Type IV pressure vessels have been further refined for hydrogen storage and are now the most mature level of technology in mobile applications. These types of vessels include an appropriate gas-sealing liner which sets the general vessel shape and prevents leakage of gaseous material [9]. A composite reinforcement is then used to guarantee the structural robustness of the tank system. Type V pressure vessels are currently only used for aerospace applications due to their excessive costs often unreachable within the automotive sector.

During pressurization, the vessel structure expands, generating significant tensile stresses. These dominate the loading on the vessel and determine its mechanical response. In this context, the choice of carbon fiber reinforced polymer (CFRP) as reinforcement finds its reasoning, as its tensile strength to weight ratio exceeds of about ten times that of steel. However, raw carbon fiber is expensive, making the cost of CPVs particularly elevated. In fact, the material cost makes up for 60 to 80% of the total vessel costs depending on the production volume [12], mainly due to the specific pre-processing procedures required to manufacture raw CFRP. It is therefore clear that minimizing its use would lead to a cost-efficient hydrogen storage solution.

Within automotive regulations, the performance of CPVs is assessed in terms of burst pressure, or in other words the maximum pressure reached before the laminate structure fails, causing hydrogen dispersion. According to the Global Technical Regulation GTR13 [13], a composite pressure vessel can be certified only



when its burst pressure exceeds the critical value of  $R \cdot p_{operating}$ . Here,  $R$  is the required ratio between minimum burst pressure and nominal working pressure, typically ranging between 2.25 and 3.5 depending on the vessel type, and  $p_{operating}$  is the nominal working pressure, conventionally set at 70 MPa. In addition, CPVs are subjected to impact testing to prove the vessel resistance to perforation. It should be noted that for every configuration, at least 3 samples must be tested to prove the safety of the design.

Among other tests, each manufactured CPV also has to endure end-of-line pressurization testing. This is meant to prove its capabilities during regular operation, as it requires the vessel to hold a pressure 1.4 times higher than the nominal working pressure for 30 s [14].

Typically, the burst pressure requirement dictates the main design parameters, as the high internal pressure loading immediately prior to burst causes critical stress states within the vessel laminate structure [15]. Therefore, most structural optimization studies are based on achieving the required burst pressure while using the lowest amount of material. For this purpose, appropriate understanding of the structural response is absolutely necessary to achieve structural soundness at minimum cost.

## 1.2. Manufacturing of Composite Pressure Vessels

Given their convenient axisymmetric geometry, CPVs are usually manufactured by means of filament winding. To properly understand the mechanical response of the vessel, this manufacturing process must be carefully analysed, as it affects the architecture of the composite laminate significantly. Filament winding has been used for the manufacturing of fiber reinforced structures since the second half of the 20<sup>th</sup> century for multiple reasons. First of all, it allows for the application of continuous fiber filaments on curved surfaces. Continuous fibers are the strongest type of reinforcement when loaded longitudinally, and can be oriented to match and carry the loading state of the structure [16]. Furthermore, filament winding can be largely automated, allowing for low labour costs and high reproducibility [17]. In the next sections, the filament winding procedure and its effects on the final vessel architecture are described in detail.

### 1.2.1. Introduction to Filament Winding

In filament winding, narrow tows of composite material under tension are passed through an eyelet and deposited on a polymeric liner. The process can be performed by means of a portal machine or with the aid of a robotic system. The first features a rotating and translating eyelet moving alongside the rotating liner. The second, on the other hand, consists of a rotating eyelet and a translating and rotating liner. In other words, the difference between the two methods resides in the translating movement, which is performed by the eyelet in the first case and by the liner in the second. In any case, the rotation of the eyelet allows to tune the orientation of the fibers on the mandrel and distribute their strength and stiffness as needed. The movement of the mandrel ensures full fiber coverage over its outer surface [17]. Different filament winding machines may allow rotations around two, three or six axis, progressively increasing the flexibility of the process.

Another way of differentiating between the winding processes is based on the stage of impregnation of the fiber component. In dry winding the fibers are impregnated prior to the winding process, and bought from the material manufacturer in the form of ready-to-use prepreg spools. On the other hand, in wet winding, tows of dry fibers are passed through a resin bath directly prior to winding. This is schematically depicted in Figure 1.3, which features an original portal axis machine. Within industrial settings, wet winding is often preferred, as it relies on generally cheaper raw materials which do not require the high-quality processing necessary to make prepreg rolls. Wet winding has also the advantage of not involving any specific infrastructure for the storage of the raw material, inherently lowering the overall manufacturing costs of CPVs. The dry fibers for wet winding can conveniently be stored at room temperature without issue, and the resin system does not begin its hardening curing process as long as the components remain unmixed. In dry winding, on the other hand, the raw material must be kept below freezing temperature to avoid premature curing of the resin system. Despite this enormous advantage, wet winding has several disadvantages. First of all, the manufacturing process must be performed at a fast pace, as the impregnation of the fiber in the matrix becomes progressively more ineffective as the viscosity of the polymer increases with curing time. Alternatively, winding must be performed in subsequent steps by mixing only limited amounts of resin components at the time, allowing only a portion of the raw material to start curing. A second disadvantage of wet winding is the high level of maintenance required for the instrumentation. In fact, the stickiness of the thermoset resin still in its liquid phase requires frequent cleaning of the manufacturing tools, increasing the labour costs of in-series production [18]. Another important difference between wet and dry winding is the possibility to achieve high accuracy in the placement of plies at different locations. As in wet winding the matrix must be liquid

enough for impregnation, its tackiness is partly compromised, making it difficult for the impregnated fibers to stick to the underlying surface in the desired location and orientation. As consequence, the fiber tows in wet winding tend to slip and accurate fiber placement cannot be guaranteed. In this context, dry winding is a much better alternative as the uncured resin of pre-impregnated composite materials is designed to be sticky enough to allow good adhesion with the surface underneath. Therefore, an adequate level of control over the location and orientation of the fibers can be achieved by programming the movement of the winding machine appropriately [10]. Similarly, controlling the fiber volume content and ensuring its maximization is more easily achievable in dry winding. The spools provided from the material manufacturers are designed and processed in such way to maximize the ratio of fiber-to-matrix volume, with the intention to guarantee maximum material performance without compromising the important load-transfer purpose of the matrix. For these reasons, dry winding is often preferred for research purposes where high precision is needed. This leads to better prediction of the material architecture both in terms of fiber orientation and in terms of fiber volume content.

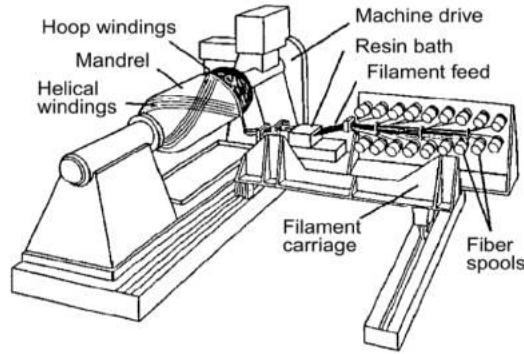


Figure 1.3: Schematic representation of a wet winding process on a portal axis machine, from [16].

The translational and rotational motion of the winding robots for dry winding gives origin to two layer types, presented in Figure 1.4. Helical layers define a balanced  $[\pm\alpha]$  interwoven laminate as the filament is deposited from pole to pole. Circumferential layers, on the other hand, are wound nearly perpendicularly to the longitudinal axis of the vessel in its cylindrical section. Here, the stability of the fibers is not affected by the high slip potential caused by curvature of the liner. The cylindrical region of the vessel experiences high tangential stresses, therefore benefiting from the presence of the fiber reinforcement at high angles of orientation [19]. On the contrary, helical layers are used to reinforce the vessel axially and tangentially according to their orientation, which refers to their angle of inclination in the cylinder with respect to the longitudinal axis of the vessel. This tends to be constant in cylinder, but it increases in the dome regions, where the tows approach the turnaround point. According to their orientation, helical plies can be classified into two layer types. Low angle helical plies, with orientation typically ranging between 0 and 20 degrees in the cylinder, are used to reinforce the vessel longitudinally and have small polar openings, reaching the interface between liner and boss at the boss neck. High angle helicals, on the other hand, have orientation usually ranging between 20 and 80 degrees and despite providing less axial reinforcement, play an important role in the tangential reinforcement of the dome regions. High angle helical plies have larger polar openings, and therefore do not reach the neck of the boss.

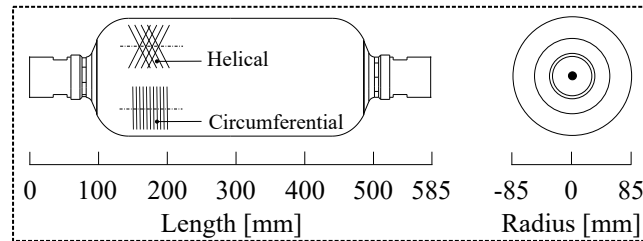


Figure 1.4: Representation of helical and circumferential fiber orientations, adapted from [10].

Once the laminate is wound, the vessel is cured in an oven or by means of radiating heaters according to

the curing cycle specified by the prepreg manufacturer. Despite its advantages in reducing porosity while increasing fiber volume fraction, vacuum bag curing is usually avoided because of its related high costs. Adding layers of consumables to the lamination process requires a significant amount of disposable material and a labour-intense effort, which is not realistic for mass production. Similarly, autoclave curing is not necessary for filament wound pressure vessels, as the required fiber volume content and compaction can be achieved by applying an appropriate tension force on the fibers during winding. This way, it is possible to avoid drastic increases in manufacturing costs and time [20].

The performance of filament wound pressure vessels is influenced by a series of parameters which come as direct consequences of the manufacturing process. Amongst others, the geometry of the vessel and the material composition of its laminate structure are highly influenced by the winding procedure, and have an impact on the stiffness and load distribution of the vessel. For this reason, in the next sections, the most important aspects are analyzed separately.

### 1.2.2. Filament Path Definition and Thickness Accumulation

The adequate definition of filament paths is one of the most important aspects of CPV manufacturing, as it defines the complex geometrical shape of the dome end-caps. Here, local changes in fiber orientation are necessary to achieve full mandrel coverage and to provide the mandrel with the needed reinforcement to withstand the internal pressure loads. As mentioned, the deposition of circumferential plies is unsuitable for the curved dome shape, and therefore only helical layers are wound in this region. As helical plies approach their turnaround point at different locations along the dome profile, their orientation increases progressively to approximately 90 degrees. This leads to a change in stiffness, resulting from the deviation from the nominal ply orientation measured in the cylinder. Furthermore, a drastic increase in local thickness at the polar openings is caused by the multiple passes that are necessary to achieve full vessel coverage in the cylinder [21].

Quantifying the rate of change in ply orientation in the dome regions is complicated. In general, each helical ply follows either a geodesic or a non-geodesic path to reach its turnaround point. The former is described as the shortest trajectory between the end of the cylinder and the polar opening, and it is often assumed for CPV analysis to simplify all calculations. However, considering only geodesic paths limits the design space of CPVs. The vessel can in fact benefit from the implementation of non-geodesic paths, as these allow a more uniform distribution of stresses across the dome surface [22]. Whereas earlier studies mainly focussed on geodesic paths for dome design purposes, more recent analysis have focussed on non-geodesic path definitions [22–24]. In both cases, the proper depiction of the vessel geometry has shown to be crucial for an accurate simulation of the vessel behavior. For this reason, the effects of filament path definition on the thickness accumulation at the turnaround points have been investigated in numerous papers [21, 22, 25].

In general, predicting the complex geometry around the turnaround points is a difficult challenge to tackle, as the thickness accumulation is often highly irregular. An example of thickness profile prediction is formulated by Leh et al. [21] and presented in Figure 1.5. The figure shows a comparison between the measured dome thickness and its simulated counterpart based on the estimated path definition. The left figure serves as benchmark, whereas the right figure includes a fixed non-zero thickness at the polar opening.

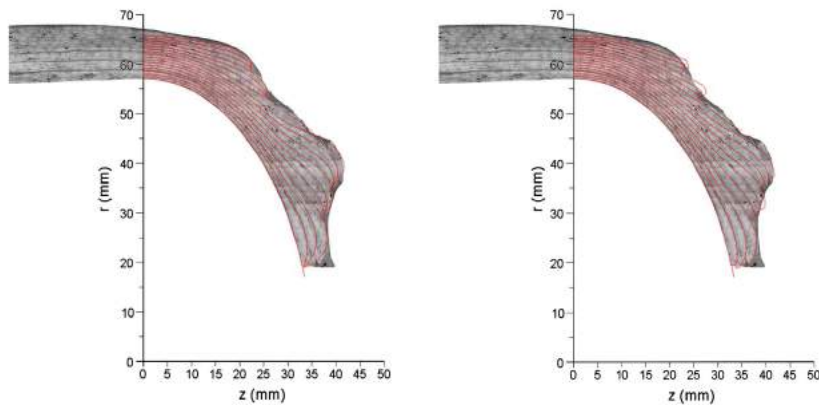


Figure 1.5: Coupling of non-geodesic fiber path and roving thickness estimation at the dome, from [21]. The figure on the left serves as reference. The figure on the right shows the contour of each ply when a non-zero thickness constraint at the turnaround point is applied.

An approach to deal with the complex problem of thickness prediction is proposed by Liang et al. [25], whose method is based on the definition of filament path on a curved surface formulated by Zu et al. [22]:

$$\frac{d\alpha}{dz} = \lambda \cdot \left[ \frac{\sin(\alpha)\tan(\alpha)}{r} - \frac{f''}{1+r'^2}\cos(\alpha) \right] - \frac{r'\tan(\alpha)}{r} \quad (1.1)$$

Here,  $\alpha$  is the angle between the winding direction and the meridional path,  $\lambda$  defines the coefficient of slippage of the tow,  $z$  corresponds to the axial coordinate and  $r$  is the radial coordinate. This is obtained as a function of the axial location  $z$  and the geometrical angle  $\theta$ , as described in Figure 1.6.

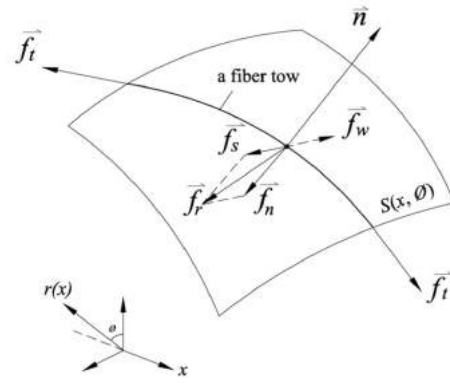
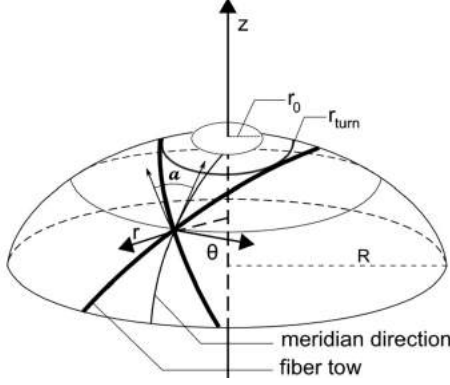


Figure 1.6: Non-geodesic winding path, from [21]      Figure 1.7: Stress state of a filament tow on an arbitrary convex surface, from [26]

The coefficient of slippage is defined by De Carvalho et al. [27] as the ratio between the transverse force  $f_s$  and the normal force  $f_n$  on the filament:

$$\lambda = \frac{f_s}{f_n} \quad (1.2)$$

Figure 1.7 is provided with the aim to explain the origin of  $f_s$  and  $f_n$  as tangential and normal components of the force  $f_r$ , resulting from the fiber tension on the laminate surface.

Slippage is highly affected by the fiber tow trajectory, the viscosity of the resin system, the fiber tension and the surface roughness. Wang et al. [26] elaborates that the winding type also plays an important role in the determination of the fiber slippage coefficient, which can vary from 0.1 to 0.5 for wet and dry winding respectively. In general, the path is stable and not susceptible to slippage if the transverse force is lower than the static friction between the filament and the underlying surface. For geodesic paths, this transverse force is null. As described by Liang et al. [25], in this case the condition posed by Clairaut's equation is satisfied:

$$r \sin(\alpha) = \text{constant} \rightarrow \sin(\alpha) = \frac{r_0}{r} \quad (1.3)$$

where  $r$  is the vessel radius at the specific axial location and  $r_0$  is the radius at the turnaround point. The winding angle between the filament winding direction and the longitudinal axis of the vessel is defined as  $\alpha$ . The method assumes that each filament crosses the equator and all concentric circles in the dome an equal amount of times without doubling the path nor abruptly terminating. This assumption translates to the following expression:

$$t(2\pi r)\cos(\alpha) = t_c(2\pi r_c)\cos(\alpha_c) = \text{constant} \quad (1.4)$$

where  $t$  is the shell thickness and the subscript  $c$  denotes the location of transition between cylinder and dome. Substitution of Equation 1.4 into Equation 1.3 leads to the following relation between the thickness at any point of the dome and the cylinder thickness:

$$\frac{t_d}{t_c} = \sqrt{\frac{r_c^2 - r_0^2}{r^2 - r_0^2}} \quad (1.5)$$

The approach described by Liang et al. [25] is however not universal and does not apply to non-geodesic path definitions. In the case of non-geodesic paths, the slippage coefficient  $\lambda$  is either negative or positive,

indicating a shift in location of the turnaround point respectively towards the cylinder or towards the boss. For this case, an alternative method is elaborated by Leh et al. [21], who estimate the dome thickness on the basis of the spline function method elaborated by Wang et al. [26, 28]:

$$t(r) = \frac{n_R m_R t_p}{\pi} \left[ \arccos\left(\frac{r_{turn}}{r}\right) - \arccos\left(\frac{r_b}{r}\right) \right] \quad \text{for} \quad r_{2b} \leq r \leq R \quad (1.6)$$

$$t(r) = A + Br + Cr^2 + Dr^3 \quad \text{for} \quad r_{turn} \leq r \leq r_{2b} \quad (1.7)$$

In the equations,  $r_b$  and  $r_{2b}$  are the polar openings at a distance of respectively one and two tow-width distances from the turnaround point. Here, the polar opening is defined by  $r_{turn}$ . Coefficients  $A$ ,  $B$ ,  $C$  and  $D$  are the coefficient defining the thickness profile in the dome, and are determined by the laminate thickness at the turnaround point. Parameters  $n_R$  and  $m_R$  indicate the number of pseudo-ply and their count in the cylindrical region of the vessel. It should be noted that a pseudo-ply is a group of two consecutive plies of opposite orientation ( $+\alpha/-\alpha$ ), whereas a layer is defined as a group of pseudo-ply in the same orientation.

The presented work shows relatively accurate results which relate closely with the products of the filament winding process. This is further elaborated in the study of Nebe et al. [10], where the thickness is adjusted manually to achieve a close correlation between experimental and numerical results.

Another iteration to the method is proposed by Zu et al. [29], who takes into consideration the influence of the bandwidth and the number of tangential points at the dome to further improve the accuracy of the thickness approximation. Specifically, according to the simulation presented by Zu et al. [29], choosing the appropriate bandwidth and number of tangential points at the tows is fundamental to minimize the amount of material used in the design of the composite pressure vessel without compromising a smooth thickness profile in the dome. Intuitively, as the roving bandwidth increases, the number of wound circuits to achieve full mandrel coverage decreases. However, this does not necessarily correspond to an overall reduction of material used, as effectively the length of rovings placed along the circumferential direction is highly affected by this increase in bandwidth. Zu et al. [29] suggest on the contrary that an optimum design can be obtained by minimizing the roving bandwidth.

The downside of this approach is that it leads to an increased number of passes in the cylindrical section and therefore an increase in fibers overlap in the dome area. As shown in Figure 1.8, the overlap tends to increase for increasing number of circuits or, in other words, for decreasing roving bandwidth. This inherently leads to a thicker profile at the domes.

A second parameter influencing the thickness build-up at the dome is the number of tangential points around the boss. As this number increases, the number of wound circuits necessary to achieve full mandrel coverage decreases. This leads to an overall thinner profile at the poles, inherently resulting in a more uniform thickness distribution.

In conclusion, predicting the thickness build-up at the poles is extremely complicated, as this is influenced by several design variables and manufacturing parameters, which are often difficult to reproduce simultaneously. Nevertheless, a realistic geometrical depiction of the vessel is of high importance as this influences greatly the accuracy of the simulation and inherently the theoretical understanding of the mechanical behavior of the pressure vessel.

### 1.2.3. Effects of Fiber Tension

Tension can be imposed on the fiber during manufacturing by controlling the torque of the motors connected to the CFRP spools [30]. This parameters has a twofold impact on the laminate architecture. First of all, tension is directly related to the roving friction. In general, the higher the tension on the fibers, the higher the normal load imposed on the surface and the higher the friction between the composite material and the underlying structure. High friction gives the opportunity to tune the filament path and therefore allowing more extreme non-geodesic path without encountering fiber slippage.

The second important role of fiber tension is to consolidate the undelying laminate therefore increasing its fiber volume content [30]. When a ply is wound at high fiber tension, the layers underneath are pressed together. This favors better adhesion between the plies and forces the air voids to escape the laminate, overall improving its quality. On the contrary, low fiber tension generally translates into low consolidation levels, reasonably leading to a higher void content. Therefore, high fiber tension is generally favorable. However, this brings along several limitations. A high fiber tension may lead to an excessive resin squeeze out, translating to inadequate inter-ply bonding and dry spots across the laminate [16]. The risk of this phenomenon is the inappropriate transfer of loads between the fibers, which work collaboratively thanks to the efficient shear

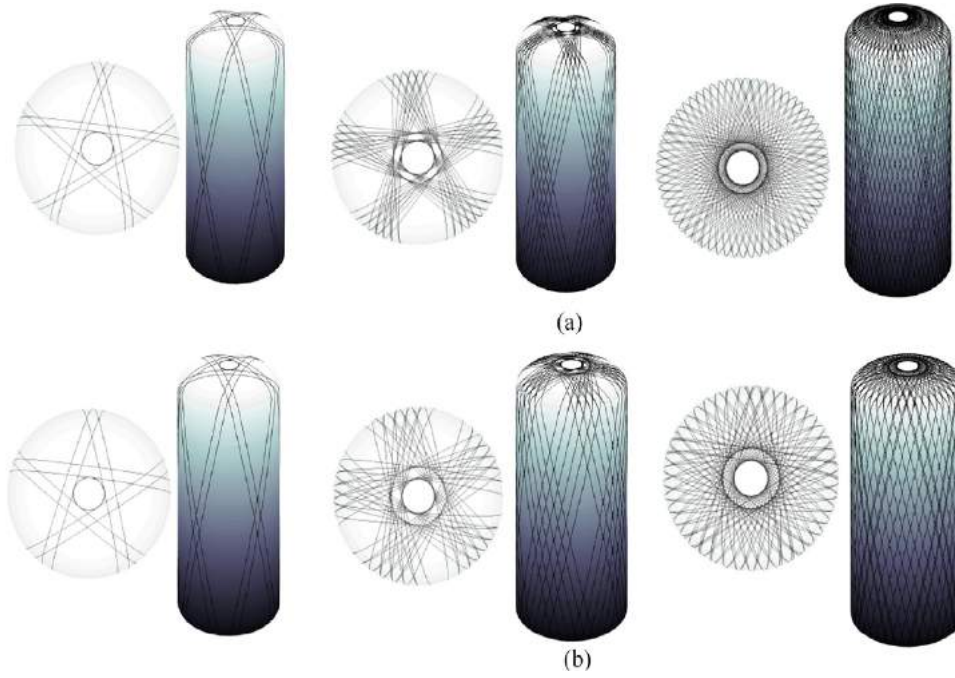


Figure 1.8: Non geodesic patterns for different roving bandwidths: (a) thin bandwidth - (b) wide bandwidth, from [29]

load transfer allowed by the resin. Finally, high fiber tension may potentially lead to undesirable mandrel deformation, which is typically difficult to predict, complicated to quantify and often results in an overall decrease of the tank capacity. For this reason, tension must be finely tuned during manufacturing. Typically, low fiber tension is chosen for the deposition of circumferential plies in the cylinder, where the high level of compaction is guaranteed by the high angle of orientation of the plies. Here, high tension would lead to inappropriate mandrel deformation, which in fact shows low stiffness in the radial direction. On the other hand, helical plies are usually wound at high fiber tension to guarantee an appropriate level of compaction in the dome regions. In this case, the high fiber tension does not compromise the mandrel shape as long as its axial component remains withstandable by the axial stiffness of the liner polymer. In any case, the liner is usually pressurized from the inside during winding, to limit any variation of the mandrel shape.

Inherently to higher compaction, the tension force on the fiber tows also has a direct correlation with the thickness of the final product. As the normal component of the force  $f_n$  increases and the laminate is compacted, its thickness decreases. According to Mertiny et al. [30], the overall laminate thickness in the cylinder can be calculated as:

$$t_{tot} = t_1 + t_2 + \dots + t_n \quad (1.8)$$

where  $t_n$  is the thickness of a single composite layer, calculated as:

$$t_n = \frac{n_{tow} W_{tow} C}{v_f \rho_f \pi (r + t_1 + t_2 + \dots + t_{n-1}) \cos(\alpha)} \quad (1.9)$$

Here,  $n_{tow}$  is the number of tows,  $W_{tow}$  is the tows weight,  $C$  is the number of winding circuits to achieve full mandrel coverage,  $\rho_f$  is the fiber density,  $\alpha$  is the winding angle and  $v_f$  is the fibre volume fraction. As fiber tension increases and fiber volume increases, the thickness tends to reduce.

Fiber tension is also important to control the mechanical properties of the laminate. The results of the analysis carried out by Mertiny et al. [30] on a filament wound tubular laminate with stacking sequence  $[\pm 60_3]_T$  show that the stress states on the laminate and the associated failure stage are related to fiber tension. However, increasing fiber tension does not lead to a unequivocal improvement in mechanical properties: it is beneficial in case of fiber-dominated loading, whereas a slight decrease in failure strength is recorded in case of matrix-dominated loading.

Estimating the effects of compaction and how it develops through the laminate is rather difficult. Different plies experience different levels of compaction, and predicting the decrease in thickness at different through-thickness locations is complicated. A thickness correction algorithm is developed for this purpose by Kang

et al. [31]. This model describes a strategy to determine the stress state of CPVs as result of the winding and curing processes. The first ones are mainly caused by the tension load applied on the fibers, whereas the second ones are attributed to the thermal stresses and the shrinkage associated to them. The model developed by Kang et al. [31] has been applied within the scope of the Fuel Cell Development department at cellcentric GmbH throughout previous investigations, to estimate the impact of fiber tension on the model. However, this analysis did not include the estimation of the stress state induced on the laminate during curing, as this requires detailed material information which is indeed difficult to retrieve.

The model developed by Kang et al. [31] relies on the following fundamental assumptions:

- plane stress conditions apply to the laminate, meaning that all non-zero stress components act in one plane only;
- the rule of mixture provides a reasonable estimation of the composite modulus;
- the internal liner material is isotropic and shows linear elastic deformational behavior;
- layers are modelled in a discrete manner, meaning that the stress in each individual ply is a consequence of the superposition of the surrounding plies.

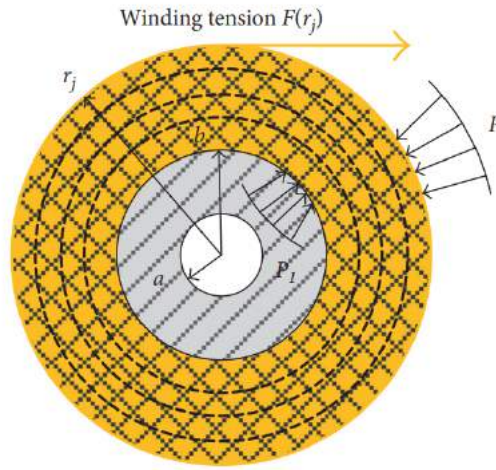


Figure 1.9: Cylinder discretization and load schematic according to the model proposed by Kang et al. [31]

Figure 1.9 show a cross-section of the cylindrical region of the vessel during winding, where the relation between the internal pressure loading and the tension force becomes apparent. Throughout the approach, the authors first estimate the stress state of the mandrel according to thick cylinder theory. Then, the stresses on the laminate itself are computed according to the linear constitutive equation below:

$$\begin{bmatrix} \epsilon_r \\ \epsilon_\theta \end{bmatrix} = \begin{bmatrix} \frac{1}{E_r} & \frac{-\nu_\theta}{E_\theta} \\ \frac{\nu_r}{E_r} & \frac{1}{E_\theta} \end{bmatrix} \begin{bmatrix} \sigma_r \\ \sigma_\theta \end{bmatrix} \quad (1.10)$$

In Equation 1.10,  $E_r$  and  $E_\theta$  correspond to the radial and tangential elastic moduli,  $\nu_r$  and  $\nu_\theta$  are the Poisson's ratios in radial and tangential directions, whereas  $\sigma_r$  and  $\sigma_\theta$  are the radial and tangential stresses.

In this case, the mechanical equilibrium of the system is defined as:

$$\frac{d\sigma_r}{dr} + \frac{\sigma_r - \sigma_\theta}{r} = 0 \quad (1.11)$$

The combination of Equation 1.10 and Equation 1.11 leads to the following expression, describing the radial deformation of the system:

$$u_r = c_1 r^\beta + c_2 r^{-\beta} \quad (1.12)$$



Here,  $c_1$  and  $c_2$  are constants which depend on the boundary conditions of the system, and  $\beta$  is calculated as  $\sqrt{\frac{E_\theta}{E_r}}$ . From Equation 1.10, Equation 1.11 and Equation 1.12, the stress in the laminate cylinder are computed as:

$$\begin{aligned}\sigma_r &= c_1 S_1 r^{\beta-1} - c_2 S_2 r^{-\beta-1} \\ \sigma_\theta &= c_1 S_3 r^{\beta-1} - c_2 S_4 r^{-\beta-1}\end{aligned}\quad (1.13)$$

Here, the  $S$  coefficients are shape functions defined as:

$$\begin{aligned}S_1 &= \frac{\beta + \nu_\theta}{1 - \nu_r \nu_\theta} E_r \\ S_2 &= \frac{\beta - \nu_\theta}{1 - \nu_r \nu_\theta} E_r \\ S_3 &= \frac{\beta + \nu_r}{1 - \nu_r \nu_\theta} E_r \\ S_4 &= \frac{\beta - \nu_r}{1 - \nu_r \nu_\theta} E_r\end{aligned}\quad (1.14)$$

The combination of boundary conditions holding for the cylindrical region of CPVs is represented by the equations Equation 1.15. These are then applied to derive  $c_1$  and  $c_2$  as shown in equation Equation 1.16.

$$\begin{aligned}\sigma_r &= K \cdot u_r, & r &= b \\ \sigma_r &= -P, & r &= r_j\end{aligned}\quad (1.15)$$

$$\begin{aligned}c_1 &= -\frac{H_2(r_j/b)^{2\beta}}{H_1 S_2 + H_2 S_1(r_j/b)^{2\beta}} \left(\frac{1}{r_j^{\beta-1}}\right) P, \\ c_2 &= \frac{H_1 r_j^{\beta+1}}{H_1 S_2 + H_2 S_1(r_j/b)^{2\beta}} P\end{aligned}\quad (1.16)$$

Here,  $H_1 = Kb - S_1$  and  $H_2 = Kb + S_2$ . From this, fully worked-out expressions for the radial and tangential stresses in the laminate cylinder are derived by applying the principle of superposition, by which the stress in the  $i$ th layer of the composite is calculated as the sum of the stresses introduced by the winding of all layers underneath. As the thickness of all plies is relatively small, this summation can be expressed as a continuous integral. The results for radial and tangential stresses respectively are presented in Equation 1.17 and Equation 1.18. Here,  $h$  is the ply thickness and  $f(r_i)$  is the fiber tension during winding.

$$\sigma_r^{wt}(x) = -\frac{1}{h} [(H_1 S_2 - H_2 S_1(x)^{2\beta})(x)^{-\beta-1} \int_x^m \frac{\zeta^\beta F(\zeta)}{H_1 S_2 + H_2 S_1 \zeta^{2\beta}} d\zeta] \quad (1.17)$$

$$\sigma_\theta^{wt}(x) = \frac{1}{h} [f(x) + (H_1 S_4 - H_2 S_3(x)^{2\beta})(x)^{-\beta-1} \int_x^m \frac{\zeta^\beta f(\zeta)}{H_1 S_2 + H_2 S_1 \zeta^{2\beta}} d\zeta] \quad (1.18)$$

Although the model is principally designed for composite cylinders, it has been applied in previous investigations within cellcentric GmbH to estimate the effect of fiber tension to the entire vessel [32]. With this purpose, the CPV is discretized into a series of cylinders of varying radii along its length and the radial stresses are calculated for each one of these cylinders. The radial stresses are then converted to strains to estimate the thickness reduction deriving from compaction during winding.

### 1.3. Research Focus and Thesis Structure

The use of CPVs in automotive is well established. However, full understanding of their complicated laminated structure is yet to be achieved, especially in light of the design variables introduced during manufacturing. Further research is therefore necessary to ensure a minimization of the CFRP material applied to reinforce the vessel. Such minimization would allow to reduce the costs of CPVs without compromising their structural robustness.

In this context, the objective of this research is to contribute to the design of hydrogen storage systems for the automotive industry by developing a reliable and comprehensive analysis strategy of as-manufactured composite pressure vessels. Specifically, the research focusses on the realization of a sound numerical tool, capable of realistically reproducing the mechanical response of CPVs during pressurization in a fast and accurate manner. The tool is then applied on several configurations of CPVs for which an extensive library of experimental data is available. Its applicability to different vessel configurations and failure types is then evaluated.

The thesis presents firstly a thorough explanation of the analysis strategies which can currently be found in literature, including the simulation tools that have been developed within the Fuel Cell Development Department at cellcentric GmbH. Effectively, these set the state-of-the-art prior to this research. This overview, provided in Chapter 2, highlights the knowledge gaps currently existing in the understanding of CPVs, and allows to define the research questions and objectives. The numerical modelling strategy worked out throughout the project is elaborated in Chapter 3, which expands on its advantages and limitations in terms of accuracy and computational time. In Chapter 4, several adjustments to the vessel model are presented, which involve the geometrical definition of the filament wound vessel and its material composition. In this context, the propagation of damage through the laminate is also addressed, and the numerical solution adopted to simulate the mechanical response of the structure to failure is described in detail. The results of the simulation strategy for different configurations are presented in Chapter 5, which includes the analysis of a series of CPVs which differ in terms of layup and failure type. The performance of the developed numerical tool is then reflected upon and discussed in Chapter 6. Finally, the research work is summarized in Chapter 7, where clear answers to the research questions are provided and the general outcome of the investigation is concluded.

# 2

## Research Framework

As introduced in Chapter 1, this research focuses on the simulation of the deformational behavior of composite pressure vessels during operation, and on the relative prediction of the burst event. Specifically, the focus lays on the development of a tool which can accurately depict the laminate response in the different design-critical areas of the vessel and can efficiently be used for design purposes. With this in mind, it is important to analyze the framework that defines the need for such research. As CPVs are not new to the automotive industry, a library of analysis strategies have been developed by different parties and is available in literature. These have been used as baseline for this work and provide fundamental insights on the stress-state of different design-critical areas of the vessel. An overview of the most relevant ones is presented in Section 2.1, where special attention is given to the applicability of each strategy to several design problems. In fact, as not only accuracy is of interest but also computational time, different strategies are typically suited for different applications.

Despite providing reasonable results, many of these works lack a thorough experimental validation. Conveniently, a vast database of experimental results collected during burst experiments is available at cellcentric GmbH, facilitating the implementation of a robust validation method. The experimental techniques and all instrumentation used to perform the burst experiments are presented in Section 2.2.

The theoretical background and the experimental setup available offer the possibility to dive deep into the development of a verifiable modelling tool which can be used for the analysis of the response of different vessel types. This does not only allow to shed light on the CPV response to pressurization, but it also to test the applicability of the developed simulation method on distinctive failure behaviors. For this purpose, a set of vessel configurations is defined and presented in Section 2.3.

Once the theoretical and experimental frameworks of the research are clear, finally the research objectives are formulated. In Section 2.4 all research questions are reported, alongside an indication on the location in the document where the investigation is tackled.

### 2.1. Analysis Strategies for CPVs

The modelling of CPVs is a complicated task which has been addressed in many scientific contexts by the developing different analytical and numerical strategies of increasing level of complexity. The theoretical background surrounding CPVs is rather rich. Relatively simple analytical models focus on the more rudimentary netting theory for the analysis of vessel cylinders [33]. More elaborated strategies apply classical lamination theory (CLT) to account for the contribution of the matrix to the mechanical properties of the laminate [25, 34, 35]. Accurate numerical analysis simulate through-thickness effects and track progressive damage through the laminate [36–39]. Before diving into a detailed overview of the most relevant studies, it is fundamental to introduce the loading state of pressure vessels, which is best described by considering the isotropic cylindrical tank presented in Figure 2.1.

In the cylinder, the predominant radial expansion imposed by the internal pressure causes high tangential loading, which can be computed as [41]:

$$N_{\theta}'' = \frac{pR}{t} \quad (2.1)$$

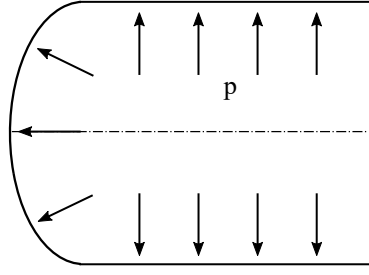


Figure 2.1: Isotropic cylindrical pressure vessel with elliptical head, from [40].

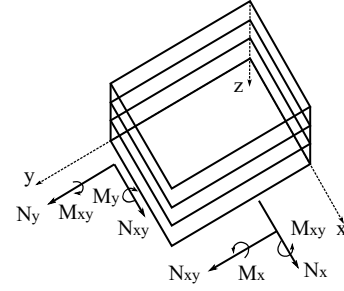


Figure 2.2: Resultant loading on laminated plate.

Here, superscript  $''$  indicates cylinder conditions, as opposed to superscript  $'$  which corresponds to dome conditions.

In the dome region, on the other hand, the change in geometry causes the loading components of the internal pressure to change. For a hemispherical dome, for example, the meridional and tangential loading becomes equal to [41]:

$$N'_\theta = N'_s = \frac{pR}{2t} \quad (2.2)$$

According to Balicevic et al. [40], the difference in internal forces between cylinder and dome is particularly important as it causes internal moments which eventually result in a difference in radial displacements between the two regions. In this work, where thin walled conditions are assumed for an isotropic vessel with elliptical end-caps, the axial force  $N'_s$  and the circular normal force  $N'_\theta$  in the dome wall are defined according to membrane theory:

$$N'_s = \frac{pR}{2} \left( \frac{1 + \gamma}{1 + \gamma \sin^2 \theta} \right) \quad (2.3)$$

$$N'_\theta = (1 - \gamma \sin^2 \theta) N'^{(0)'}_s \quad (2.4)$$

An overview of all geometrical parameters and the loading on the structure is provided in Figure 2.1.

The membrane load components computed by means of Equation 2.3 and Equation 2.4 are compressive in the dome, and tensile in the cylinder, leading to a difference in radial displacement which can be computed as:

$$u_r^{(0)''} - u_r^{(0)'} = \frac{pR^2}{2Eh} (1 + \gamma) \quad (2.5)$$

From Equation 2.3 it is clear that the meridian force is continuous across the transition region and varies uninterrupted from cylinder to dome. However, the membrane component to the circular load is discontinuous at the boundary. As here the displacement of the two regions of the laminate should remain the same, additional loading occurs in the walls of the vessl. Different design strategies can be adopted to balance this effect. Balicevic et al. [40] conclude that stresses at the transition region can be significantly influenced by controlling the dome convexity and its wall thickness.

Composite pressure vessels differ from isotropic pressure vessels because they have the advantage of allowing local tailoring of the mechanical properties by arranging the composite plies in the direction of needed strength and stiffness. However, the anisotropy of the laminate, the heterogeneity of the material properties and the doubly-curved geometry introduce an extensive set of complexities in the analysis of the CPV. In the following paragraphs, different analytical and numerical strategies are described alongside their applicability and limitations.

### 2.1.1. Analytical Models

One of the most commonly used analytical approaches for the preliminary analysis of CPVs is netting theory, mainly applied because of its simplicity [42]. The fundamental assumption of netting theory is that all loads are carried by the fibers in tension, whereas the contribution of the resin to the structural performance of the laminate is null. In this sense, burst due to fiber fracture is the only admissible failure mode. Furthermore, all walls are considered to act as membranes and therefore do not carry any bending or out-of-plane shear loads [43].

Despite their conservative context, the analytical results of netting theory are usually accepted in the context of CPVs, especially for the study of the cylindrical region. Here the complexity of the laminate is not different from that of a planar laminate for which the reference system is converted from Cartesian to cylindrical [23, 33, 44].

Netting theory is found in literature also for the preliminary study of the dome. Amongst the earliest examples of dome analysis by means of netting theory is the one presented by Fukunaga and Uemura [33]. Here, the vessel contour is approximated by a multiple cubic spline definition, and the dome strength is calculated by assuming a geodesic filament path. This approach leads to an isotensoid solution, which allows for a quick estimation of the laminate thickness and the associated material usage. Specifically, two distinct approaches are followed by the authors to obtain the optimal dome shape: the first one is based on failure criteria, whereas the second one is based on performance factor. An initial calculation of meridional and circumferential loads on the vessel is carried out as [33]:

$$\begin{aligned} N_s &= \sigma t_r \cos(\alpha^2) \\ N_\theta &= \sigma t_r \sin(\alpha^2) \\ N_{s\theta} &= 0 \end{aligned} \quad (2.6)$$

where  $N_s$  and  $N_\theta$  are the loads in the meridional and circumferential directions,  $t_R$  is the ply thickness and  $\alpha$  is the ply orientation angle. Then, the optimal dome shape is derived with respect to several failure criteria, amongst which Tsai-Hill results in the best dome geometry. A second optimized dome shape is derived by maximizing the performance factor, defined as function of the storage volume and the CPV weight [33].

An iteration to the approach elaborated by Fukunaga and Uemura is proposed by Zu et al. [23], who include the possibility of a non-geodesic path description.

Effectively, the results of netting theory are not able to provide the most accurate picture of the thick-walled composite pressure vessel as they do not consider out-of-plane loading. In addition, the model is limited by the neglect of the contribution of the matrix, which however plays an important role in the determination of the mechanical properties of the laminate [34]. For this reason, classical lamination theory (CLT) is often preferred [25, 34, 35], as it offered a refined analysis which considers both the contribution of the matrix and more complicated loading cases, such as bending.

CLT is an analytical method for the analysis of laminated thin shells [45]. According to the definition of Parnas et al. [46], it is applicable to CPVs only when the ratio of outer to inner radius is smaller than 1.1, guaranteeing the thin-walled conditions that the theory relies on.

CLT owes its success to the high level of accuracy that it can provide at low computational expenses. When applying CLT to CPVs, the curved surface of the vessel is typically discretized in smaller flat plates in a state of plane stress [34].

According to CLT, the resultant forces and moments in the laminate are related to the strains according to the following relation [47]:

$$\begin{Bmatrix} N \\ M \end{Bmatrix} = \begin{Bmatrix} A & B \\ B & D \end{Bmatrix} \begin{Bmatrix} \epsilon^0 \\ \kappa \end{Bmatrix} \quad (2.7)$$

Here,  $N$  and  $M$  are respectively the force and moment vectors per unit length, as presented in Figure 2.2.  $\epsilon^0$  and  $\kappa$  represent the midplane strain and the curvature strain. Finally,  $A$ ,  $B$  and  $D$  are respectively the extensional stiffness matrix (expressed in  $N/m$ ), the coupling stiffness matrix (expressed in  $N$ ) and the bending stiffness matrix (expressed in  $Nm$ ).

CLT has been used for in the context of CPVs for several studies on layup optimization. Unlike netting theory, CLT is better able to represent material orthotropy of the structure. Madhavi et al. [35] show clearly the advantages of CLT over netting theory by using the first one for a preliminary design of the laminate thickness, and the second one to study matrix crack failure across the vessel. A similar proof is elaborated by Hojjati et al. [34], who perform a thorough investigation on the influence of the matrix on the determination of an accurate representation of the dome response to pressurization. Fukunaga et al. [48] take CLT a step further by analyzing the stress-state of cylindrical laminates with different stacking sequences to obtain a relation between layer orientation and deformational behaviour of the laminate. Similarly, Chauduri et al. [45] investigate an axisymmetrical thin cylindrical laminate subjected to internal pressure loading by means of CLT to observe the effects of a varying stacking sequence on the response of the cylinder boundaries.

CLT is usually not suitable for the analysis of CPVs for compressed hydrogen storage. In this case, the high operative pressures require the reinforcement of a thick laminate, which inherently introduces in the

structure the development of through-the-thickness stress gradients. A more applicable solution for this case is 3D elasticity. In this context, Xia et al. [49] highlight the dependency of the laminate response on the laminate thickness, as effectively the average meridional and tangential stresses computed by means of thin-wall assumptions are not realistic. An extension of the work of Xia et al. [49] which includes asymmetric laminates is proposed by Zu et al. [50], for which the bending and twisting responses cannot be neglected. Zu et al. [50] shows how the tangential and axial stresses vary within the cylinder wall thickness, and assess how the in-plane twisting caused by the unbalance in the laminate decreases for increasing laminate thickness.

Despite producing realistic preliminary results, all analytical solutions developed so far have the limitation of providing limited insights on the structural response of the dome region of the vessel. For this reasons, most recent strategies involve more elaborate finite element (FE) methods, which are able to combine the complexity of the CPV geometry to the thick-walled effects that arise in the laminate.

### 2.1.2. Numerical Models

Finite element models have several advantages. Firstly, they allow to tune the material properties of the different regions of the vessel independently and they accurately reproduce the interface between adjacent areas. Furthermore, finite element analysis (FEA) grants the possibility to simulate the progression of damage by consecutively degrading the material properties until final failure. Finally, they overcome the limitation of analytical models which consider the body in analysis as free in space. FEA, in this sense, offers a valid and often more accurate basis for simulation purposes.

In the context of CPVs, Seide et al. [51] uses FEA on a study on the effects of different boundary conditions on a thick laminate, discretized by using quadratic triangular finite elements. The authors here apply a layer-wise constant shear-angle theory (LCTS) to obtain a more accurate prediction of the distribution of the in-plane displacements and stresses through the laminate thickness and extends the investigation to the dome, as opposed to the analytical similar study presented by Chauduri et al. [45] which remains limited to cylindrical region.

The advantage of FEA simulations is also elaborated by Son and Chan [52], who compare two distinct methods. The first one utilizes a thin shell approach across the entire vessel length, obtaining realistic stress estimations in the cylinder. However, it underestimates the laminate stress-state in the dome and in the cylinder-dome transition region due to the unreasonable local thickness prediction of the model. The second approach includes a full ply-based FE modelling technique, based on a plausible thickness approximation which takes into account the irregularities which derive from the winding procedure. The result of the second approach is definitely more realistic. This work clearly shows the inadequacy of shell models in the representation of stress-states in the dome region of the vessel, caused by the neglect of through-thickness stress gradients and the thin-wall assumption. These are unrealistic in the dome region, where the material accumulation during winding causes the laminate leads to a thick laminate.

In the context of composite domes, Leh et al. [15, 21, 53] propose a comprehensive methodology to describe both geodesic and non-geodesic paths to develop an optimization tool for design purposes. For example, in [53], the authors describes the differences between a solid model definition and a simpler axisymmetric approximation. Both methods include the implementation of the Hashin-Rottem failure criterion to estimate the propagation of failure through the laminate. The results are then correlated to those collected throughout experiments as for validation purposes. Both simulation strategies showed a general agreement to the testing results, although an underestimation of the burst pressure was recorded. This discrepancy is likely caused by imprecisions in the definition of the material properties, by an inadequate thickness approximation and by the absence of plasticity in the boss response, proved by Berro et al. to be significant [54]. In general however, despite being more computationally expensive, the solid model does not seem to provide relevant improvements to the axisymmetric solution.

Another example of damage propagation analysis in CPV is presented in two works by Wang et al. [36, 37]. The first one uses a continuum damage mechanics (CDM) model based on Hashin failure criterion [36]. This accounts for intralaminar damage and delaminations, as cohesive elements are nested between the laminate and the liner, and between the different plies. In the second one, the loading on the structure is modelled by means of a macro-mechanical model, whereas micro-mechanics is used to address damage progression. The results are subsequently scaled up by correlating the respective stress levels in each model. This work has shown remarkable results in the prediction of failure in the cylindrical region of the vessel, but it is limited in the full depiction of the dome behavior where the geometry is difficult to simulate and the material properties appear heterogeneous [37].

FEA also allows to investigate the development of fracture through the laminate, as studied by Lin et al.

[39] by applying a user-defined field (USDFLD) subroutine in Abaqus which relies on Puck failure criterion to degrade the elastic parameters of the composite material in case failure. This may occur in the form of fiber tension failure, fiber compression failure, matrix tensile failure or compressive failure. The method relies on cohesive elements of zero thickness between the plies to simulate interlaminar failure. As validation, acoustic emission detection is applied to localize damage to some extent. This method allows a promising prediction of burst pressure, which on average deviates from the experimental result of only 5.4%. However, once again, the burst event occurs in the cylinder, therefore providing little information regarding the accuracy of the model in the dome region.

Finally, a robust progressive damage approach is proposed by Magneville et al. [38], based on a detail material characterization approach meant to quantify the laminate material properties in different areas of the CPVs by means of computed tomography (CT) and microscopic inspection. The authors elaborate on an axisymmetrical numerical model based on the multi-sequence layup proposed by Leh et al. [21]. Despite still excluding delaminations, this is then improved by the implementation of CDM, which includes plasticity of the boss and time delay caused by material viscosity.

### 2.1.3. Previous Research at cellcentric GmbH

Within the Fuel Cell Development department at cellcentric GmbH, Soriano developed a high fidelity numerical model in Abaqus as part of his MSc thesis at the Technical University of Delft [55]. A schematization of the model setup for a specific stacking sequence is presented in Figure 2.3.

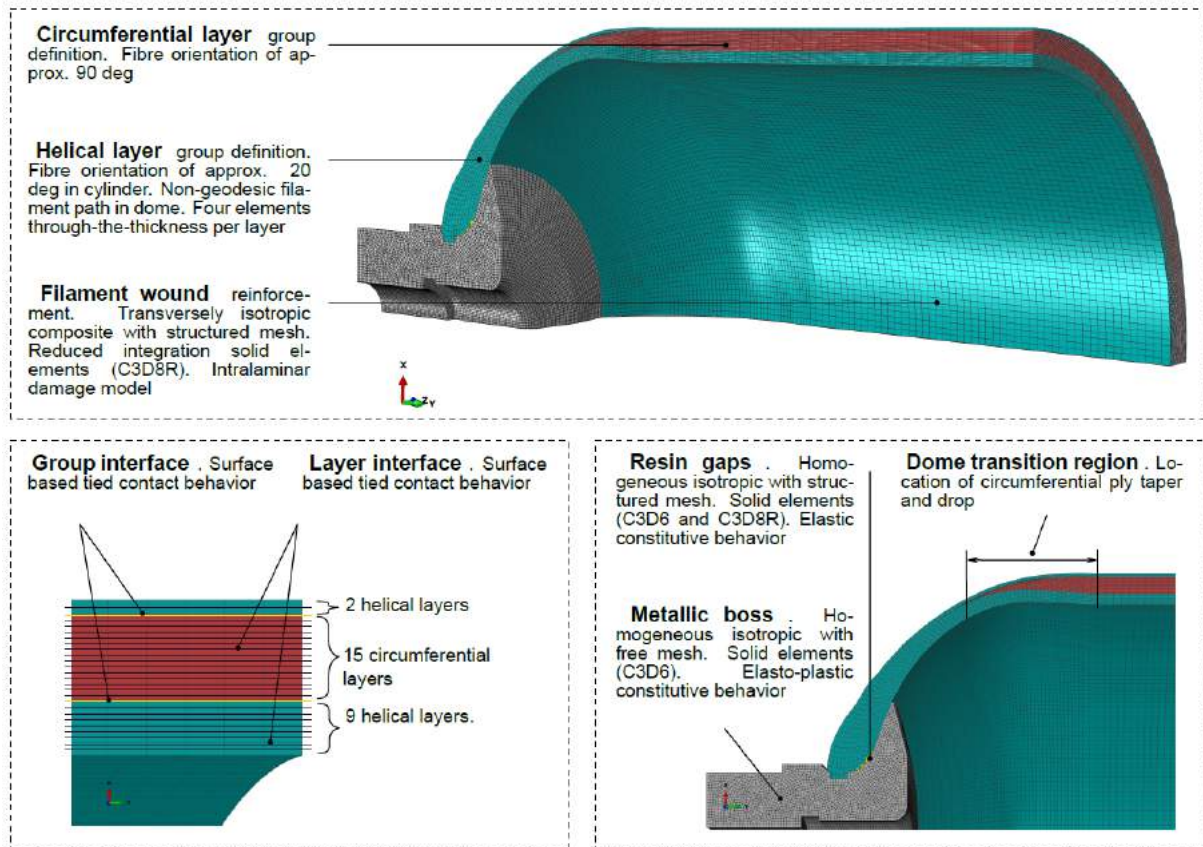


Figure 2.3: Representation of the structured solid mesh used in by Soriano, including the definition of material properties and layer types, from [55].

The research initially relies on a constitutively elastic analysis to simulate the deformational behavior of CPVs and estimate the pressure stage of damage onset, evaluated as failure in the fiber constituent. The level of complexity is then increased progressively by considering damage propagation through the laminate, and the effects of heterogeneous material properties. The model is based on the CDM model proposed by Leone et al. [56], used to reproduce cracks embedded within the continuum elements as cohesive surfaces. Material degradation is included in the model by reducing the stiffness of the constituents as damage progresses. The



results of the simulations are in agreement with the experimental data in case of cylinder failure, showing discrepancies below the threshold of 5% both for the constitutively elastic solution ( $\sim 4.8\%$ ) and the solution which includes damage progression ( $\sim 2.2\%$ ).

The simulation comes at the expense of high computational times, strongly affected by the complexity of the problem and the extremely fine required mesh. Furthermore, some discrepancies between simulation results and experimental data exist in the dome and cylinder-dome transition region, attributable to inaccuracies in the depiction of the vessel geometry and the tapering of circumferential plies.

In general, fast computation is a necessity to meet the requirements of cost- and time-effective design phases, which are a standard in the automotive industry. For this reason, Johman [32] presents an investigation in which the focus is shifted towards computationally inexpensive and robust models. The author proposes an analysis strategy articulated in three steps. Firstly, the geometry of the vessel and the orientation of each ply is extracted from the winding software in use. Then, the geometry is corrected by adjusting the thickness of each ply according to Kang compaction model [31], as explained in Chapter 1. Finally, the generated vessel geometry is imported in a FE model developed in Abaqus, where quadratic solid elements are implemented to account for through-thickness effects. In the work presented by Johman, the model is then applied on the investigation of the laminate response according to a varying stacking sequence. In general, the correlation with experimental data shows remarkable accordance in deformational behavior of the cylinder, achieved through a faster method. In fact, the simulation can be run in approximately 30 minutes by using a 4 cores setup. However, important discrepancies in strain response can still be found both in the cylinder and in the dome region. These are attributable to the low resolution of the single through-thickness partition, and the numerical inconsistencies at the ply ends which make the results at the dome scattered and tedious to interpret. Finally, the model does not take into account the material heterogeneities introduced by the manufacturing process, and the effect of damage propagation on the material performance during pressurization. Overall, this results in discrepancies between the simulated and the experimental burst pressure.

Both models developed by Soriano [55] and Johman [32] serve as input to this research project, which aims to find a proper combination of fast computational time without compromising the accurate depiction of the laminate response.

## 2.2. Experimental Setup at cellcentric GmbH

Experimental validation is a crucial point not only to retrieve physical insights on the vessel response to pressurization, but also to assess the accuracy of the developed simulation tool. However, the experimental characterization of CPVs for hydrogen storage is typically complicated by the high pressures that the vessel is subjected to during operations. In addition, according to current regulations, the vessel is certifiable when able to withstand its operative pressure of 70 MPa multiplied by a safety factor, further increasing the required burst pressure to achieve experimentally to have an accurate representation of the vessel response. Due to these extreme conditions, the reinforcement on the mandrel is rather thick and the composition of the orthotropic CFRP material complicated. Conducting the project in collaboration with cellcentric GmbH offers the great opportunity to have access to a large database of testing results, collected over the years for the testing of large-scale and small-scale composite pressure vessels of different configurations. In this section, the facilities that allow the collection of such data are described in detail. It should be noted that the author contributed to part of the experimental set prior the beginning of this research project, whereas the remaining data was collected within the Fuel Cell Development department throughout previous investigations.

The facilities at cellcentric GmbH include an advanced towpreg filament winding robot and a one-of-a-kind test bench which allows to acquire various experimental data on the deformational and burst behavior of CPVs. The main manufacturing instrumentation consists of the 6-axis KUKA KR-500 machine presented in Figure 2.4, which allows dry winding of towpreg material around polymeric liners of different sizes. The mandrel is kept in place at the extremities of the robotic arm by pneumatic holders. These allow the rotation around its longitudinal axis to facilitate appropriate fiber placement. Furthermore, built-in pressure valves permit the pressurization of the liner during winding, to balance the stresses imposed by fiber tension on the surface. Directly in front of the winding machine is a column structure accommodating the eyelet, which rotates to ensure the deposition of fibers in the correct orientation. The eyelet contains the set of rollers presented in Figure 2.5, used to avoid overlapping between the fiber tows. The fiber filaments are fed to the eyelet from a creel which can accommodate 10 towpreg spools at the time. During winding, fiber tension is adjusted by regulating the torque on small electric motors installed in the creel. The creel is not refrigerated, meaning that the spools are set in place only shortly before the start of the winding process. On the contrary,



Figure 2.4: KUKA KR-500 robot for filament winding at cellcentric GmbH.



Figure 2.5: Overview of rollers installed on the filament winding eyelet.

they are kept in a freezer for storage purposes. Once the vessel is fully wound, it is placed inside an oven for curing. The curing cycle depends on the material specification provided by the resin suppliers. In this case, it includes a dwell phase of 8 hours at 110°C. During curing, the vessel rotates around its longitudinal axis to allow even hardening of all sides.

The manufactured vessels are then tested until burst in the unique burst chamber schematically presented in Figure 2.6. Inside the burst chamber, the bottom boss of the CPV is clamped to a fixed bearing and connected to a water pump which allows pressurization until 200 MPa. The top boss is clamped to a floating bearing which displaces vertically during pressurization, allowing the vessel to expand axially. 9 systems of camera pairs and a projector are installed in the walls of the burst chamber at different heights. These are used for two experimental techniques: firstly, stripe light projection, a contour scanning technique which relies on capturing the reflection of black and white light patterns projected on the vessel surface. Specifically, in stripe light projection the distance from the CPV outer surface to the cameras is computed by means of triangulation, creating a virtual points cloud which represents the three-dimensional vessel geometry. This is used throughout the project to compare the predicted vessel geometry to the shape of the filament wound CPV.

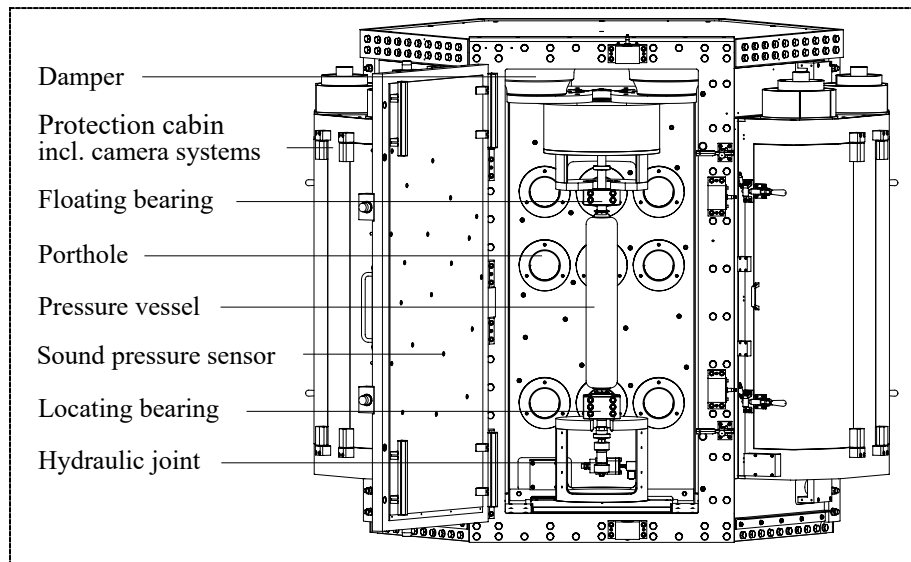


Figure 2.6: Schematic representation of burst chamber and testing instrumentation at cellcentric GmbH, adapted from [57].

More importantly, the camera systems are used for the collection of full-field strain measurements by means of digital image correlation (DIC). In DIC, the displacement of unique facets on the vessel surface is tracked by taking subsequent pictures of the CPV during pressurization at a frame-rate of one image per second. As the field of view of different camera systems overlap each other, the collected strain measurements are continuous along the surface both in the axial and in the tangential direction of the vessel. Typically, the

recording continues until burst to capture the strain response at every stage of pressurization.

Additionally, the burst chamber is provided of a set of 120 microphones distributed around its walls to record the acoustic emissions of the pressurized vessel. Thanks to a mathematical array, this technology allows to spacially localize damage as it initiates during pressurization. Despite enriching the capabilities of the testing facility, the correlation with acoustic emission data is not the focus of this research and it is therefore not further discussed in this document. However, it should be noted that for every discussed vessel configuration acoustic data has been collected and can therefore be used for further investigations.

## 2.3. Overview of Layups in Analysis

An adequate amount of circumferential plies is usually would around the cylindrical section of the mandrel to withstand the high in-plane stresses that develop tangentially due to the radial pressure loading. On the other hand, a sufficient amount of helical plies is required to reinforce the dome end-caps of the vessel, to compact the laminate, and to provide the necessary axial support to the entire structure. Inevitably, vessels composed by different layups are bound to behave differently during pressurization, and often experience different failure modes. In addition, previous research have found that not only the number of plies composing the laminate determines its structural response, but also their through-thickness order [57].







Vessel ID and weight	Description of Layup (From outer- to inner-most ply)	Failure Type
 BL 4.16 kg	<ul style="list-style-type: none"> <li>1 low angle helical ply (<math>\alpha = 20</math> deg)</li> <li>27 circumferential plies (<math>\alpha = 88</math> deg)</li> <li>4 high angle helical plies (<math>\alpha = 45</math> deg, <math>\alpha = 60</math> deg)</li> <li>10 low angle helical plies (<math>\alpha = 20</math> deg)</li> </ul>	Cylinder failure at 163 MPa 
 BC 4.29 kg	<ul style="list-style-type: none"> <li>10 low angle helical plies (<math>\alpha = 20</math> deg)</li> <li>4 high angle helical plies (<math>\alpha = 60</math> deg, <math>\alpha = 45</math> deg)</li> <li>27 circumferential plies (<math>\alpha = 88</math> deg)</li> <li>1 low angle helical ply (<math>\alpha = 20</math> deg)</li> </ul>	Cylinder failure at 189 MPa 
 W2B 2.80 kg	<ul style="list-style-type: none"> <li>1 high angle helical ply (<math>\alpha = 45</math> deg)</li> <li>20 circumferential plies (<math>\alpha = 88</math> deg)</li> <li>2 high angle helical plies (<math>\alpha = 60</math> deg, <math>\alpha = 45</math> deg)</li> <li>7 low angle helical plies (<math>\alpha = 20</math> deg)</li> </ul>	Dome failure at 127 MPa 

Figure 2.7: Overview of layups in analysis and respective failure types.

The performance of an analysis strategy can be assessed based on its applicability, or in other words, its capability of reproducing closely the behavior of different vessel configurations. For this reason, it is decided to focus the research on a series of vessels which differ from each other not only in terms of layup and stacking

sequence, but also in terms of observed behavior upon burst. Specifically, the configurations schematically described in Figure 2.7 are selected. Here, low angle helical plies are presented in blue, high angle helical plies are drawn in green and circumferential plies are shown in red. The respective ply orientations are presented in the description of the layout, whereas a picture of the burst behavior is illustrated alongside the respective burst pressure.

One of the advantages of focussing on these configurations is that several samples of each vessel type have been tested in the context of the Fuel Cell Development department at cellcentric GmbH in the test-bench described in the previous section. These sets of experiments provide an extensive database on their deformational behavior, and an indication of their experienced failure mode and location.

Vessel types BL and BC are chosen as they have been widely used in previous investigations, providing a legitimate benchmark for comparison. Johman [32] applied the modelling technique presented in Section 2.1.3 to these vessel configurations to study the behavior of the CPV laminate in the cylinder-dome transition region, and to simulate cylinder burst. Effectively, this research project comes as continuation of his work in the same industrial context. Therefore, it is useful to apply the newly-developed analysis strategy to the same set of vessels, with the purpose to more clearly assess its potential to improve the current benchmark. The peculiarity of the set of vessels presented in Figure 2.7, however, resides in the selection of the W2B vessel configuration. This layout allows to assessment of the model performance in the prediction of dome failure. Contrarily to cylinder failure, assessing dome burst remains a widely unexplored task that this investigation intends to shed light on.

## 2.4. Research Questions and Objectives

As presented throughout this chapter, the analysis of composite pressure vessels is not new to the automotive industry and to the world of academia. A large collection of research works on filament wound pressure vessels is available in literature, and a variety of models has been developed for the most diverse set of applications.

However, previous research frameworks have only been able to partly tackle all the different aspects which influence the laminate response during pressurization. Most studies compromise between achieving an accurate estimation of burst, or a precise prediction of the deformational behavior. This is caused by several reasons. Firstly, the complexity of the structural problem makes the detailed implementation of multiple effects tedious. Secondly, proper validation strategies are often difficult to develop. Expensive testing equipments are needed to reach the high operational pressure stages while simultaneously collecting relevant data on the vessel's deformational behavior. The result is often an uncomplete analysis, that does not allow to gain full understanding of the structural response.

The automotive industry is characterized by fast development times, meaning that quick results are needed in the design phase. In this tight time-frame, the vessel structure is often overdesigned to overcome the scarce understanding of the laminate response. This effect is particularly clear in the dome region of CPVs, where the material heterogeneities, the doubly curved geometry and the fastly changing ply orientation makes the region difficult to simulate, the computational times particularly high and the results tedious to interpret. For these reason, failure in this region cannot reliably be predicted. To avoid premature burst, domes are often over-reinforced, effectively increasing the overall costs of the tank system unnecessarily. In this context, a research gap becomes apparent as only limited work has been done on the development of a methodology useful for industrial purposes, which limits the computational expenses of the design process while ensuring reasonable accuracy of results for the prediction of burst in different design-critical areas of the vessel.

The main objective of the thesis work lays therefore in the construction of a computationally efficient, highly automated and robust numerical tool for the appropriate analysis of the structure of filament wound CPVs during pressurization. This shall be validated experimentally both in terms of deformational behavior and in terms of prediction of burst event. With this purpose, the main research question is formulated as:

*How accurately can numerical models simulate the deformational behavior of CPVs and how can these be used to predict the burst event both in the cylinder and in the dome region of the vessel?*

To answer this research question, a series of subquestions is defined:

- *How can existing simulation frameworks be extended to achieve low computational cost and high accuracy of results in the depiction of the structural behaviour of CPVs?* - Several approaches to answer this question are elaborated in Chapter 3 and Chapter 4, whereas the outcome of such strategies are

presented in Chapter 5.

- *Which parameters influence the simulated laminate response and how can these be adjusted to achieve a realistic prediction of the deformational behavior and burst of CPVs?* - This question is mainly answered in Chapter 4, where the sensitivity of the simulation to the variation in the material and geometrical definition of the vessel is addressed.
- *Based on the correlation between the observed vessel performance and the numerically simulated response, how accurately can burst pressure and failure location be predicted?* - Chapter 5 addresses this question thoroughly by correlating experimental and simulation results to evaluate the performance of the developed simulation tools to predict burst in different regions of the vessel.
- *How can the developed tool be applied for design purposes, to simulate the deformational behavior and burst of CPVs?* - Again, the data to answer this question is presented in Chapter 5, whereas a detailed discussion is provided in Chapter 6.

The document is organized to answer this set of questions chronologically. In Chapter 3, the model construction is described alongside with an explanation of the numerical approaches to guarantee its stability and efficiency. In Chapter 4, a method for the adjustment of the vessel geometrical and material composition is proposed to account for the effects of manufacturing. In Chapter 5, the model is directly applied to the BL, BC and W2B vessel configurations to assess its applicability and robustness. The evaluation of the method is discussed in Chapter 6, where its potentials and limitations are outlined in detail. Finally, the conclusions of this study are described in Chapter 7, where the research questions are answered explicitly.

# 3

## Computationally Efficient Modelling of CPVs

The simulation software Abaqus is chosen for the development of the numerical model. This is a FEA modelling software widely available both in academia and often used for industrial applications. Abaqus uses the open-source coding language Python, allowing the implementation of parametrized scripts for the model generation and processing. As introduced, the primary objective of this study is to develop a numerical tool for the analysis of composite pressure vessels, that can be applied for design purposes. In this framework, the developed analysis strategy must satisfy three main requirements:

1. It shall provide adequate accordance with the actual vessel behavior, as observed during pressurization and burst experiments;
2. It shall allow for fast computational time;
3. It shall be applicable to a wide range of vessel designs, which may not only differ from each other in terms of geometry and composition, but may also exhibit different deformational response and failure behavior when pressurized.

A separate discussion is necessary for each one of these three aspects.

### **Accuracy**

The required level of accuracy of a simulation framework varies according to the application. In detailed development phases, a high level of accuracy is often necessary to gain full understanding of the structure. For this purpose, earlier studies have focused on very detailed investigations that allowed to shed light on the laminate structure at microscopic level. However, this comes at high computational costs that realistically cannot be invested in an industrial context. When quick design decisions are needed, it is important to set a limit on the required level of accuracy, with the aim to obtain realistic results without excessively compromising on the computational efficiency of the model. This is only possible when the level of understanding of the CPV is high enough to reason and mitigate the discrepancies. A way to assess the acceptable level of accuracy relies on the comparison of the simulation results to the observed vessel response during pressurization. In this sense, it is assumed that the experimental data collected in the laboratory environment is representative of the vessel behavior during operation, despite in reality the former can be compromised by the limitation of the test setup itself. In any case, the smaller the discrepancy between the simulated response and the experimental results, the more accurate the numerical tool is said to be. To make the comparison reliable, the real-life vessel must be represented as closely as possible. Therefore, the effects of the manufacturing process and the time-dependent consequences of the pressure loading should be modelled appropriately.

### **Computational Efficiency**

The time efficiency of numerical simulations is a key aspect, as extremely detailed and yet too slow modelling tools are often discarded in the fast-paced automotive industry. Intuitively, the larger the model size, the longer the computational time. Therefore, the research and development (R&D) phase usually relies

on simplified models of reduced size, with the purpose to keep computational time at its minimum. Great effort must be spent to ensure that the model is scaled appropriately, such that the results obtained on a reduced-size vessel are representative of the actual CPV in operation. Furthermore, determining an acceptable simulation time requires an initial reference. To assess the computational efficiency of the developed modelling tool, its solving time is compared to that of the state-of-the-art simulation strategies. In this sense, an evaluation in terms of time-saving is performed.

### Robustness

The laminate structure, the vessel size, and even its geometry are likely to vary depending on the requirements of vehicle. For this reason, it is convenient to develop a model that is easily adaptable to different designs. In principle, it is not plausible to test the capability of the simulation strategy to any possible configuration, and it is also unrealistic to have the ambition to generate a model which can be adapted to any mandrel shape. On the other hand, significant effort is made to fully parametrize the model generation, solving and postprocessing of all data. This way the model can be applied to a great variety of vessel configurations, which may vary from each other in terms of size, layup, winding parameters and material composition. This does not only allow to automate and speed up the vast majority of the process, but also to test its capability to predict different failure types. In this case, the model is applied to the configurations presented in Chapter 2 to assess its robustness and its applicability to different designs.

Different strategies are applied throughout the research to guarantee the fulfillment of these three requirements. These span from numerical insights to physical adjustments to the vessel geometry and material definition. The first ones are explored in detail in this chapter of the document, whereas the second ones are described in Chapter 4.

## 3.1. Model Specifications

Within the Abaqus environment, it is possible to choose different modelling specifications to represent the vessel. Compared to previous numerical models as, for example, the one developed by Soriano [55], the purpose of this study is not to focus on the details of CPVs to an extreme degree of accuracy, but rather to generate fast results which represent realistically the laminate response without the need of manual modifications. For this purpose, two modelling strategies are investigated. The first one, based on solid elements, is built as an iteration to the work performed by Johman [32]. Specifically, several adjustments to the vessel geometry and material composition are implemented to better represent the laminate response. The second one, on the other hand, uses continuum shell elements to push the predictive ability of the model even further, to take into account the effects of damage propagation through the material without excessively compromising on the computational efficiency of the simulation.

In the following paragraphs, a brief description of both simulation strategies is provided as mean of familiarization with the assumptions that the different element formulations rely on. In both cases, the simulation is run in Abaqus/Standard, and the internal pressure is modelled as quasi-static load on the inner walls of the mandrel and of the boss. The geometrical specification of the vessel contour and the material composition of the laminate is kept constant for both simulations strategies.

### Solid Model

The implementation of solid elements to represent the through-thickness effects of pressurization is first inspired by the work performed by Soriano and Nebe et al. [10, 55]. A similar modelling technique is also applied in the research of Johman [32], where the level of through-thickness accuracy is conveniently traded in return of higher computational efficiency. As the purpose of this study is to keep reducing the computational time of the simulation while, at the same time, shedding light on some effects which improve its predictive abilities, the same element type is implemented. Specifically, the solid model relies on C3D20R elements, a quadratic formulation of the C3D8R element with three-dimensional translational degrees of freedom. This element type is able to capture the translation of each node in the three-dimensional space and translate it to a stress-state. It should however be noted that this formulation does not account for rotational degrees of freedom, meaning that the model tends to overestimate the bending stiffness of the structure. The quadratic formulation is chosen to improve the through-thickness refinement of the mathematical integration. Finally, the last letter R of the element name stands for *reduced integration*, selected to limit the detrimental effect of the propagation of hourglass deformation modes.



### Continuum Shell Model

The choice of developing a second model which relies on continuum shell elements is founded on the objective to quantify the impact of material degradation due to damage progression during pressurization. In principle, this could also be implemented within a solid model. However, this would require the development of a user-defined (UMAT) subroutine for the definition of the material composition of the vessel which is beyond the purpose of this research. Not only UMAT subroutines are very complicated to develop, but their implementation on three-dimensional solid models typically leads to extensive computational times, which are not useful for the purpose of this study.

An accurate depiction of the effects of damage through the material thickness, on the other hand, can be achieved for shell elements by implementing a material degradation subroutine in-built in Abaqus. Subsequently, continuum shells are chosen over conventional shells as they are able to discretize a three-dimensional body similarly to solid elements, allowing to use the same pre-processing steps as for the solid model. Therefore, the generation of the solid of revolution presented in Section 3.2 and the definition of a per-cell composite layup which accounts for layer thickness specifications are the same for both element types. This makes the modelling strategy easily adjustable to different numerical formulations according to the desired application.

The selected element type in this case is the so-called SC8R, a quadrilateral continuum shell formulation. As for the solid model, reduced integration is used to limit hourglass deformations, which in this case can also be controlled manually by tuning the membrane and the bending hourglass stiffnesses.

As three-dimensional continuum solid elements, continuum shells only have translational degrees of freedom. On the other hand, their kinematic and constitutive behavior looks like that of conventional shell elements, without however accounting for rotational degrees of freedom. The disadvantage of using continuum shell elements as compared to solid elements is the neglect of the stresses in the radial direction of the vessel.

## 3.2. Model Size Determination

The computational time of a simulation is highly affected by the model size and the overall number of elements. However, reducing the amount of elements without reducing the model size inevitably leads to high element dimensions. This solution is unfeasible, as it reduces the number of integration points distributed over the geometry, therefore limiting the resolution of the numerical approach. The price of this strategy is therefore often linked to low accuracy of results.

For this reason, previous researches usually propose a reduction of the entire model size, without varying the element size. This way, high accuracy of results can still be achieved by keeping a high resolution. At the same time, the computational time of the simulation remains low, as effectively only a limited amount of elements is included. In pursuing this strategy, it is important to ensure that the small-scale model represents closely its large-scale counterpart, or, in other words, that the simulation is representative of and scalable to what actually happens in the CPV during pressurization. Numerical simulations offer the potential to impose certain conditions on the virtual structure such that this requirement is fulfilled. For the case of CPVs, a solution is elaborated in the next paragraphs and subsequently evaluated to assess its effectiveness in the reduction of the computational time.

### 3.2.1. Setup for Model Size Reduction

In most works, CPV models are built on the 90 degrees revolution of the vessel contour, as shown in Figure 3.1(a). In this case, the model is built in a cartesian coordinate system and the vessel size is reduced to  $1/8^{th}$  of its original geometry, significantly decreasing the amount of elements in the mesh. This particular solution has been widely implemented in the context of the Fuel Cell Development department at cellcentric GmbH, and it is therefore used as reference for comparison [32, 55]. In this case, the model size reduction is possible by imposing symmetrical boundary conditions along the outer cross-sections of the vessel, parallel to the principal x-, y- and z-axis of the cartesian coordinate system. This is illustrated in Figure 3.1(a). The symmetrical boundary conditions constrain translational and rotational degrees of freedom in the direction where the material is removed.

A better alternative to achieve fast computational time consists in imposing a smaller angle of revolution for the generation of the vessel in Abaqus. Potentially, the angle of revolution can assume any arbitrary value, keeping in mind that the smaller the chosen revolve angle, the faster the computational time of the simula-

tion. An example for a revolution angle of 30 degrees is displayed in Figure 3.1(b).

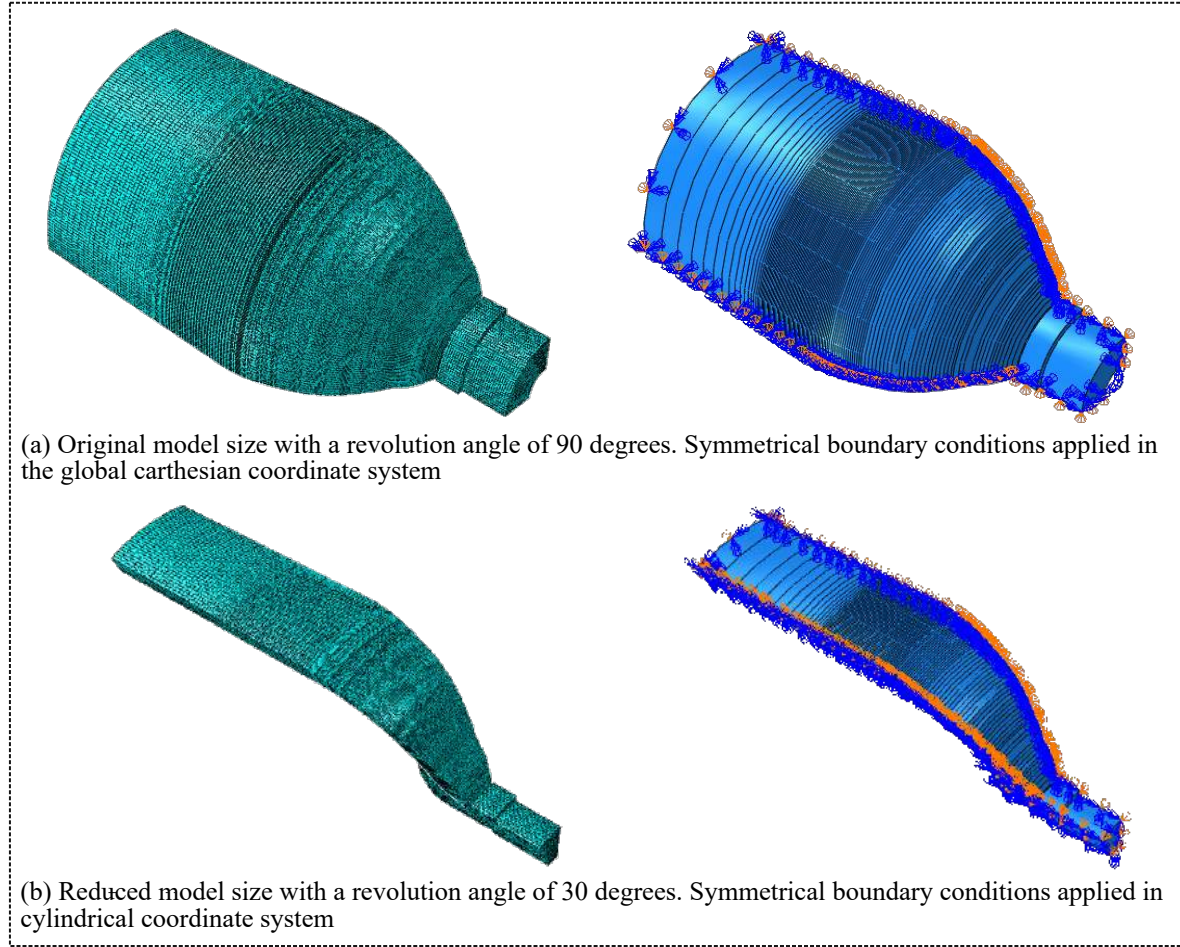


Figure 3.1: Graphical representation of the model with reduced size (b) as compared to the most widely used 1/8th vessel solution (a).

### 3.2.2. Method for the Adjustment of the Model Geometry

To generate the solids of revolution presented in Figure 3.1, two main inputs must be fed into Abaqus. The first one consists of the coordinates of the laminate profile, from which the solid geometry is created. This is done in a fully-parametrized manner, meaning that potentially any vessel shape can be analyzed, provided that the loading on the structure is adjusted accordingly. The laminate contour does not only depend on the number of plies included in layup, but also on the stacking sequence. In fact, this controls the compaction of the laminate and therefore its thickness, as further explained in Chapter 4.

The second required input is a set of coordinates describing the boss transversal cross-section. This structural element corresponds to the metallic base of the liner, which connects the tank to the other components of the vehicle or, alternatively, to the testing setup. The shape of the boss may vary according to the application. For this reason its generation is also fully parametrized. This guarantees the robustness of the process and its applicability to different configurations. However, it should be noted that large modifications of boss shapes have not been tested as throughout this research the boss geometry is kept constant, and consistent with that attached to the liners used for the experimental sets.

Both the vessel and the boss profiles are sketched in the  $xz$ -plane. The contours are then revolved around the longitudinal axis of the vessel (which corresponds to the  $x$ -axis in the global coordinate system) according to the user-defined revolution angle. Once the solid parts are created, tie connections are established between the composite material and the metallic boss.

Conveniently, boundary and loading conditions are defined in a cylindrical coordinate system which does

not require the planes of symmetry of the vessel to be aligned to the principal x-, y- and z- axis. In the established coordinate system, the origin corresponds to the origin of the global cartesian coordinate system, the radial direction corresponds to the original y- and z-axis, the tangential direction is chosen in the direction of the revolution angle and the longitudinal direction is aligned with the global x-axis. Also in this case, symmetry conditions are applied. Here, these are defined in the cylindrical coordinate system. They constrain the tangential and longitudinal displacement to simulate the effect of the missing geometry and ensure that the model size reduction does not compromise the validity of the results.

### 3.2.3. Relevance of the Model Size Reduction Approach

Two main aspects are considered for the assessment of this size-reduction procedure:

1. The results of the simulations should not be affected by the reduced number of elements that the model is now composed of.
2. The re-modification should yield to a decrease in computational time.

An investigation which involves different solids of revolution is performed to verify the first objective. Specifically, six versions of the same vessel configuration are modelled, which only differ from each other in terms of revolution angle. The results of these six simulations in regards to outer strains and per-ply stresses are then compared. For sake of conciseness, Figure 3.2 only reports the outer strains as a function of the axial coordinate along the mandrel profile, depicted in grey in the plot. The figure shows clearly that by performing the adjustments described above, reducing the revolution angle has negligible impact on the results of the simulation. In fact, the strain curves of the different simulations overlap perfectly, confirming that the results are not affected by the vessel size reduction and by the change in coordinate system. The similarity in the results is also seen in the comparison of per-ply stresses.

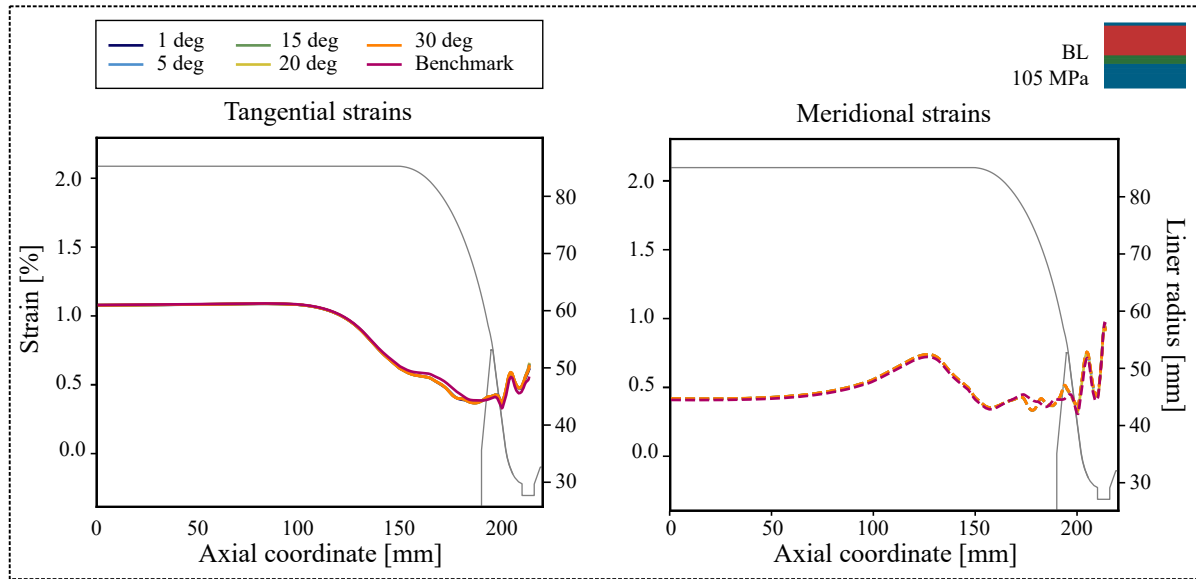


Figure 3.2: Outer tangential (left) and meridional (right) strains obtained through the revolution of the BL vessel configuration according to a selection of 7 revolution angles, and direct comparison with the 90 degree revolution benchmark

For completeness, the results are also compared to those of the original modelling strategy in the cartesian coordinate system, marked as *benchmark* in Figure 3.2. Again, the comparison shows limited differences in the estimation of the deformational behavior. These discrepancies are mainly attributed to the slight differences in boss geometry, which is now generated directly from a finite set of coordinates in Abaqus. This causes a partial decrease of the refinement with respect to the original part generated by the CAD software Siemens NX.

With the purpose to assess the model size reduction, the computational times of each simulation are compared. An overview is provided in Table 3.1 and Figure 3.2 for the BL vessel type. As the investigation is not dependent on the stacking sequence, similar results are gathered for the BC and W2B configurations. In

Revolution angle [deg]	CPU Time [Min]	Wallclock Time [min]
1	5.01	3.10
5	7.49	3.53
15	17.61	5.92
20	21.23	6.38
30	25.70	7.78
90	76.95	21.15

Table 3.1: Overview of computational times for several configurations which differ from each other in terms of angle of revolution. All data refers to the BL vessel configuration.

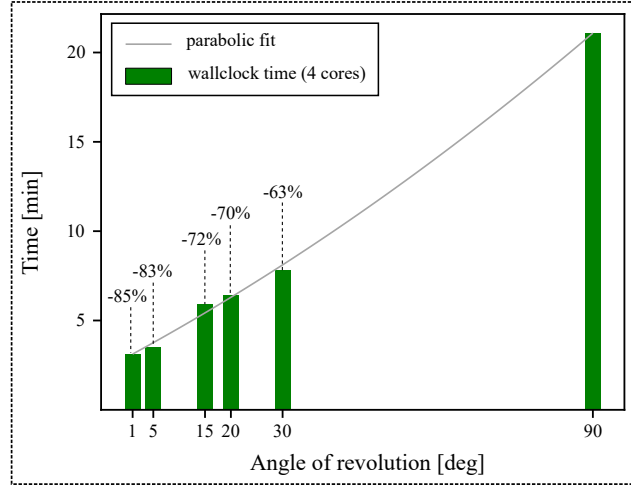


Table 3.2: Computational time for geometries with increasing revolution angles, and respective time reduction with respect to the  $1/8^{th}$  vessel benchmark. All data refers to the BL vessel configuration.

Table 3.1, the CPU time corresponds to the comprehensive computational time that the simulation needs in order to complete a run, whereas the wallclock time corresponds to the running time of the simulation with the available processing setup. In this case, the parallelization of 4 cores working simultaneously reduces the running time of the simulation of 85%. The wallclock time is used throughout this thesis as measuring standard, as the same PC and set of cores is used for every simulation.

Although potentially any revolution angle can be selected, drastic reductions of the revolution angle below 5 degrees are unadvised. Important fluctuations of results are found in proximity of the boundaries, which makes it necessary to extract the results at adequate distance from these locations. For clarity, an example is provided in Figure 3.3(a). Figure 3.3(b) shows how the path for data extraction should be chosen to avoid the significant scatter caused by the boundary effects. It should be noted that the choice of showing shear stresses as well as the selected ply in the figure are arbitrary, as all results appear to be affected by the described boundary effects.

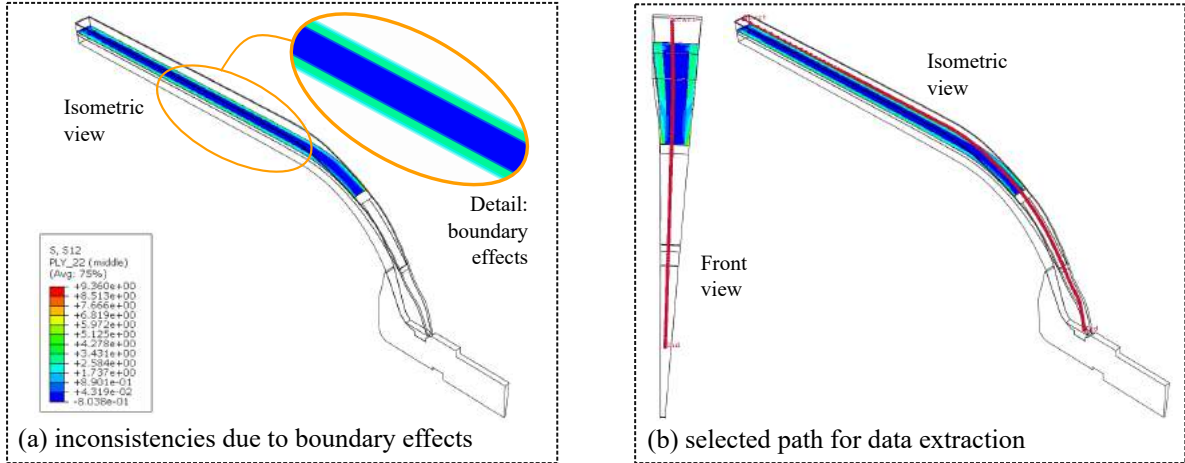


Figure 3.3: Numerical inconsistencies in proximity of the edges of the vessel geometry, due to boundary effects

### 3.3. Partitioning Methods

Throughout this study, a partitioning strategy is developed to tune the number of axial and through-thickness elements according to the application of the model. When, for example, high level of accuracy is required to analyze per-ply effects, a high number of partitions can be implemented to increase the number of elements

through-the-thickness. This increases the amount of nodes at which the constitutive equations are solved and improves the associated model resolution. On the other hand, when fast computation is preferred and generally realistic results are acceptable, the number of elements can easily be decreased.

### 3.3.1. Through-Thickness Partitioning

To facilitate the partitioning procedure, the user input is required before modelling to establish the number of through-thickness elements. This number corresponds also to the number of solids of revolution which will be generated in Abaqus, or in other words, to the number of sub-laminates that the vessel is discretized into.

Each ply is then associated to a specific sub-laminate according to the stacking sequence. The coordinates of the inner and outer contours of each sub-laminate are derived directly from the raw geometry prediction provided by the winding software Composicad. These sets of coordinates are subsequently input into Abaqus to sketch the sub-laminate profile on the xz-plane. The profile is then revolved according to the selected revolution angle as explained in Section 3.2. This procedure originates as many solids of revolution in Abaqus as many through-thickness elements the user has requested to have. In this sense, each solid of revolution consists of only one element through-the-thickness. The separate sub-laminates are then joined together by means of tie constraints. A graphical explanation is provided in Figure 3.4, where a per-ply-group discretization is chosen for the BL configuration. In this case, each element only contains layers of the same type (i.e. circumferentials, low and high angle helicals).

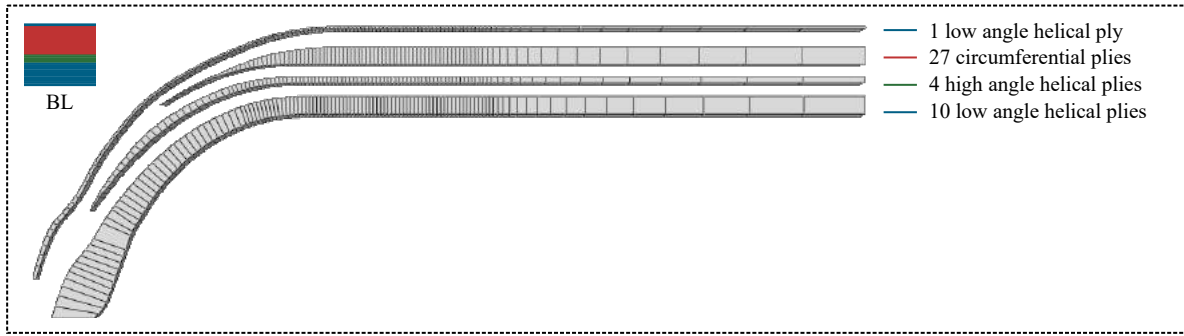


Figure 3.4: Through-thickness partitioning method to obtain a per-ply-group discretization for the BL vessel configuration.

### 3.3.2. Axial Partitioning

The axial partitioning of the model is determined within the Composicad environment. In this context, fundamental information regarding the thickness of each ply and its angle orientation is extracted at every discretization point along the longitudinal direction of the vessel. Intuitively, the higher the amount of discretization points along the contour, the more accurate the ply geometrical information.

For convenience, the same discretization points are then used in Abaqus to partition the model axially into different cells. The layup is assigned to each specific cell according to the ply information originated in Composicad. For mesh refinement purposes, seeds are then virtually placed at different intervals in each cells to guarantee an adequate level of resolution to each design-critical area of the vessel.

Within this study, it is decided to use 242 discretization points along the longitudinal axis of the vessel, which translates to 121 for the halved vessel modeled in Abaqus. The distribution of discretization points along the meridional direction of the liner is displayed in Figure 3.5 (a). This is not homogeneous as the required level of resolution is different for each area of the vessel. In the cylinder, the close-to-even ply thickness and the constant ply orientation allow for a coarser partition. Here, increasing the number of discretization points would only lead to heavier output files from Composicad and slower processing times in Abaqus without providing any extra information on the ply architecture. In the cylinder-dome transition region, on the other hand, a finer discretization is needed to keep track of the tapering of circumferential layers and the turnaround location of the high angle helical plies. In this region, ending plies experience a drastic change in thickness which increases at the turnaround point to then suddenly decrease to zero. Intuitively, different plies reach their turnaround point at different locations, meaning that a macroscopic tapering is also found along the vessel contour. To capture these phenomena, the density of discretization points in this region is

drastically increased, such that the information extracted from Compositcad is able to represent this gradual thickness variation smoothly.

Similarly, in the dome region, the approaching of low angle helical plies to their turnaround point causes a gradual change in ply orientation from the nominal cylinder angle to approximately 90 degrees. The rate of change in ply orientation is difficult to estimate but plays a substantial role in the stiffness distributon of this complex region. For this reason, the information provided from Compositcad is extremely valuable and must be as accurate as possible. In general, a higher density of discretization points is beneficial in the dome region.

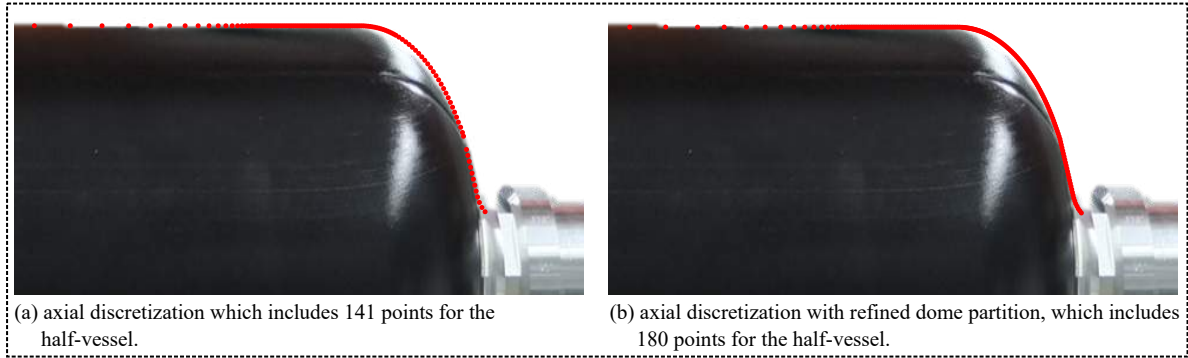


Figure 3.5: Coarse (a) and fine (b) distribution of discretization points along the mandrel contour.

### 3.3.3. Evaluation of Partitioning Strategy

This twofold partitioning method allows to achieve a wide range of model resolutions. The through-thickness partitioning strategy can be used to generate as many solids of revolution as many plies are in the laminate, eventually achieving a per-ply discretization. This is useful when high level of detail is required in the extraction of through-thickness effects. For convenience, the model is setup such that each element can only contain plies of the same type, meaning that the minimum number of through-thickness elements corresponds to the number of ply-groups, as displayed in Figure 3.4. Manual adjustments must therefore be made if a lower amount of solids of revolutions is preferred. Although this may be seen as a limitation, it effectively does not compromise significantly the validity of the method as it is found that a per-ply-group discretization leads to a valid combination of accuracy of results and computational efficiency. For this reason, most results in this document are retrieved for this configuration, unless stated otherwise.

In terms of axial partitioning, different configurations have been tested with the purpose to refine the Compositcad output which describes the thickness and ply orientation along the vessel's longitudinal axis. Among others, the one presented in Figure 3.5 (b) shows an iteration of the previously described 121-cells strategy. In this case, the number of discretization points in the cylinder-dome transition region and in the dome are doubled. The implementation of this strategy has shown to bring little improvement to the simulation results for the amount of computational effort necessary to process the data retrieved from the additional discretization points. For this reason, this configuration is discarded. However, its potential may become interesting if further adjustments to the vessel's contour are made in proximity of the boss neck. In fact, the finer discretization of the region could allow better tuning of the outer shape of the vessel.

## 3.4. Overview of Modelling Method

An overview of the entire modelling procedure is presented in Figure 3.6. The advantage of selecting either solid or continuum shell elements for the numerical formulation of the simulation is that the pre- and post-processing steps necessary for the model construction do not change.

Regardless of which element type is used in the Abaqus environment, the modelling strategy heavily relies on the output from the winding software Compositcad, which outputs a preliminary vessel geometry discretized along the meridional contour of the liner. This geometry, which includes a raw prediction of ply thickness and ply orientation, is then corrected to take into account the effects of compaction during winding according to the model proposed by Kang [31]. In the context of the compaction model, the laminate is partitioned through its thickness into sub-laminates. Each sub-laminate includes layers of the same type.



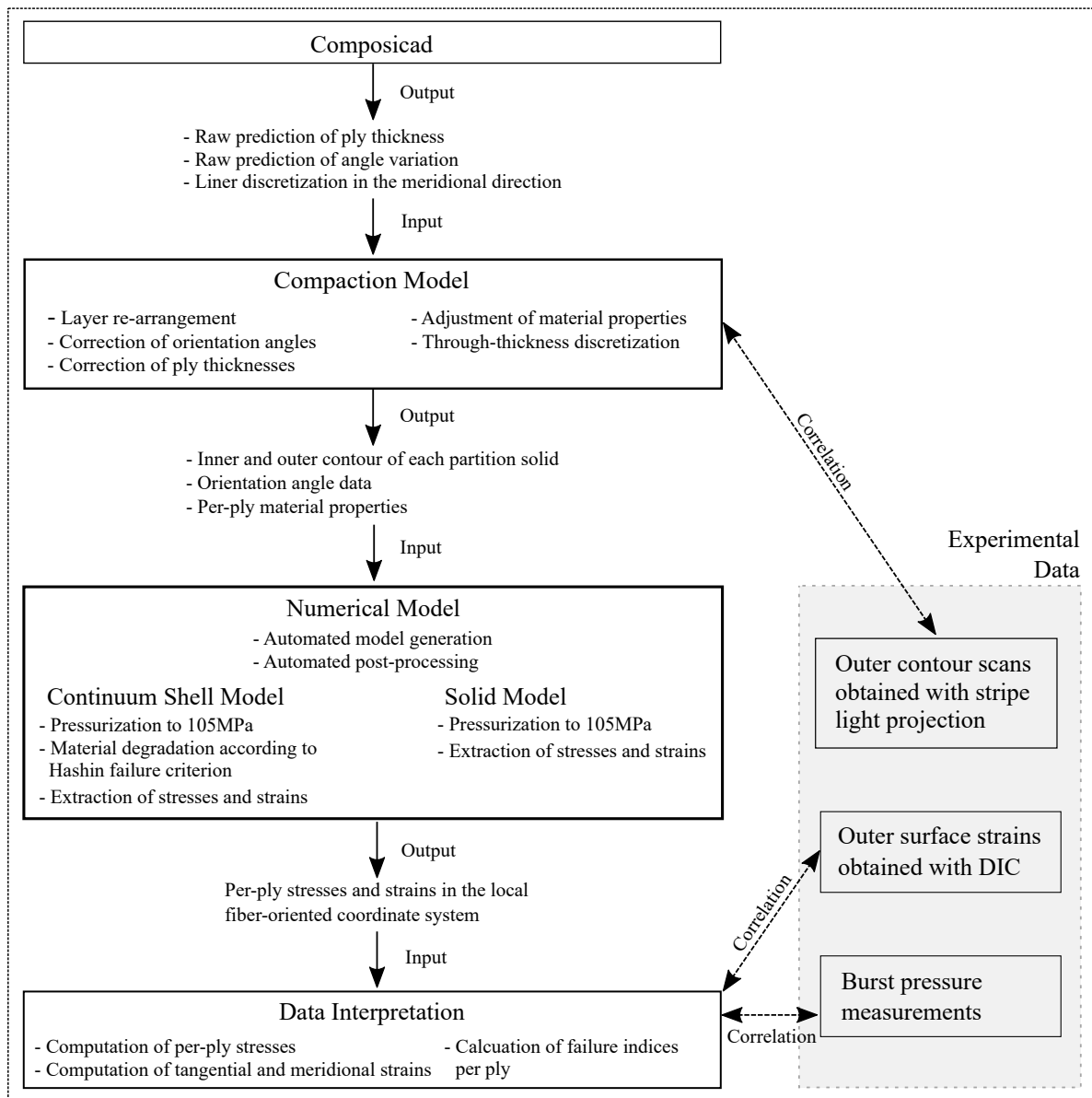


Figure 3.6: Overview of modelling strategy and correlation with experimental data

Furthermore, the material properties are adjusted to depict the heterogeneities caused by the different levels of compaction which every ply experiences.

The inner and outer contour of each sub-laminate and the material composition of each ply are then imported in Abaqus to generate the solids of revolution according the selected revolve angle and the desired through-thickness partitioning. Each solid is partitioned similarly along the length of the vessel to avoid sudden changes in mesh resolution. The number of cells in the meridional direction of the vessel depends on the level of discretization chosen in extracting the ply information from Compositcad. A specific number of seeds is then applied to each cell for mesh refinement purposes, to ensure that a high level of resolution is found in design-critical areas.

For both element formulations, the model generation follows the same fully-automated steps. In fact, the only difference resides in the selection of the element type. Depending on the application, the user may select whether a solid or continuum shell formulation is preferred. As explained, the first one is fully able to depict through-thickness effects and radial stresses in a fast-paced manner, whereas the second one enables to obtain results that consider the effects of material degradation due to damage.

Again, the post-processing of the simulation data and the generation of the model output is fully auto-

mated and similar for both modelling strategies. From this, the per-ply strains and stresses are computed not only in the local fiber direction, but also in the global tangential and meridional directions. Burst is then estimated by applying specific failure criteria to the stress-state at 105 MPa internal pressure. This corresponds to the highest pressure stage reached in the simulation.

Experimental data of different kinds are used throughout the whole modelling procedure to validate the simulation strategy. Firstly, the simulated vessel contour generated by the compaction model is compared to the contour scans obtained by means of stripe light projection. This ensures that the modelled geometry matches the manufactured counterpart. Furthermore, experimental strains obtained by means of DIC are used to evaluate the ability of the model to predict the deformational behavior of the vessel. Finally, data on burst allows to compare the burst pressure estimation to the actual pressure level reached during the experiments.



# 4

## Geometry and Material Definition of CPVs

The numerical strategies described in Chapter 3 do not yet account for many of the variables introduced in CPVs by the manufacturing process and by pressurization. For instance, the compaction applied during filament winding leads to a reduction of thickness as compared to the nominal prediction of the winding software. Furthermore, unexpected thickness accumulations occur at every ply drop-off location due to the dwelling of the winding machine. Material heterogeneities also develop through the laminate due to the different levels of compaction that every ply is subjected to. Finally, during pressurization the material is expected to degrade due to local damage, effectively diminishing the load-carrying capabilities of the vessel. These aspects influence the structure performance. Therefore, they must be taken into account to represent the laminate closely, resulting in a valid correlation between the simulation and the experimental data.

With this purpose, the geometry and the material composition of the vessel are studied in this chapter. Specifically, several approaches are developed to simulate the effects of filament winding on the laminate, and to study how the propagation of damage affects the performance of CPVs.

### 4.1. Geometrical Definition of Vessel Thickness

As introduced in Chapter 2, the geometry of the vessel is highly dependent on the manufacturing process. In this section, a series of adjustments is proposed to make sure that the simulated vessel geometry is representative of the filament wound CPV. These approaches rely on analytical strategies to mitigate the limitations of the winding software Compositcad in capturing the thickness build-up which results from filament winding. The outcome is then validated experimentally by comparing the adjusted vessel contour to the scanned profile obtained by means of stripe light projection.

#### 4.1.1. Description of Input Geometry

The fundamental input to the modelling strategy comes from the winding software Compositcad. By performing a series of calculations which take into account the robot motion during winding, the software computes two important pieces of information: first of all, the orientation of every ply at each axial discretization point along the length of the mandrel. For circumferential plies, this is straightforward as it remains constant throughout the entire surface over which the layer spans. Since circumferential plies are wound almost perpendicularly to the longitudinal axis of the vessel, they cannot extend over the cylinder-dome transition region, but are rather limited to the cylindrical part of the vessel. Here, the ply orientation remains constant and equal to approximately 88 degrees. This prevents the development of the high slip potential in the doubly curved region, as described in Chapter 1. On the other hand, the prediction of layer orientation is much more complex for helical plies. In this case, the ply orientation is constant in the cylinder, as shown in Figure 4.1(a). However, it changes rapidly in the dome where each ply approaches its turnaround point. As shown in Figure 4.1(b), the ply here needs to be perpendicular to the longitudinal axis of the vessel to allow for the necessary switch in winding direction. Estimating the rate of change in ply orientation is a rather convoluted task which is hardly measurable experimentally. A conspicuous set of measurements would indeed have to be recorded manually for each ply. This would come with all probability at low accuracy, due to the difficulties in inspecting by hand a complex and doubly-curved surface. For this reason, the output of the winding software is very important, as it provides the most realistic and easily attainable insight on the ori-

entation of each layer in the dome. However, some inconsistencies are found for both ply types, which can be adjusted by ensuring the following:

- All helical plies shall reach 90 degrees at the turnaround point. As shown in Figure 4.2(a), this is not always predicted by the winding software, which tends to lose track and underestimate the ply orientation in the dome region.
- All circumferential plies shall have constant ply orientation, set for consistency at 88 degrees with respect to the longitudinal axis of the vessel.

To guarantee these conditions, the orientation of each ply as function of the axial coordinate is adjusted as displayed in Figure 4.2(b) for the BL case. Similar adjustments are done for all configurations in analysis.

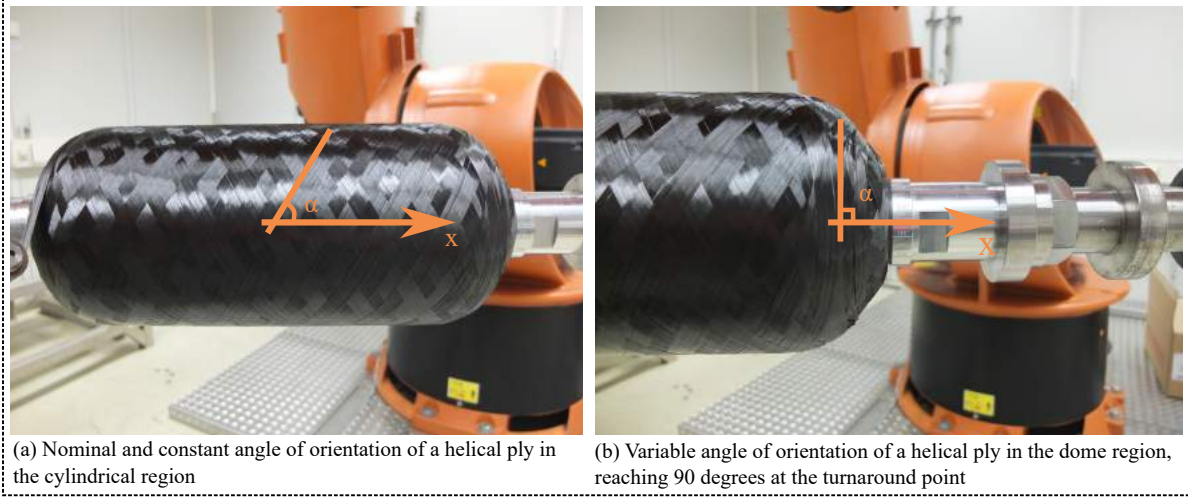


Figure 4.1: Ply orientation of a helical ply in the cylindrical region and in the dome of the vessel.

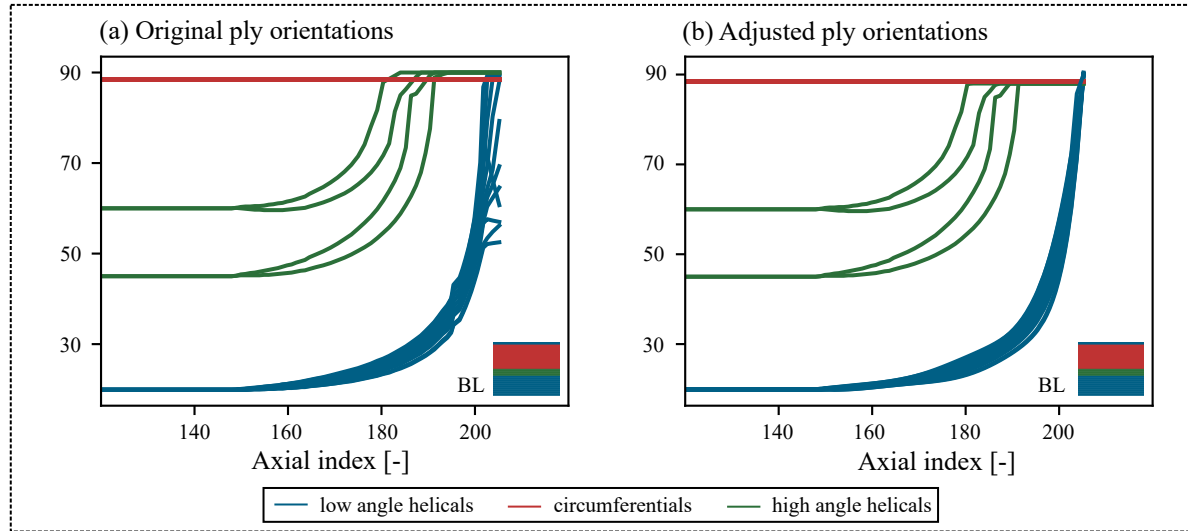


Figure 4.2: Overview of ply orientations as function of the axial location for the BL vessel configuration, as exported from Compositcad (left) and adjusted (right)

Another crucial output of the winding software is a first approximation of the layer thickness at every axial discretization point along the vessel length. Although important, the thickness approximation provided by Compositcad is not able to realistically depict the effects of compaction during manufacturing. These are mainly determined by the tension load imposed on the fibers during winding and by the thermal stresses which develop in the laminate during curing. Although the latter are beyond the scope of this investigation,

the former are accounted for by applying the compaction model proposed by Kang et al. [31] as described in Chapter 2. This model relies on the Composicad output because of two main reasons. Firstly, the thickness reduction it leads to is computed relatively to the initial thickness prediction of the winding software. Secondly, the normal tension load applied on the laminate is calculated as a function of the tension load on the fibers during winding and the orientation of each ply at every axial discretization point along the mandrel. Specifically,

$$F_n = F_t \cdot \sin(\alpha) \quad (4.1)$$

where  $F_t$  represents the tension imposed on the fiber during winding, and  $\alpha$  is the orientation of the specific ply.

The raw thickness output from Composicad is represented graphically for the BL case in Figure 4.3(a). This is far from realistic, especially in proximity of the ply-ends of circumferential and high angle helical plies. A first adjustment is proposed by Johman [32], who applies a layer re-arrangement procedure to generate the adjusted contour presented in Figure 4.3(b). His correction model is particularly relevant for the adjustment of circumferential plies, for which the contour at the ply-ends is corrected to obtain a realistic tapering in proximity of the cylinder-dome transition region.

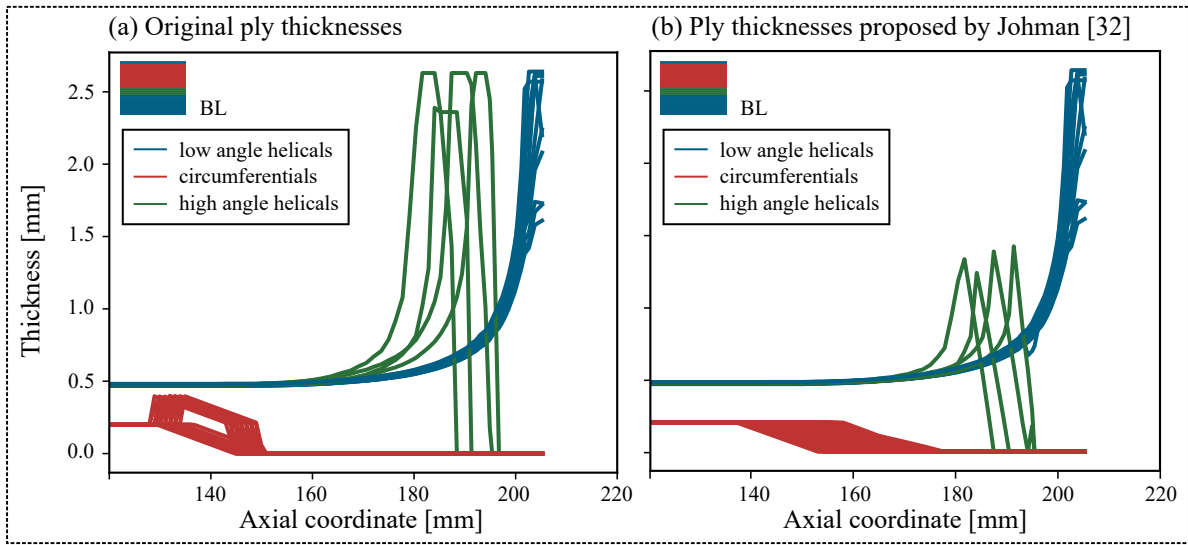


Figure 4.3: Overview of ply thickness as function of the axial location for the BL vessel configuration, as exported from Composicad (left) and as adjusted by Johman (right) [32]

When looking at the thickness accumulation in the dome of high and low angle helical plies as predicted by Composicad and displayed in Figure 4.3, one can notice that as each ply reaches its turnaround point, the thickness increases drastically and, in some cases, shows inconsistencies. Composicad is not able to estimate the thickness accumulation at the polar opening, probably due to the near-to-perpendicular layer orientation. This is mitigated by means of fitting functions that force the geometry contour to follow a certain curve to match the as-manufactured vessel contour. Although this approach leads to reasonable results for the adjustment of low angle helical plies, it appears to cause several numerical instabilities at the turnaround locations of high angle helical plies. For this reason, an alternative method is proposed in this study.

#### 4.1.2. Layer Re-Arrangement at Turnaround Points

As seen in Chapter 2, helical plies can be classified based on the orientation of their fibers in the cylindrical region of the vessel.

High angle helical plies typically extend only marginally into the dome, and reach their turnaround point right after the cylinder-dome transition region. This is due to the high ply orientations, translating into a large radii at which turnaround is possible at reasonable slippage.

The turnaround locations of high angle helical layers are important for the stress-strain distribution in the cylinder-dome transition region of CPVs. Once circumferential layers taper off at the cylinder end, high angle helical layers provide tangential reinforcement to ensure a gradual change in stiffness from cylinder to dome. Without these layers, the low angle helical plies would be exposed to high tangential stresses after

the circumferential ply drop locations. This would result in excessive local deformations, due to the high compliance of low angle helical layers in the tangential direction.

Given the importance of high angle helical plies in this region, it is fundamental to ensure a proper representation of their thickness profile. With this purpose, a mathematical approach is followed to adjust the predicted contour introduced in Figure 4.3.

The method relies on the main assumption that the amount of material estimated by the adjustment of Johman [32] is realistic. Graphically, this is represented by the area underneath the curve of the thickness profile of each ply as function of the axial location along the vessel length. Mathematically, this is computed as the definite integral of the thickness function, spanning from the origin (in this case the mid-point of the vessel length) until the turnaround point:

$$m = \int_0^{\text{turnaround}} t \cdot dx$$

Here,  $m$  represents the total cross-sectional area of material used. It is effectively a measure of its volume, as the fiber bandwidth remains constant regardless of the thickness accumulation. Furthermore,  $t$  represents the ply thickness and  $x$  the length along the longitudinal axis of the vessel.

Following this assumption, a second consideration is made regarding the unrealistic spike-like thickness prediction of Johman [32]. Although a thickness increase at the turnaround point is reasonable due to the dwell required to change the winding direction, it is unreasonable to assume that the thickness will reach its peak in a point-like manner. Due to the nature of the filament winding process and the geometry of the eyelet presented in Figure 2.5, several fiber tows are deposited simultaneously in the form of a fiber band. This suggests that a wider portion of surface will approach a similar thickness level at the turnaround point, as presented in Figure 4.4.



Figure 4.4: Bandwidth overlap at the turnaround location of circumferential plies.

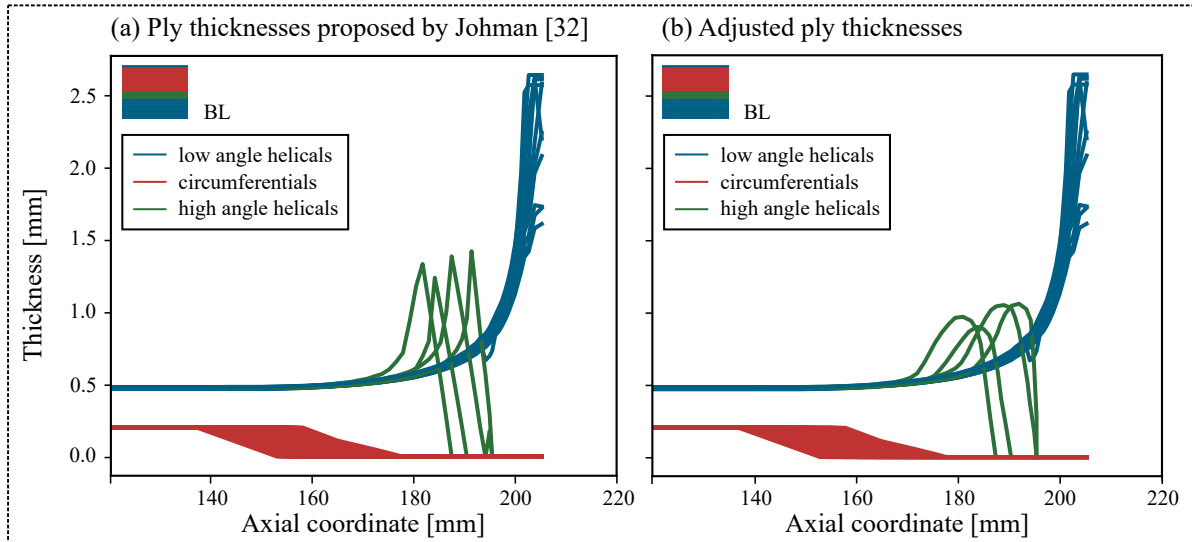


Figure 4.5: Overview of ply thickness as function of the axial location for the BL vessel configuration, as adjusted by Johman [32] (a) and adjusted (b).

A parabolic function is therefore fitted at the ply end of each high angle helical ply. This guarantees that the amount of material remains unchanged, and it defines a smooth vessel contour in the region. A graphical

representation of the parabolic fitting for the BL cases is presented in Figure 4.5, where it is directly compared to the initial estimation of Johman [32]. A similar approach is followed for all other vessel configurations.

The adjustment of low angle helical layers requires different considerations. The thickness approximation provided by Composicad becomes completely unrealistic as each ply approaches the pole, as presented in Figure 4.6(a) for the BL case. Therefore, an entirely new approximation is required. In the area of the dome adjacent to the boss neck, a remarkable increase in thickness is expected due to several aspects:

- The decreasing vessel diameter results in the deposition of more material. Here, an increase in thickness is necessary to reach a balance of volume across the length of the vessel.
- As the vessel is cured, the resin that squeezes out of the laminate in the dome region tends to slip along the curved surface towards the boss neck.
- As for high angle helical plies, the dwell which allows the eylet of the winding machine to rotate and invert the winding direction causes a local thickness increase.

To allow for these effects, the thickness profile of low angle helical plies is adjusted by fitting a sixth-degree polynomial function to the innermost low angle helical ply. This is forced to reach the boss neck by following the fitting function from the location where the profile predicted by Composicad begins to deviate. The plies above follow a similar trend: the thickness of each ply is calculated according to the sixth-degree fitting function and subsequently added to the contour of the laminate underneath. A comparison between the original contour predicted by Composicad and the result of this adjustment is presented in Figure 4.6 for the BL case.

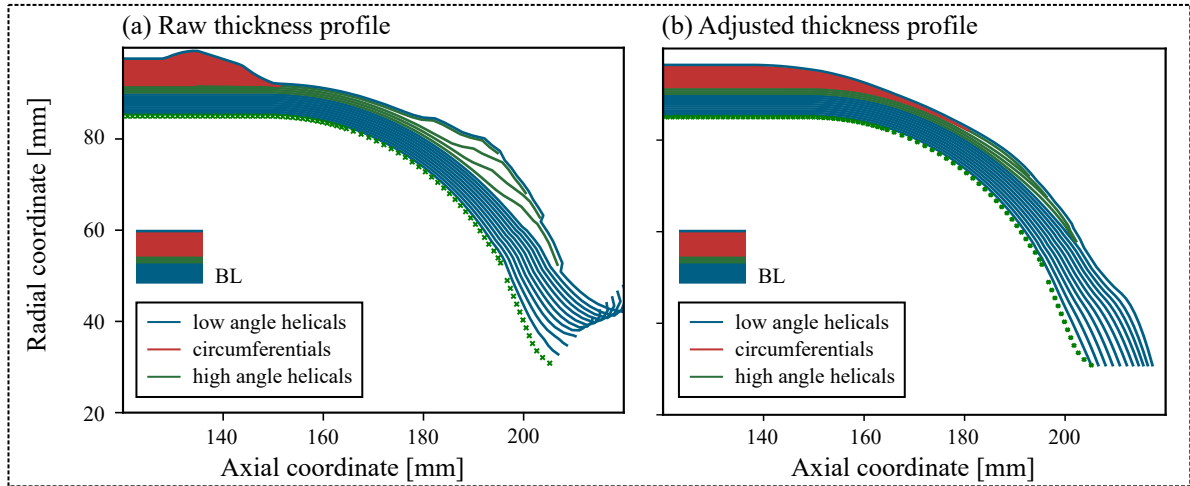


Figure 4.6: Comparison between vessel contour estimated from Composicad (a), and adjusted (b).

#### 4.1.3. Comparison with Measured Vessel Contour

To evaluate the accuracy of the thickness adjustment procedure, the corrected vessel profile is compared to that measured experimentally by means of stripe light projection. For completeness, the results of this correlation are presented respectively for the BL, BC and W2B cases in Figure 4.7, Figure 4.8 and Figure 4.9. The relative tables report the difference in total laminate thickness between the simulated and the experimental results in different areas.

In case of BL, good accordance is achieved in the cylindrical region of the vessel, where the Kang compaction model [31] plays the most relevant role for the determination of the laminate thickness. In fact, according to Equation 4.1, the higher the ply orientation the higher the tension load on the laminate. Therefore, even if a higher tension load is applied to helical plies during winding, the highest compaction is caused by the circumferential plies in the cylinder.

High accuracy of results is also found in the cylinder-dome transition region, proving the validity of the layer-rearrangement of high angle helical plies.

In proximity of the boss neck, on the other hand, realistic results are yet to be achieved as the measured thickness profile appears to be thicker for most tested cases. A possible explanation for the larger thickness

Region ID	Discrepancy [%]
I	2.83
II	2.62
III	2.25
IV	21.11

Table 4.1: Overview of the deviation between predicted and measured vessel contour for the BL configuration.

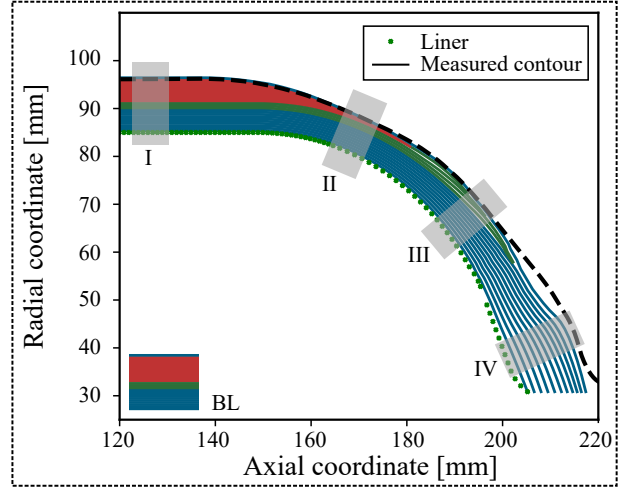


Figure 4.7: Graphical comparison between adjusted and experimental vessel profile for the BL case.

Region ID	Discrepancy [%]
I	0.90
II	0.04
III	0.10
IV	36.65

Table 4.2: Overview of the deviation between predicted and measured vessel contour for the BC configuration.

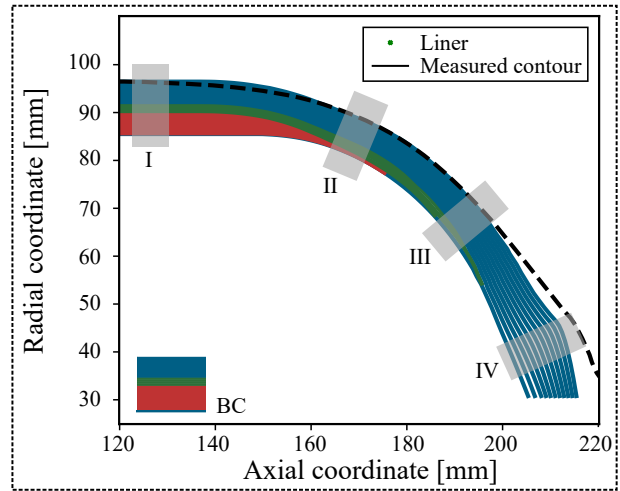


Figure 4.8: Graphical comparison between adjusted and experimental vessel profile for the BC vessel configuration.

Region ID	Discrepancy [%]
I	1.42
II	1.89
III	1.54
IV	4.07

Table 4.3: Overview of the deviation between predicted and measured vessel contour for the W2B configuration.

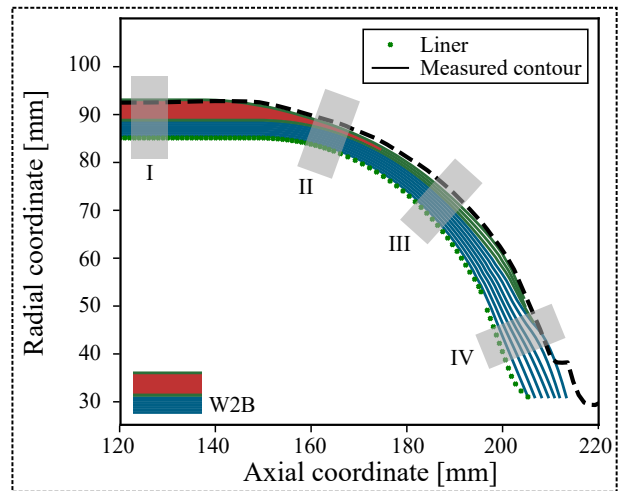


Figure 4.9: Graphical comparison between adjusted and experimental vessel profile for the W2B vessel configuration.



profile in this region is the accumulation of resin in this area. While this leads to a significant thickness discrepancy, its impact is deemed as minor in simulations, as the accumulated resin only partly contributes to the mechanical response of the CPV. Nonetheless, further investigations are necessary to verify this hypothesis. Overall similar accuracies are achieved for the BC and W2B configurations. The amount of material close to the boss neck appears to be underestimated in all cases.

#### 4.1.4. Evaluation of Vessel Geometry Adjustments

The fitting model implemented for the adjustment of the thickness profile of the vessel accurately depicts its as-manufactured geometry, although different areas of the vessels are better represented than others. In this case, the largest correction is made to the ply-ends of high angle helical plies.

The approach described in this document allows to smoothen the vessel contour by implementing a gradual parabolic fit under the assumption that the material accumulation predicted by Johman [32] is realistic. This makes the stiffness increase along the vessel length much less sudden, effectively reducing the numerical inconsistencies found in the FE environment. Overall, the adjustment of high angle helicals is representative of reality, although a few limitations should be noted. Firstly, it is an engineering solution to a physical problem. In reality, the parabolic fitting of the thickness curve is not verified and there exists no certainty that it corresponds closely to the actual build-up that helical plies experience during manufacturing. Furthermore, as explained in the previous section, the ply-ends of low angle helicals is still roughly represented and needs to be refined by means of microscopic insights.

## 4.2. Material Properties Definition

Compaction does not only affect the geometry of the vessel, but also its material composition. The different levels of consolidation experienced by each ply during winding generate a gradient in porosity through the laminate thickness. Porosity represents the density of air voids trapped in the resin constituent of the composite. These reduce the surface contact between matrix and fibers, therefore reducing the load-transfer capabilities of the resin. When the laminate is compacted, the air voids are partly removed, decreasing the porosity locally and increasing the fiber volume fraction. This phenomenon results in an enhancement of material properties, as better adhesion is ensured between the fiber and the matrix constituents.

In filament wound CPVs, each ply experiences a different level of compaction based on to aspects:

- Its own orientation- the higher the fiber orientation as measured from the longitudinal axis of the vessel, the higher the level of compaction.
- The compaction inferred by the 3 plies directly above it.

Therefore, porosity varies through the thickness, leading to a variable fiber volume content. This effect is presented in Figure 4.10, which shows the CT scan of the cross-section of a BC vessel following curing. The plies located on the inside of the laminate experience low porosity, thanks to the high compaction imposed by the stack of circumferential plies above. On the other hand, a higher density of air voids is found in the outer plies, meaning that the laminate here is more porous. The outer plies are compacted less, due to the low orientation of helical layers and the absence of an overlaying compacting layup. This gradient in porosity results in varying material properties which vary through the laminate thickness.

This chapter presents in detail the method followed for the adjustment of the material properties, to take into account these through-thickness heterogeneities. First, the purpose of the adjustment is presented alongside the assumptions that it relies on. This is followed by a thorough explanation of the mathematical procedure and its validation process. Finally, the validity of the model is assessed and its assumptions reviewed.

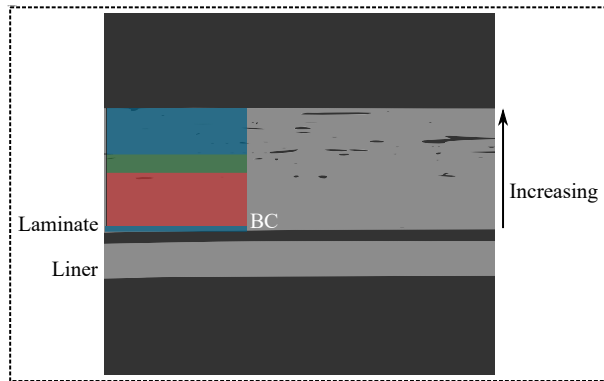


Figure 4.10: CT scan showing the material heterogeneity caused by compaction in a BC vessel configuration.

### 4.2.1. Effect of Compaction on the Definition of Material Properties

The geometrical adjustments presented in Section 4.1 result in an accurate depiction of the vessel contour, which takes into account the impact of compaction on the vessel geometry. However, an important limitation is worth mentioning: reducing the laminate thickness without accounting for a change in material properties leads to a drastic decrease of the load-carrying capabilities of the laminate. In fact, the thickness reduction translates to the removal of composite material in the FE model, as schematically shown in Figure 4.11. In reality, the opposite happens. When compacting the laminate, its fiber volume fraction increases as its porosity decreases. As mentioned, a scarce density of air voids through the laminate favors adhesion between matrix and fibers, enhancing the mechanical properties of the material. Therefore, when accounting for compaction, it is necessary to adjust the mechanical properties accordingly, as otherwise the compaction model would lead to an underestimation of the laminate stiffness caused by the thickness reduction. For simplicity, in Figure 4.11 the load-carrying material is displayed in blue, without differentiating between fibers and matrix.

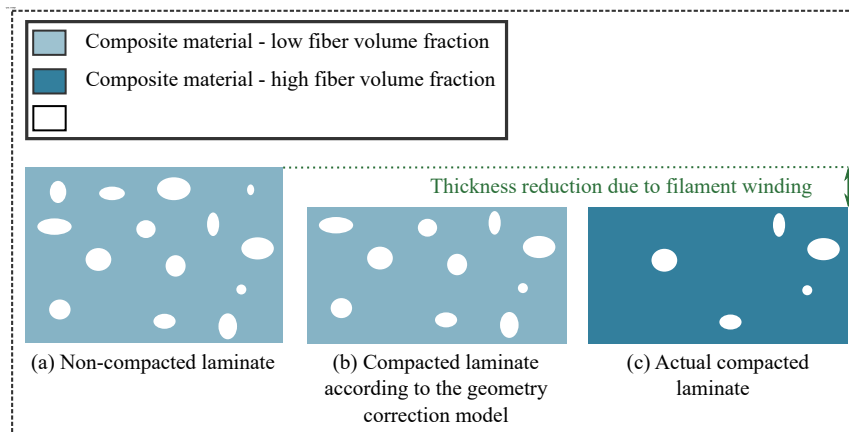


Figure 4.11: Schematic graphical depiction of (a) non-compacted laminate thickness and composition, (b) thickness reduction and material composition as assumed by the geometry correction model and (c) actual thickness reduction and material composition

To mitigate this effect, an engineering procedure for the adjustment of material properties is developed. This relies on the assumptions listed below:

1. **The amount of composite material deposited on the mandrel as estimated by the winding software Compositcad is realistic** - In all tested cases, the estimated vessel weight matches the measured weight of the manufactured vessel. Therefore, it is assumed that the Compositcad estimate is representative of reality also for non-tested cases.
2. **All material deposited on the mandrel during winding will remain on the mandrel after curing** - The curing process does not involve the addition of any consumable which would cause squeez-out or absorb the excess resin on the surface. Furthermore, no spilling of resin is detected in the oven for any of the tested cases. Therefore, it is reasonable to assume that the material deposited on the mandrel does not decrease during curing. In reality, it is possible that the fluid resin material would relocate during the curing process, especially since the vessel rotates with respect to its longitudinal axis when placed in the oven. This has the potential to cause irregularities in the material distribution, which are however discarded for sake of simplicity.
3. **Classical lamination theory (CLT) applies to the laminate** - The approach is based on CLT, meaning that each ply is considered to be homogeneous in properties and in state of plane-stress. Furthermore, the deformation of the laminate can be described by means of the Kirchhoff-Love approximation for extension and bending of thin plates [58].
4. **In-plane stresses constitute the most relevant loading case for composite pressure vessels** - As explained in Chapter 1, CPVs are mainly subjected to radial loading, which cause the laminate to expand tangentially. This causes high in-plane stresses, which exceed significantly the out-of-plane meridional bending stresses at the cylinder-dome transition region, and the through-thickness shear and radial stresses.



### 4.2.2. Engineering Approach for the Adjustment of Per-Ply Properties

The main steps of the methodology followed for the adjustment of material properties are summarized in Figure 4.12.

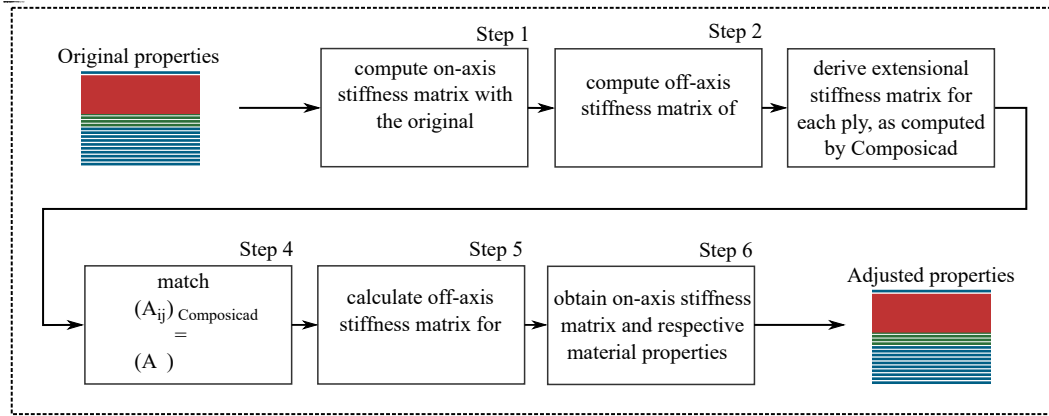


Figure 4.12: Flowchart describing the material adjustment procedure.

The input is the geometry and material definition of the non-compacted laminate. This is compacted by means of Kang's model [31] to simulate the thickness reduction caused by fiber tension during winding. For the compacted laminate, the on-axis stiffness matrix is calculated from the original material properties provided by the material manufacturer as follows:

$$Q_{12} = \begin{bmatrix} \frac{E_1}{1-\nu_{12}\nu_{21}} & \frac{\nu_{12}E_2}{1-\nu_{12}\nu_{21}} & 0 \\ \frac{\nu_{21}E_1}{1-\nu_{12}\nu_{21}} & \frac{E_2}{1-\nu_{12}\nu_{21}} & 0 \\ 0 & 0 & G_{12} \end{bmatrix} \quad (4.2)$$

Here,  $E_1$  corresponds to the longitudinal modulus of elasticity of the material in tension,  $E_2$  to its transverse modulus of elasticity and  $G_{12}$  to its shear modulus.  $\nu_{12}$  and  $\nu_{21}$  correspond to the Poisson's ratios respectively in the longitudinal and transverse directions of the fibers. The on-axis stiffness matrix  $Q_{12}$  describes the stiffness of each ply in an orthotropic coordinate system where the 1-axis is aligned with the orientation of the ply's own fibers. A graphical representation is provided in Figure 4.13(a). This is then converted to the global xy-coordinate system where, in the case of composite pressure vessels, the x-axis is aligned with the longitudinal axis of the vessel, as presented in Figure 4.13(b).

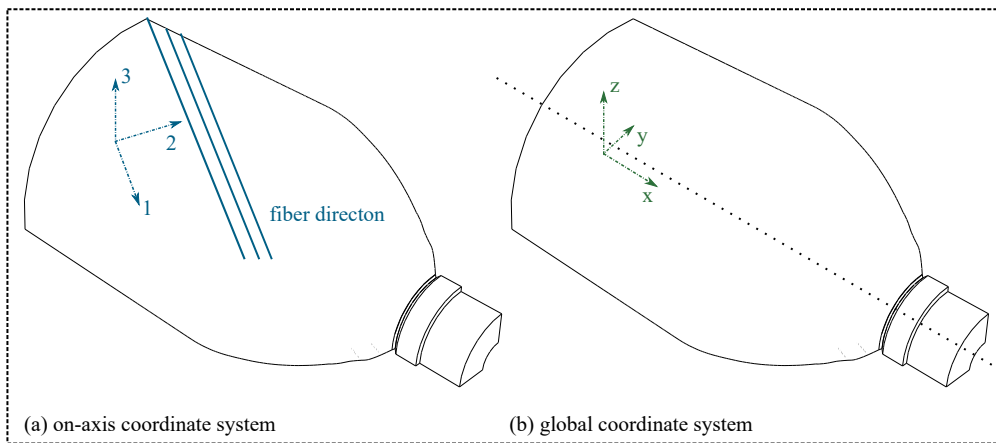


Figure 4.13: Schematic representation of on-axis and global coordinate systems.

A transformation is performed to rotate the stiffness matrix  $Q_{12}$  to the global coordinate system:

$$Q_{xy} = T^{-1} \cdot Q_{12} \cdot T \quad (4.3)$$

where,

$$T = \begin{bmatrix} \cos^2(\alpha) & \sin^2(\alpha) & 2\sin(\alpha)\cos(\alpha) \\ \sin^2(\alpha) & \cos^2(\alpha) & -2\sin(\alpha)\cos(\alpha) \\ -\sin(\alpha)\cos(\alpha) & \sin(\alpha)\cos(\alpha) & -\sin^2(\alpha)\cos^2(\alpha) \end{bmatrix} \quad (4.4)$$

Here, angle  $\alpha$  corresponds to the orientation of the ply measured in the cylinder with respect to the global x-axis. Once the off-axis stiffness matrix  $Q_{xy}$  of each ply is known, the element of the extensional stiffness matrix  $A$ , those of the extension-bending coupling stiffness matrix  $B$  and those of the flexural stiffness matrix  $D$  can be calculated according to CLLT as:

$$\begin{aligned} A^{ij} &= \sum_0^n Q_{xy_k}^{ij} t_k \\ B^{ij} &= \sum_0^n Q_{xy_k}^{ij} t_k^2 \\ D^{ij} &= \sum_0^n Q_{xy_k}^{ij} t_k^3 \end{aligned} \quad (4.5)$$

where  $t$  is the ply thickness,  $n$  is the total number of plies and  $k$  is the inde of the ply in analysis.  $i$  and  $j$  refer to the row and column entry of the specific matrix.

The compacted stiffness matrix  $Q_{xy,compacted}$  can only be adjusted according to one of the relations in Equation 4.5. In this case, the laminate is mainly subjected to the in-plane stresses inferred by the radial loading stretching the layers. Therefore, mainly the elements of the  $A$  matrix are relevant. Furthermore, selecting the  $B$  or the  $D$  matrix would lead to an overestimation of the material properties, as the thickness terms in Equation 4.5 are respectively squared and cubed. For this reason, the  $A$  matrix of each ply in its non-compacted state is matched to the  $A$  matrix of the same ply in the compacted state as follows:

$$A_{k,original} = A_{k,compacted} \rightarrow Q_{xy_k,original}^{ij} t_{k,original} = Q_{xy_k,compacted}^{ij} t_{k,compacted} \quad (4.6)$$

For each ply, as the thickness reduces due to compaction and the elements of the  $A$  matrix are kept constant, the elements of the  $Q_{xy}$  matrix of the compacted laminate must increase for Equation 4.5 to apply. The elements of the updated stiffness matrix  $Q_{xy}$  are therefore computed as follows:

$$Q_{xy_k,compacted}^{ij} = \frac{A_{k,original}^{ij}}{t_{k,compacted}} \quad (4.7)$$

The procedure is performed separately for each ply, as each ply has its own specific thickness and it is compacted to a different extent. This material adjustment attributes the highest increase in material properties to the most compacted plies, and viceversa, as the stiffness matrix  $Q_{xy}$  and the compacted ply thickness  $t$  are inversely propotional according to Equation 4.5. The off-axis matrix  $Q_{xy}$  of the ply is then rotated back to its own on-axis coordinate system. This is done by means of the same transformation matrix  $T$ , presented in Equation 4.4:

$$Q_{12} = T \cdot Q_{xy} \cdot T^{-1} \quad (4.8)$$

As seen in Equation 4.2, the on-axis stiffness matrix  $Q_{12}$  is composed in each term of a combination of material properties, featuring the stiffness in the principal loading directions and the associated Poisson's ratios. Therefore, these can be back-calculated by solving a system of equations which associates each entry of the calculated  $Q_{21}$  stiffness matrix to the material properties.

The results are presented for the BL, BC and W2B configurations in Figure 4.14. For each case, the thickness reduction of each ply in the cylinder is presented on the left hand-side, whereas the corresponding increase in longitudinal elastic modulus is presented on the right hand-side. The three ply types are displayed in different colors. Finally the distance of each ply from the liner is presented on the horizontal axis of the plot, where the origin corresponds to the innermost ply.

In the case of BL, the group of circumferentials plies is placed on top of the stack of helical plies, towards the outside of the laminate. This causes high compaction in the cylinder, resulting in a drastic reduction of the laminate thickness. As presented in Section 4.1, the level of compaction of each ply depends on two aspects: its own orientation and the orientation of the 3 plies directly above.

Because of the first, circumferential plies experience a higher level of compaction, and therefore a more drastic thickness reduction. This is due to Equation 4.1, which suggest that a high fiber orientation translates to a higher normal force on the laminate.

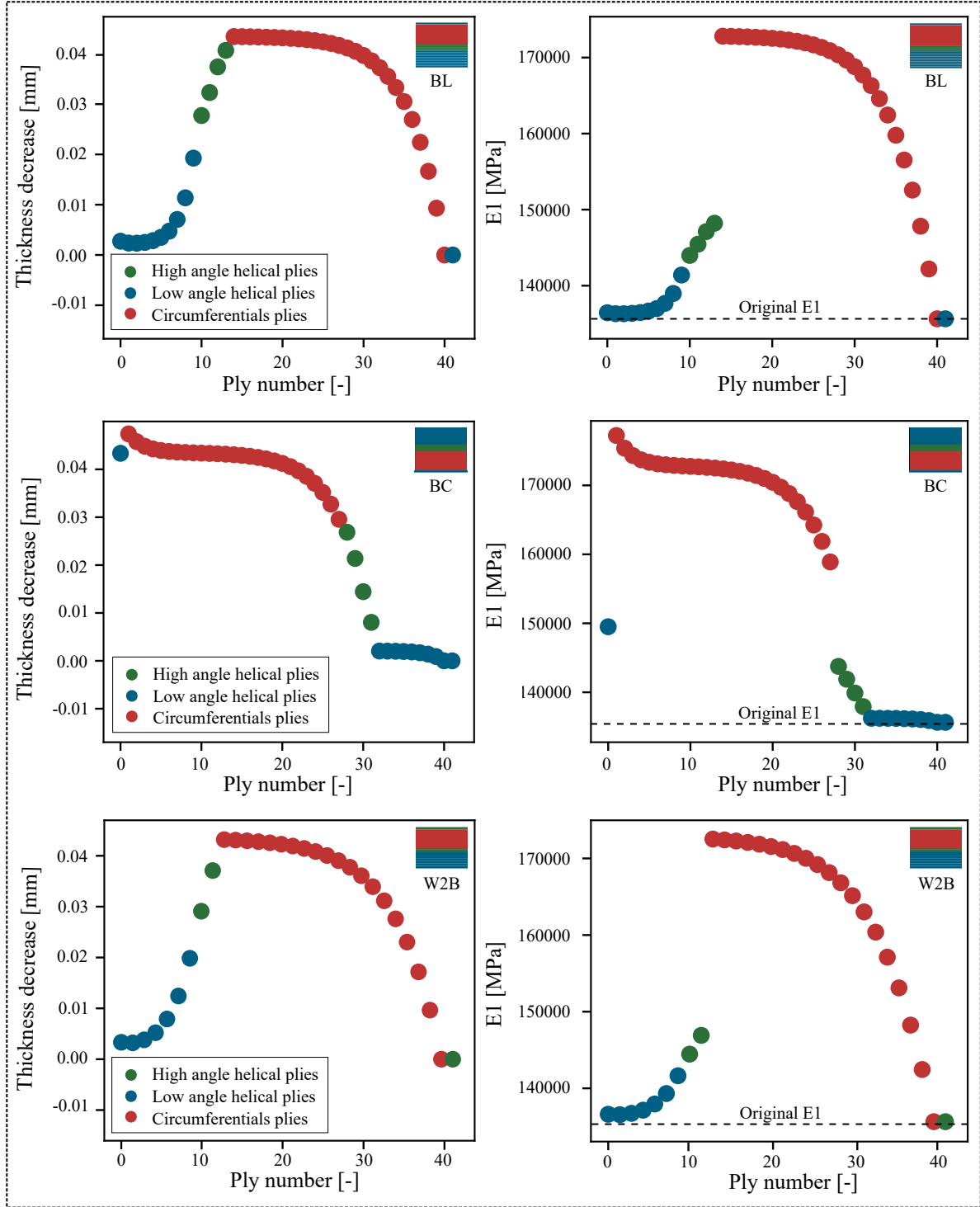


Figure 4.14: Results of cylinder compaction and of the material adjustment procedure in terms of (a) per-ply thickness reduction, and (b) per-ply increase in longitudinal modulus in the cylindrical section of the vessel.

The second indicates that the level of compaction is most significant for the innermost circumferential ply, as the 3 plies directly above are also heavily compacting due to their high orientation. The innermost circumferential ply therefore experiences the most relevant increase in stiffness. Similarly, the increase in material properties becomes negligible for the outermost ply of the laminate. Another implication of the second consideration is the relatively low increase in material properties experienced by innermost low angle helical plies, despite their position at the bottom of the laminate. Intuitively, one could expect these plies to

be highly compacted as more plies are wound subsequently on the vessel. However, this is not the case. The innermost low angle helical ply of the BL configuration, for example, experiences low compaction due to its low fiber orientation, and due to the fact that the three plies directly above it are wound at low fiber orientations as well. Therefore, only the low angle helical plies right below the stack of circumferentials experience a significant increase in material properties, as these are affected by the compaction inferred by the high orientation of the plies directly above. The same considerations are valid for the W2B case, as effectively the two configurations have similar stacking sequences.

In the BC case, the situation is reversed. The innermost low angle helical ply is subjected to the high level of compaction inferred by the adjacent circumferential plies. In this case, the increase in material longitudinal modulus experienced by the high angle helical plies is also substantially lower, as these do not experience the influence of the compacting circumferential plies.

Although only the longitudinal modulus is shown in Figure 4.14 for the sake of conciseness, the transverse longitudinal modulus and the shear longitudinal modulus are also calculated accordingly and show similar behaviors. The choice of only displaying  $E_1$  is reasoned by the high impact that this property has on the deformational behavior of the vessel, which is in fact mainly subjected to in-plane stresses.

Increasing the material stiffness translates into a decrease of laminate strains experienced at the same loading level. This improves the load-carrying capabilities of the laminate and increases the stresses that the structure is able to carry. However, if the material strength is not adjusted properly, the procedure leads to a premature burst prediction, as the strength of the material would not be high enough to take on the increased stresses that the high stiffness attracts. For this reason, the strength of each ply is adjusted according to its relative increase in stiffness. For instance, if a specific ply experiences a stiffness increase of 15%, it is assumed that it will also experience a strength increase of the same relative amount.

### 4.2.3. Validation Approach

The described engineering approach is difficult to validate experimentally. First of all, assessing the level of compaction caused by the deposition of each ply would make the manufacturing process extremely long. CT scans and microscopy only partially mitigate this issue, as they allow to study the porosity of the laminate through-the-thickness. However, translating this porosity into the appropriate material properties remains tedious. In any case, a validation procedure is performed, which compares the calculated material properties of each ply to the results of an experimental set. These experiments are meant to test the material properties of laminates with different levels of compaction, whose fiber volume content spans between 50% and 65%. Although the method for the adjustment of the material properties leads to even higher fiber volume fractions, these are difficult to achieve experimentally. Therefore, only the results for fiber volume contents in this range can be validated.

The experimental set was performed in the same research group for a different investigation on composite pressure vessels, with the purpose to estimate the laminate material properties on meso-scale, under the assumption of homogeneous orthotropic material properties. To ensure good accordance between the specimens and the CPV, all samples were manufactured by means of filament winding. This way, it was possible to represent the consolidation induced by stacking sequence and fiber tension realistically. The specimens used for testing were manufactured according to ISO 527-4:1997 [59] for the determination of longitudinal and transverse characteristics, and according to ISO 14129:1997 [60] for shear properties. Unidirectional specimens were selected to represent circumferential layers as both are not intertwined.  $\pm 45$  helical layer were wound to investigate shear properties and to study the interwoven state. In total, the set consisted of 15 specimens for test type.

Different mandrels and tools were used to manufacture the unidirectional and the  $\pm 45$  degrees flat specimens. Unidirectional test plates were wound on a tailored metallic tool presented in Figure 4.15(a). This did not only set the specimen dimensions, but it also permitted the fitting of the side case that enforced layer consolidation. On the other hand,  $\pm 45$  degrees specimens necessitated of a longer tool, presented in Figure 4.15(b). This allowed to account for the variation in ply orientation in proximity of the turnaround points. The central parts of the specimens, away from the poles, were then cut to size and placed onto the same tool used for the unidirectional plates. This enforced the same level of consolidation during curing. Different levels of porosity were achieved by placing metallic shims between the case and composite material. The purpose of the shims was to increase the effective laminate thickness, to vary its consolidation level and fiber volume content.

A summary of the achieved levels of fiber volume fraction and porosity for all specimens is presented in

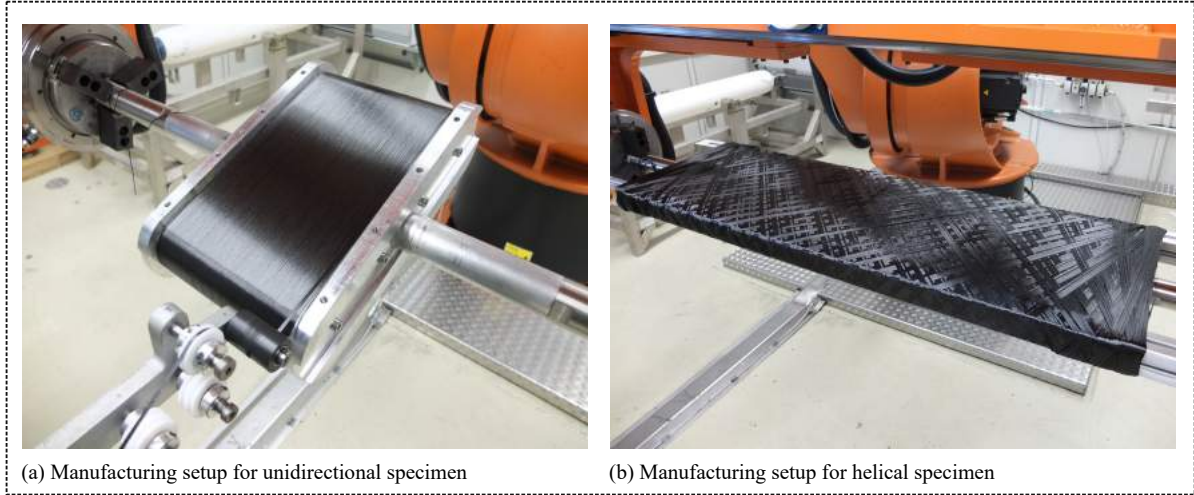
Figure 4.15: Overview of winding procedure for (a) unidirectional and (b)  $\pm 45$  specimen in their respective tailored metal mandrels

Table 4.4: Overview of fiber volume fraction and porosity of the each specimen.

Stack	Fiber-Volume	$n_f$	Fiber-Fraction [%]	Porosity [%]
[0] <sub>9</sub>	Low	5	$56.55 \pm 0.50$	$7.46 \pm 0.82$
	Medium	5	$59.57 \pm 0.7$	$1.55 \pm 0.66$
	High	5	$62.24 \pm 0.36$	$0.36 \pm 0.04$
[90] <sub>9</sub>	Low	5	$56.77 \pm 0.64$	$6.81 \pm 0.31$
	Medium	5	$60.02 \pm 0.36$	$2.60 \pm 0.43$
	High	5	$62.94 \pm 0.57$	$1.07 \pm 0.53$
[ $\pm 45$ ] <sub>5</sub>	Low	5	$55.01 \pm 5.23$	$5.65 \pm 1.93$
	Medium	5	$60.17 \pm 3.07$	$3.65 \pm 1.26$
	High	5	$62.90 \pm 1.31$	$1.31 \pm 0.72$

Table 4.4. These were obtained by means of acid digestion tests, after which the specimens were tested in the respective loading direction. Figure 4.16 shows the modulus of elasticity and the strength as function of the fiber volume content, as gathered from longitudinal tensile testing. Error bars are added to depict the scatter of the measured porosities. The elastic modulus is calculated by means of linear regression of the stress-strain curve points between 0.05% and 0.25% strain, assuming linear elastic behavior of the material. Interpolation functions are then fitted through the datapoints. In the case of longitudinal tensile testing, the interpolation function is linear for the elastic modulus and quadratic for the strength. This suggests that an increasing fiber volume fraction has a greater impact on the strength of the material, rather than its stiffness. The upwards trend of both material properties can be partly attributed to the decrease in cross-sectional area for the highly compacted specimens. This translates in higher stiffness and strength for the same applied load. A second aspect to play an important role in the stiffness and load-carrying capabilities of the laminate is porosity, which directly affects the compliance of the resin. High porosity compromises the ability of the matrix to efficiently transfer the loads between the different fiber bundles, therefore lowering the load-carrying capability of the laminate. Therefore, low porosity and sufficient amount of resin permits an efficient redistribution of loads and leads to a gradual failure. However, if the amount of resin is not sufficient, the load-transfer between the fiber bundles is compromised. This is a plausible cause for the non-linear behavior of the strength curve described by the specimens tested longitudinally.

The results for transverse tensile testing are presented in Figure 4.17. In this case, a purely linear behavior is assumed for both stiffness and strength, meaning that the cross-section of the specimen and the properties are directly proportional. The load-carrying capability of the laminate is directly affected by the quality of the matrix and of the fibers. In terms of stiffness, low fiber volume content suggests the presence of air voids in the matrix which reduce the effective laminate cross-section capable of withstanding the transverse loads. Strength is also mainly affected by the resin quality. Cracks tend to initiate in proximity of imperfections where the micromechanical load path is forced to deviate. This increases the stress concentration locally

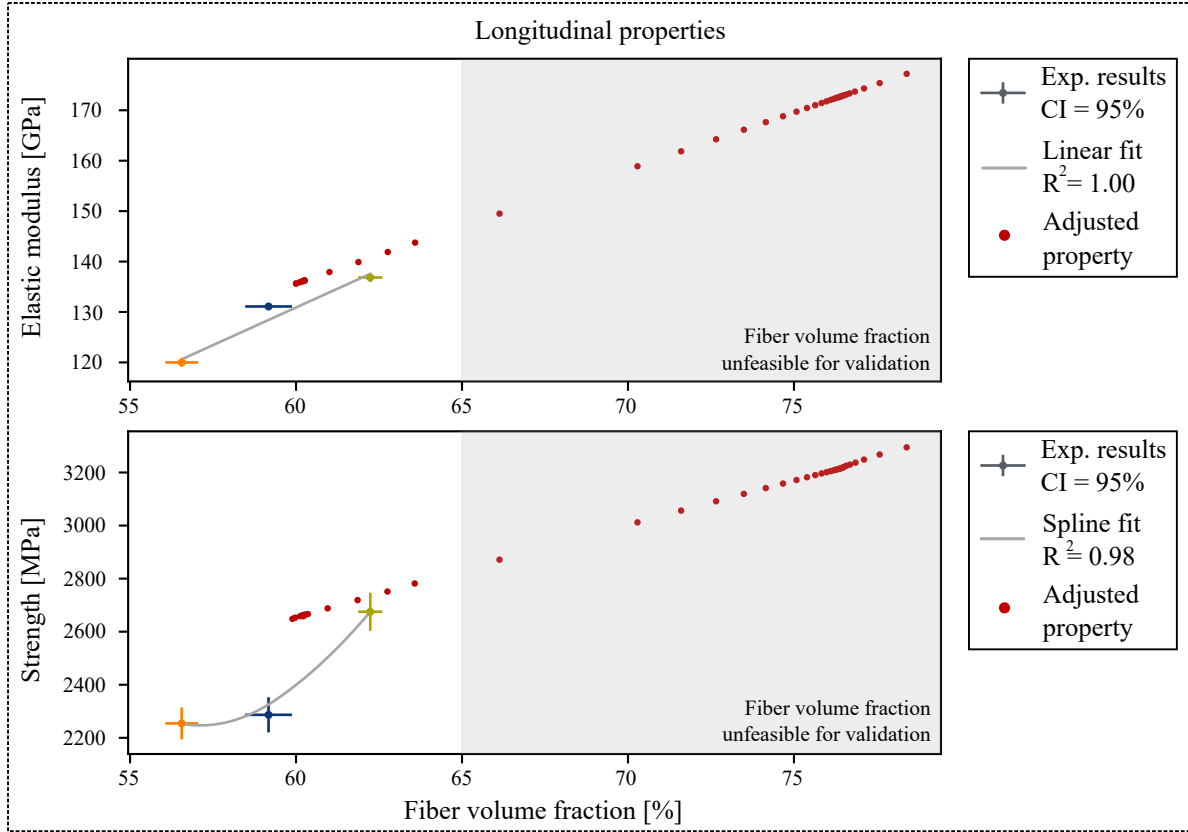


Figure 4.16: Elastic modulus and strength versus fiber volume content, as calculated by means of the material properties adjustment and as extracted from longitudinal tensile testing. A fitting function is used to fit the experimental data to extract material properties from the trend.

until failure. Therefore, the lower the fiber volume content, the higher the porosity. High porosity results in low failure strength.

Finally, the results of shear testing are presented in Figure 4.18, where the stiffness is calculated assuming an elastic response in the range between 0.2% and 0.6% strain. In this case, the estimation of porosity shows a significant scatter due to the varying material confinement imposed by the shims on the specimens. Stiffness is again highly affected by the amount of air voids, as matrix compliance is increased by the large amount of pores in the interwoven microstructure. On the other hand, strength is influenced by the constraints of the outer plies that induce premature failure on the inner plies.

The comparison between the experimental results and the adjusted material properties shows accordance for all considered loading cases when the fiber volume fraction ranges between 50% and 65%. This corresponds to the range of fiber volume fraction of the tested specimens. For higher fiber volume fractions, however, no validation data is available as there is a limit to the level of compaction achievable experimentally. Levels of fiber volume fraction above 65% are difficult to reach. The ranges of high fiber volume fraction for which no validation is possible are shaded in grey in the figures. In this regard, the comparison is only valid in the lower range of fiber volume fractions, and the fitted functions passed through the data are only representative in this window. In conclusion, the validation process presented in this section proves that the adjustment of material properties leads to reasonable results. In the range of fiber volume fraction where experimental results are available, the data matches rather closely the analytical results. For higher fiber volume fractions, however, experimental data cannot be fitted by means of monotonically increasing functions, and therefore a plausible correlation between the calculated and experimental results cannot be established.

#### 4.2.4. Evaluation of the Procedure for the Correction of Material Properties

The procedure presented for the adjustment of material properties is an interesting tool that allows to better model the stiffness and strength of the laminate at different levels throughout the thickness. Without the appropriate adjustment of material properties, correcting the geometry of the vessel loses a large part of

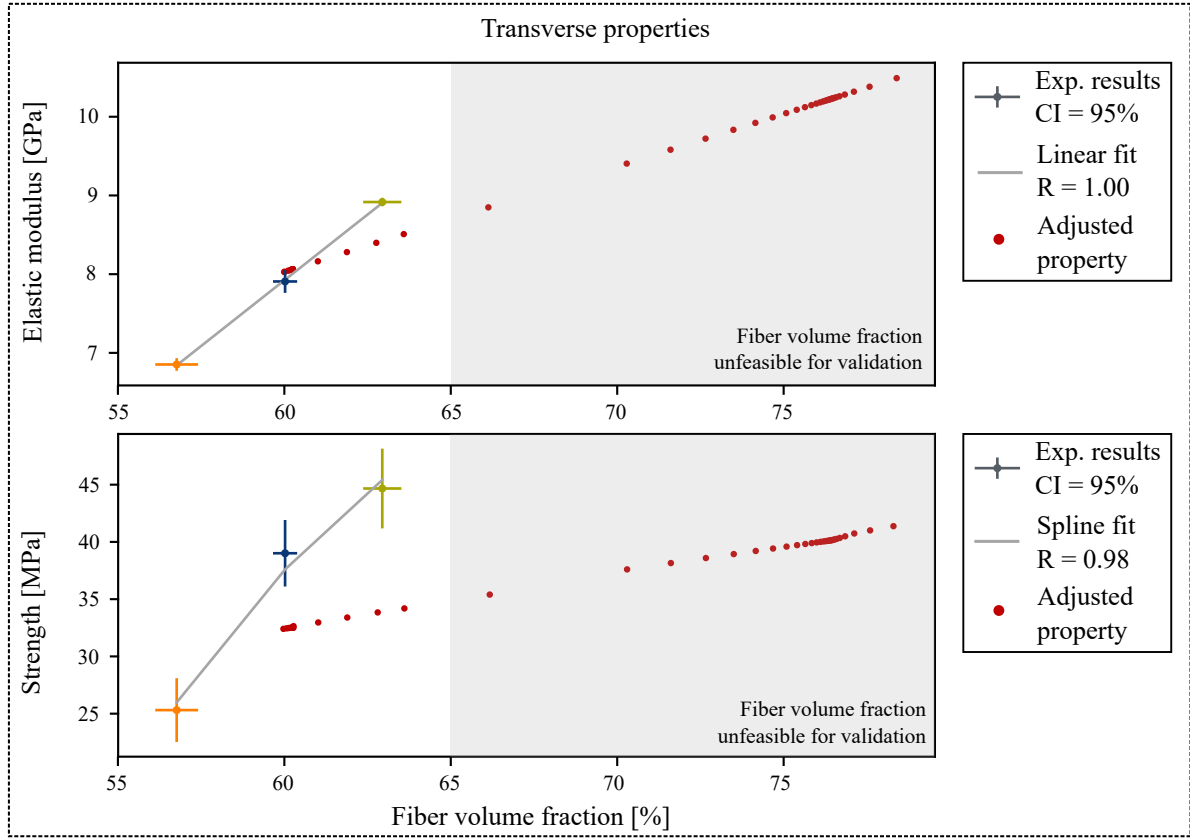


Figure 4.17: Elastic modulus and strength versus fiber volume content, as calculated by means of the material properties adjustment and as extracted from transverse tensile testing. A fitting function is used to fit the experimental data to extract material properties from the trend.

its purpose. What varies with the compaction model is not only the contour of the laminate, but also its overall stiffness, as this is directly affected by the reduction in thickness. The method presented in this section mitigates this limitation in an appropriate manner, as it provides an increase in material properties based on the main assumption that the total amount of load-carrying material does not vary when the compaction acts on the structure. This assumption seems to be reasonable, as it matches closely the material properties obtained experimentally at least for low-to-medium fiber volume contents.

Despite its clear achievements, the proposed strategy has some limitations:

- It is an engineering solution, and as such it has no physical meaning. Stiffness and strength are affected by the laminate quality and the presence of voids. However, modelling these aspects simultaneously is extremely complicated, and an engineering solution is a valuable option which has a similar impact on the simulations as that of compaction on the CPV.
- It is not easily verifiable by means of experimental techniques. The procedure is based on the thickness reduction of each ply during winding, which is however microscopic and therefore difficult to measure. Furthermore, these measurements should be taken subsequently after the winding of each ply to evaluate the influence of every layer on the compaction level of the underlying ones. This would require to interrupt the winding process often, potentially compromising the quality of the uncured material. CT scans and microscopy offer valuable alternatives, which however rely on expensive machines.
- Material properties are calculated only based on the level of compaction in the cylindrical section of the vessel. This is the most-compacted region as it corresponds to where the circumferential plies are placed. Furthermore, in this area the ply orientation is uniform, leading to constant material properties across the length of the entire cylinder. On the other hand, in the dome the level of compaction is rather low, as only helical plies are used to reinforce the liner. Here the material properties remain similar to the ones provided by the material manufacturer and assumed in previous investigations [32, 55]. In

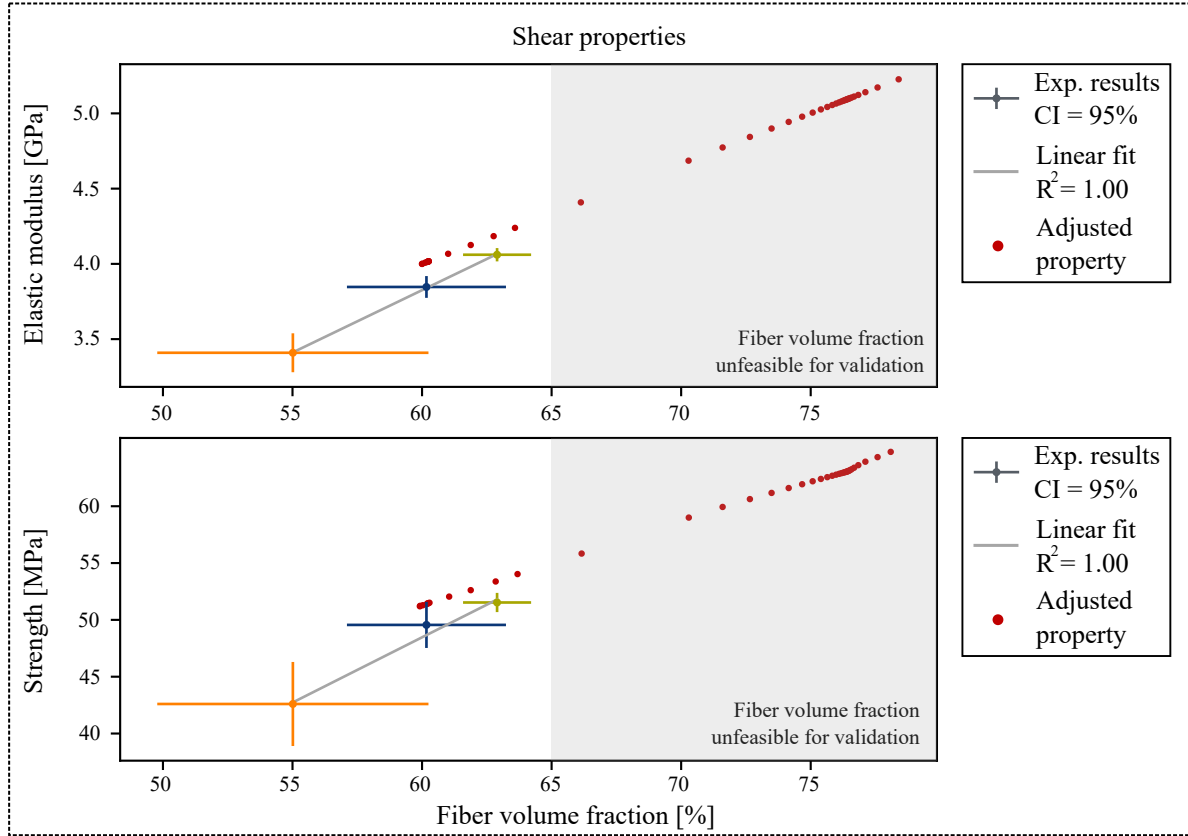


Figure 4.18: Elastic modulus and strength versus fiber volume content, as calculated by means of the material properties adjustment and as extracted from in-plane shear tensile testing. A mathematical function is used to fit the experimental data to extract material properties from the trend.

fact, the ply thickness here does not vary significantly. Furthermore, in the dome the ply orientation varies as the ply approaches the boss, reaching 90 degrees at the turnaround point. This makes the adjustment of material properties in the dome much more computationally expensive than for the cylinder case, as these must be calculated at every discretization point along the vessel contour. This would lead to material properties that not only vary per ply, but also per axial location. Adjusting the material properties in the dome as well as in the cylinder is potentially doable, and has in fact been done during the investigation to assess its benefits. However, in the dome the material properties vary only slightly at every point, making the computational expense not justifiable. It is therefore decided to proceed by adjusting the material properties only in the cylinder, where the impact is greater due to the high compaction imposed by the circumferential plies. This leads to a slight overestimation of material properties in the dome, which should be accounted for in the evaluation of the results. In any case, the option to adjust the material properties per ply and per axial location in the dome can easily be implemented in the model, as the script has already been parametrized for this function.

To further address the robustness of the method, the possibility to change the assumptions for the analysis of the dome are considered. Specifically, it is investigated whether it is true that in-plane loading is truly the most relevant loading case in this region. Here bending effects which develop in the cylinder-dome transition region and shear stresses also partly contribute to the laminate stress-state. In other words, one could argue that in this region the extensional stiffness matrix  $A$  may not be as important as the flexural stiffness matrix  $D$ , which could then be matched to that of non-compacted case to adjust the material properties. An investigation on the effects of this hypothesis is performed for sake of completeness.

As presented in Equation 4.5, the elements of the  $A$ -matrix are proportional to the ply thickness. On the other hand, the elements of the  $D$ -matrix are proportional to the cube of the ply thickness. This difference has an important implication: in the cylinder, the material properties would be unreasonably high if the  $D$ -matrix would be considered instead of the  $A$ -matrix in Equation 4.6. Furthermore, the assumption would



not be representative of reality as undoubtedly the most critical loading is found in the tangential direction for circumferential plies. In the dome, the thickness reduction is so small that the difference in results barely depends on the stiffness matrix. This makes the two approaches virtually equivalent in the dome region, whereas the advantages of adjusting the A matrix are clear in the cylinder. In conclusion, the approach based on the A-matrix is preferred as highly representative in the cylinder, and just-as-acceptable in the dome. It should however be noted that the adjusted material properties are slightly underestimated in the dome, due to the role played by flexural stresses on the laminate performance.

### 4.3. Propagation of Damage

The definition of material properties described in the previous section gives a realistic first representation of the heterogeneities already present in the laminate prior to pressurization. However, an iterative analysis is necessary to evaluate how the material degrades when loaded. With this purpose, a damage propagation analysis is implemented in the modelling strategy. The subroutine evaluates damage according to the Hashin Rotem failure criterion, following the mathematical formulations explained in detail in Section 4.3.1. The implementation in Abaqus follows the steps presented in Section 4.3.2.

The purpose of this method is to quantify the impact of damage on the deformational behavior of pressurized CPVs and the associated prediction of burst. Previous investigations have shown the potential of remarkably detailed damage progression subroutines in improving the simulation results, and to obtain a close estimation of burst [55]. However, these come at very high computational costs, especially due to the fine discretization that the formulation require. In fact, the analysis includes a per-ply discretization for a three-dimensional solid element model.

As the method developed in this study focusses on fast analysis, a more efficient approach is implemented. This is based on the progressive degradation of the material properties associated to continuum shell elements. With this approach, failure in each ply is analyzed individually. Two limitations should however be mentioned. First of all, as opposed to its solid counterpart, it does not take into account for the radial stresses through the laminate thickness, as continuum shell elements utilize a two-dimensional tensor formulation. Secondly, as multiple plies are included in a single element, the degradation of the material properties of each ply influence the overall damage variable of the entire element. In turn, the element may reach failure before its individual plies fail. A finer through-thickness partitioning has the potential to lead to more accurate results, as effectively the failure of each element would be better representative of the failure of all of the plies in its layup. For this reason, a sensitivity analysis is performed and presented in Appendix A. The outcome of this procedure shows that refining the model discretization only leads to a very slight improvement, proving that plies of the same type tend to experience similar levels of damage. To limit the computational time of the simulation, it is therefore decided to continue with the original partitioning strategy which includes one through-thickness element per ply-group.

#### 4.3.1. Mathematical Description of Hashin Rotem Failure Criterion

The mathematical formulation of the damage progression subroutine relies on two phases: damage initiation and damage evolution. Damage initiation refers to the onset of material degradation and it is evaluated in Abaqus by applying Hashin Rotem theory [61]. This criterion considers four damage mechanisms: fiber tension, matrix tension, fiber compression and matrix compression. For each one of these phenomena, a failure index is calculated to evaluate whether damage has initiated:

$$F_f^t = \left( \frac{\sigma_{11}}{X^T} \right)^2 + f \left( \frac{\tau_{12}}{S^L} \right)^2 \rightarrow \text{Fiber tension: } \sigma_{11} \geq 0 \quad (4.9)$$

$$F_m^t = \left( \frac{\sigma_{22}}{Y^T} \right)^2 + \left( \frac{\tau_{12}}{S^L} \right)^2 \rightarrow \text{Matrix tension: } \sigma_{22} \geq 0 \quad (4.10)$$

$$F_f^c = \left( \frac{\sigma_{22}}{X^C} \right)^2 \rightarrow \text{Fiber compression: } \sigma_{11} < 0 \quad (4.11)$$

$$F_m^c = \left( \frac{\sigma_{22}}{2S^T} \right)^2 + \left[ \left( \frac{Y^C}{2S^T} \right)^2 - 1 \right] \frac{\sigma_{22}}{Y^C} + \left( \frac{\tau_{12}}{S^L} \right)^2 \rightarrow \text{Matrix compression: } \sigma_{22} < 0 \quad (4.12)$$

Failure is triggered in one of the four damage mechanisms when the respective failure index  $F$  is equal to or exceeds 1. In the equations, subscripts  $T$  and  $C$  denote tension and compression respectively,  $X$  refers to longitudinal strength values,  $Y$  to transverse strength values and  $S$  to shear strength values. Factor  $f$  represents the contribution of the shear stress to the fiber tensile initiation criterion, which in this case is set to 0 to be consistent with the Hashin and Rotem formulation [61]. Finally,  $\sigma_{11}$ ,  $\sigma_{22}$  and  $\tau_{12}$  are the components of the effective stress tensor  $\sigma$  implemented to evaluate damage according to the formulation:

$$\sigma = M\sigma_t \quad (4.13)$$

where  $\sigma_t$  corresponds to the true stress and  $M$  stands for the artificial damage operator which is iteratively re-computed once damage has initiated for at least one of the four modes to model damage evolution.  $M$  is computed as:

$$M = \begin{bmatrix} \frac{1}{(1-d_f)} & 0 & 0 \\ 0 & \frac{1}{1-d_m} & 0 \\ 0 & 0 & \frac{1}{1-d_s} \end{bmatrix} \quad (4.14)$$

Variables  $d_f$ ,  $d_m$  and  $d_s$  are used to represent fibers, matrix and shear internal damage. These are derived directly from the damage variables  $d_f^t$ ,  $d_m^t$ ,  $d_f^c$  and  $d_m^c$  as follows:

$$d_f = \begin{cases} d_f^t & \text{if } \sigma_{11} \geq 0 \\ d_f^c & \text{if } \sigma_{11} < 0 \end{cases} \quad (4.15)$$

$$d_m = \begin{cases} d_m^t & \text{if } \sigma_{22} \geq 0 \\ d_m^c & \text{if } \sigma_{22} < 0 \end{cases} \quad (4.16)$$

$$d_s = 1 - (1 - d_f^t)(1 - d_f^c)(1 - d_m^t)(1 - d_m^c) \quad (4.17)$$

Here, the specific damage variable  $d$  for a particular mode is given by the expression:

$$d = \frac{\delta_{eq}^f(\delta_{eq} - \delta_e^0 q)}{\delta_{eq}^f(\delta_{eq}^f - \delta_e^0 q)} \quad (4.18)$$

where  $\delta_{eq}^0$  is the initial equivalent displacement at which the initiation criterion for the specific failure mode is met, and  $\delta_{eq}^f$  is the displacement at which the material is completely failed for the same mode.

This relation is presented in Figure 4.19(a). Once damage is initiated, the material properties are degraded such that the equivalent stress that the laminate can carry follows the trend shown in Figure 4.19(b). This is valid for each one of the four damage mechanisms. The positive slopes prior to damage corresponds to the elastic behavior of the material. The model is only realistic for materials that show elastic-brittle behavior, as no plasticity is involved in the mathematical formulation. The negative slope which follows damage is computed by the evolution of the damage variable of the mode in analysis, according to the equations below:

$$\text{Fiber tension } (\sigma_{11} \geq 0) \begin{cases} \delta_{eq}^{ft} = L^c \sqrt{\langle \epsilon_{11} \rangle^2 + \alpha \epsilon_{12}^2} \\ \sigma_{eq}^{ft} = \frac{\langle \sigma_{11} \rangle \langle \epsilon_{11} \rangle + \alpha \tau_{12} \epsilon_{12}}{\delta_{eq}^{ft} / L^c} \end{cases} \quad (4.19)$$

$$\text{Fiber compression } (\sigma_{11} < 0) \begin{cases} \delta_{eq}^{fc} = L^c \langle -\epsilon_{11} \rangle \\ \sigma_{eq}^{fc} = \frac{\langle -\sigma_{11} \rangle \langle -\epsilon_{11} \rangle}{\delta_{eq}^{fc} / L^c} \end{cases} \quad (4.20)$$

$$\text{Matrix tension } (\sigma_{22} \geq 0) \begin{cases} \delta_{eq}^{mt} = L^c \sqrt{\langle \epsilon_{22} \rangle^2 + f \epsilon_{12}^2} \\ \sigma_{eq}^{mt} = \frac{\langle \sigma_{22} \rangle \langle \epsilon_{22} \rangle + \tau_{12} \epsilon_{12}}{\delta_{eq}^{mt} / L^c} \end{cases} \quad (4.21)$$

$$\text{Matrix compression } (\sigma_{22} < 0) \begin{cases} \delta_{eq}^{mc} = L^c \sqrt{\langle -\epsilon_{22} \rangle^2 + f \epsilon_{12}^2} \\ \sigma_{eq}^{mc} = \frac{\langle -\sigma_{22} \rangle \langle -\epsilon_{22} \rangle + \tau_{12} \epsilon_{12}}{\delta_{eq}^{mc} / L^c} \end{cases} \quad (4.22)$$

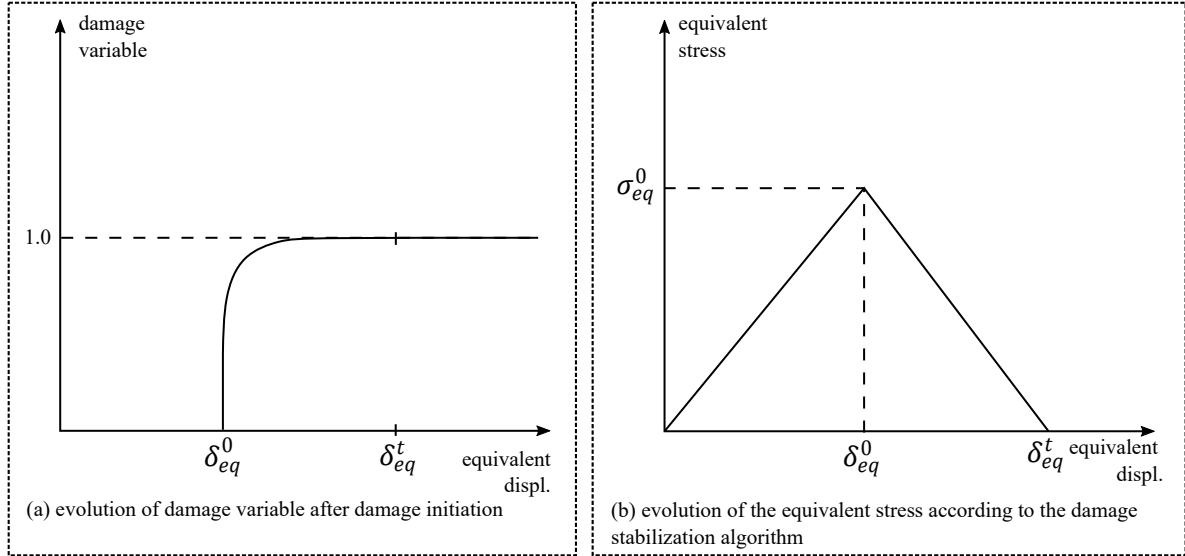


Figure 4.19: Mathematical formulation of Hashin Rotten failure criterion: on the left side, the damage variable as a function of the equivalent displacement. On the right side, the linear relation before and after damage between equivalent stress and equivalent displacement.

In these expression,  $L^c$  is the characteristic element length. This corresponds to the entire element side length due to the linear formulation applied to continuum shell elements.  $L^c$  is calculated as the square root of the element planar surface. The symbol  $\langle \cdot \rangle$  denotes the Macaulay operator which attributes for any  $n \in \mathbb{R}$  the following expression:

$$\langle n \rangle = \frac{(n + |n|)}{2}$$

#### 4.3.2. Implementation of Damage Propagation in Abaqus

In order to successfully implement damage progression in the simulation, a series of additional material properties must be assigned to the model. These describe the energy released due to fracture in the different failure modes. As this is not easily attainable from the material provider, the required information is retrieved from the study performed by Abir et al. [62]. The authors develop a model to simulate the progressive effects of damage as it propagates through a flat laminate after impact. This study has been chosen over others as the material utilized is a general T700-epoxy resin CFRP composite, similar to the one used at cellcentric GmbH for all experimental sets. The material properties presented in Table 4.5 are therefore selected.

Table 4.5: Overview of fracture energy properties used to simulate damage propagation through the material, from [62]

Longitudinal tensile fracture energy [N/mm]	Longitudinal compressive fracture energy [N/mm]	Transverse tensile fracture energy [N/mm]	Transverse compressive fracture energy [N/mm]
133	40	0.5	1.6

In Abaqus/Standard, an element is deleted once the damage variable for all failure mode reaches a pre-selected value  $d_{max}$ . By default, this is set to 1.0, but can be adjusted according to the user input. When lower than 1.0, the removal of the ineffective element is forced earlier. When higher, the element is allowed to degrade further, and remain in the model even after complete failure. If the Abaqus default parameter is not adjusted, when the elements are removed from the model their nodes still remain in the geometry even though effectively they are not attached to any element. However, if the internal pressure loading is applied directly on these nodes, the model fails to converge.

To prevent this effect, it is decided to maintain 1.0 as maximum damage variable  $d_{max}$ , but to hinder element removal. This function forces each element to remain in the model even after failure. This way, once all damage variables  $d$  reach the maximum value for each failure mode, the stiffness matrix of the element remains constant, as opposed to being removed from the model all at once. In other words, the material

degradation stops and the affected nodes remain attached to a physical element.

This strategy also offers a solution to a second issue encountered in the implementation of the damage progression analysis. As the solution progresses, the nodes of the failed elements which are removed from the model after damage may undergo nonphysical displacements due to the extrapolation scheme implemented in Abaqus/Standard. Avoiding element removal partly allows to prevent this issue. Further tuning of the elements stiffness is also possible to inhibit unrealistic element deformations.

# 5

## Results and Assessment of Model Performance

Once the geometry and material composition of the CPV are adjusted, an internal pressure loading of 105 MPa is applied on the inner walls of the vessel and on the boss. This pressure level corresponds to the required operational pressure of 70 MPa multiplied by a margin of 1.5, and it is widely applied for simulation purposes at cellcentric GmbH.

The ultimate objective is to predict with high level of accuracy the deformational behavior and the burst pressure of the different vessel configurations. With this purpose, strains, stresses and failure data at 105 MPa internal pressure is extracted from the model and post-processed in Python. Here, the results are compared to the experimental data. Correlation is then evaluated in terms of four main parameters:

- **Outer strains** - these are a measurement of the deformation of the vessel during pressurization. Experimental results are measured during testing by means of DIC, and then decoupled into tangential and meridional strains by means of rotational transformations. Similarly, outer strains are obtained from Abaqus in the global coordinate system, and then rotated appropriately in the tangential and meridional directions.
- **Per-ply stresses** - these are exported directly from Abaqus in the ply-specific coordinate system. Three components are retrieved for each ply: S1 stresses define the stresses in the fiber's longitudinal direction, S2 stresses the transverse stresses, and S12 stresses the shear stresses. Stresses are not measured directly from experiments. However, they are used directly for the prediction of the burst pressure, and can therefore be linked to the next parameter in this list.
- **Burst pressure** - this is easily retrieved from testing, as it corresponds to the pressure level at which the vessel fails and the measured pressurization level drops. The predicted burst pressure is not extracted directly from Abaqus, but it is calculated from the stress-state at the highest simulated pressure stage. Details regarding the burst pressure calculation are presented in Section 5.1.2.
- **Burst location** - the location of failure is highly dependent on the vessel layout and stacking sequence. In laboratory settings, assessing where the vessel fails is arguably simple. Although after burst the vessel is reduced to powder, usually remainders of specific parts of the structure provide insights on the location of failure. An overview on the burst location for the BL, BC and W2B configurations is provided in Figure 5.1. Predicting the failure location numerically, on the other hand, poses some challenges. Similarly to the burst pressure, the location of failure is estimated from the stress-state at 105 MPa internal pressure. Cylinder failure is in general easier to predict, as in this region the loading on the structure is uniform, the geometry rather simple and the material composition predictable. Dome burst, on the other hand, is tedious to simulate due to the doubly-curved geometry and the heterogeneous material composition of the laminate.

Finally, the computational time of the simulation is evaluated and compared to that of previous simulation tools to assess its efficiency.

## 5.1. Performance of the Solid Model

The numerical approaches presented in Chapter 3 and the physical adjustments to the model explained in Chapter 4 lead to a significant improvement of the state-of-the-art simulation tools for the prediction of the deformational behavior of CPVs. As the solid model is built directly on the inheritance of the one developed by Johman [32], a direct comparison can be made in terms of accuracy in the depiction of deformations, prediction of stresses, estimation of burst, and computational time. This comparison allows to address the relevance of all adjustment strategies one by one.

Once the advantages of the developed solid model over its predecessor are assessed, its predictive ability is tested on different vessel configurations to study its robustness. Specifically, vessels which experience different failure types are investigated with a twofold purpose: first, to check to which extent the solid model is able to predict the deformational behavior of the tank according to its layup; second, to observe whether patterns can be found to estimate the burst pressure and location of different vessel configurations.

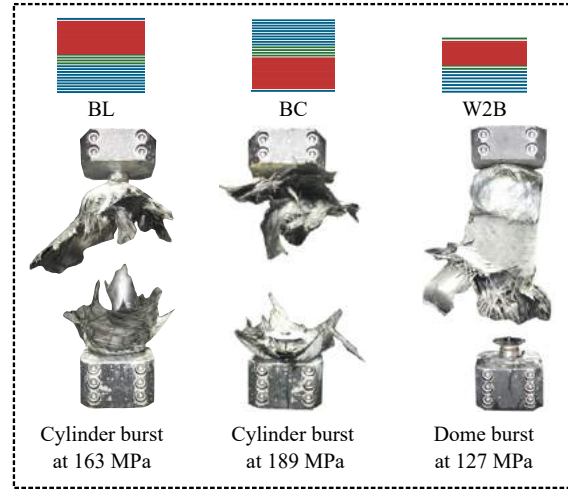


Figure 5.1: Overview of burst pressure and location for the BL, BC and W2B vessel configurations.

### 5.1.1. Prediction of Deformational Behavior

The performance of the solid element model is initially tested on the deformational behavior of the vessel during pressurization. In this section, the results for the three vessels configurations listed in Chapter 3 are presented. Outer strains in the tangential and meridional directions are computed by means of geometrical rotations from the longitudinal, transverse and shear strains extracted from Abaqus.

These are presented in Figure 5.2, which shows the computed tangential and meridional strains as compared to the pre-existing simulation benchmark for the BL, BC and W2B vessel configurations. All strain curves are also compared to the experimental results. An overview of the discrepancies between the modelling strategies and the average experimental data is presented in Table 5.1.

Table 5.1: Overview of cylinder strains at 105 MPa and respective discrepancy with experimental data.

		Outer tangential strains in cylinder (at 105 MPa)		Outer meridional strains in cylinder (at 105 MPa)	
		Absolute strain [%]	Discrepancy wrt experiment [%]	Absolute strain [%]	Discrepancy wrt experiment [%]
BL	Benchmark	1.08	13.6	0.45	28.6
	Solid model	0.89	6.3	0.40	23.7
BC	Benchmark	1.01	20.2	0.40	27.3
	Solid model	0.80	4.8	0.46	16.3
W2B	Benchmark	1.52	16.9	0.68	20.0
	Solid model	1.23	5.3	0.69	18.8

For all three cases, the solid model is noticeably more accurate than the existing benchmark in the depiction of outer tangential strains in the cylindrical region of the vessel. Here, the adjustment of material properties leads to the most drastic increase in laminate stiffness, due to the presence of the highly compacting circumferential plies. Although both the pre-existing benchmark and the new solid model include a thickness approximation based on Kang's definition of compaction [31], the benchmark does not include an adjustment of material properties. This translates in an underestimation of the laminate stiffness, which can be compared to an effective removal of load-carrying material. In fact, the thickness of each ply is reduced but the associated material properties are not adjusted. The adjustment of material properties proposed in Chapter 4 mitigates this heavy assumption, and it constitutes the most relevant difference between the two modelling approaches. The increase in laminate stiffness translates into a substantial decrease of tangential strains, which now approach the experimental data much more closely for all three configurations. The effect

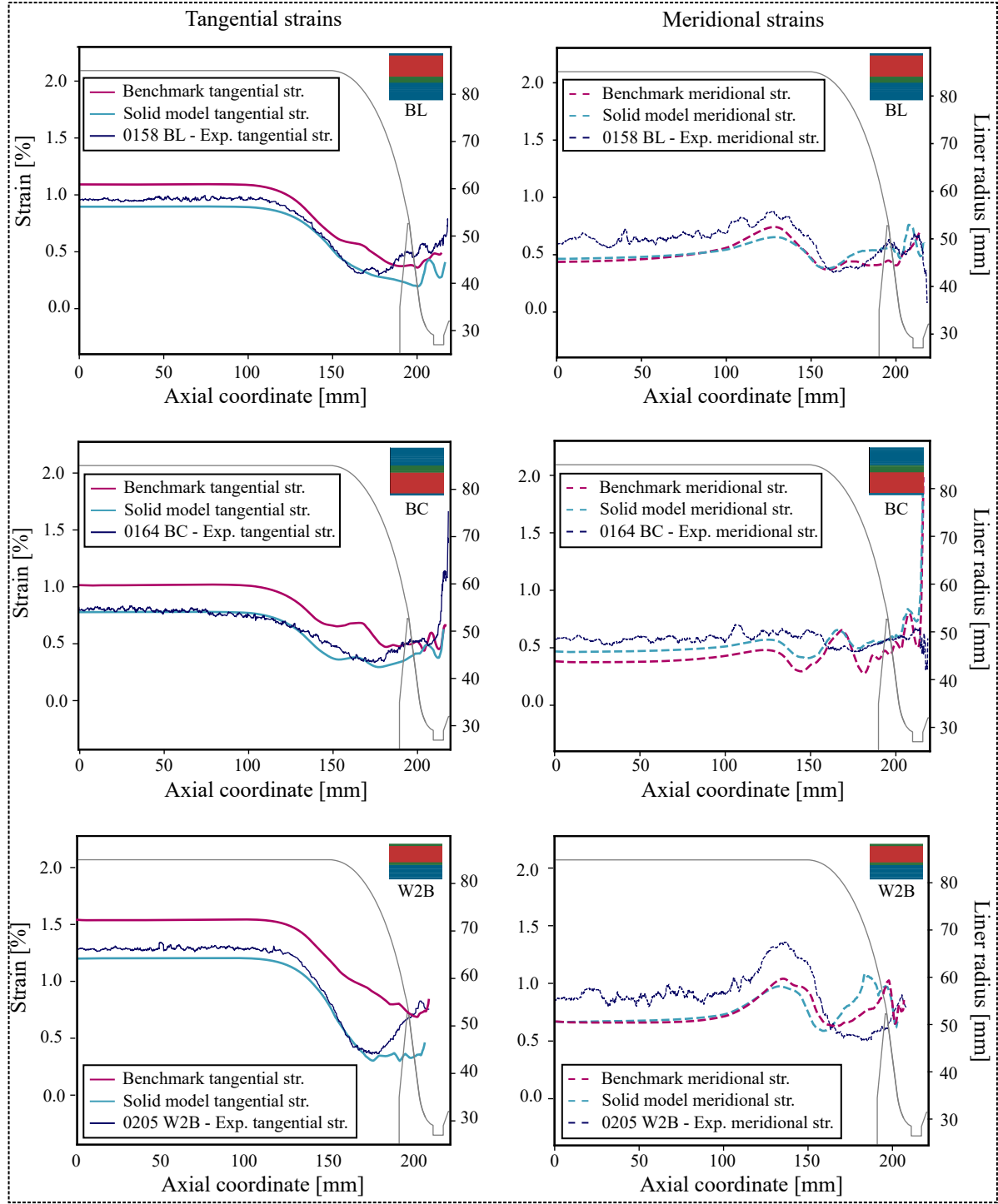


Figure 5.2: Overview of tangential and meridional strains for the BL, BC and W2B configurations as extracted from the solid model results in comparison to the previous benchmark simulation and to the experimental data. All results are extracted at 105MPa.

is more relevant in the BL and W2B configurations. In these cases, the placement of the highly-compacting circumferential plies on the outside of the laminate results in better compaction and a more significant decrease in thickness. In turn, the stiffness properties are enhanced to a greater extent.

In the dome region, the effect is less drastic. Here, the laminate is not as compacted due to the absence of circumferential plies. Furthermore, the extent of the thickness reduction of the laminate is directly related to the normal component of the fiber tension load, computed as shown in Equation 4.1. In the dome re-

gion, the mandrel can only be reinforced by low angle helical plies as the high orientation of circumferential plies may easily lead to slippage. The low angle of orientation of the local reinforcement, according to Equation 4.1, leads to a low normal load on the laminate, which therefore translates into a limited compaction. The combination of these two effects leads to a less-noticeable increase of material properties.

The difference in meridional strains between the previous benchmark and the developed solid model is less significant. Meridional strains are mainly controlled by the axial reinforcement provided by low angle helical plies. As shown in Figure 4.14, the increase in material properties for low angle helical plies is only marginal compared to circumferential plies, which explains why the meridional strains remain approximately unchanged. An exception is the BC case, for which the meridional strain curves differ significantly. The reason of this phenomenon is found in the mutual interaction between tangential and meridional stresses triggered by the drastic decrease in tangential strains.

In the dome region, a slight improvement of the numerical stability of the response is to be attributed to the smoother vessel contour. This is represented more realistically by the new solid model, which takes into consideration the thickness accumulation due to dwelling at the turnaround point of high angle helical plies. This is particularly appreciable for the BC case.

Despite the improvement, some differences between simulation and experimental results are still noticeable in both outer tangential and meridional strains. A plausible reason of these discrepancies is that the solid model does take into account the development of damage through the material in any way. In other words, the material properties do not experience any degradation, and remain constant after every load increment. This is a limitation as effectively, when the laminate takes on the increasing pressure load, the composite is damaged. This compromises its quality, resulting in a degradation of both the matrix and the fiber components. The load-carrying capabilities of the structure are therefore expected to decrease. As proved by the research of Soriano [55], this has a significant impact on the behavior of the outer strain curve. Each layup seems however to be affected by this phenomenon to a different extent.

As the pressure loading is transferred through the material from the innermost- to the outermost-ply, stresses develop through the thickness of the laminate, varying according to the through-thickness location of the ply. The per-ply stresses computed numerically are shown for every vessel configuration in Figure 5.3. For all cases, the most critical stress-state is caused by the high tangential stresses which develop in the cylinder. These are mainly carried by the circumferential plies, in which the fiber component is almost perfectly aligned to the stress direction, i.e. perpendicular to the longitudinal axis of the vessel. The stress gradient of tangential stresses is such that inner plies experience the highest loading, which then decreases towards the outermost ply. In this sense, the innermost circumferential ply is responsible for withstanding the highest tangential stresses.

The effect of damage is expected to be particularly relevant for the BL and the W2B configurations, where the stack of circumferential plies is located on the outside of the laminate. For these vessels, the high tangential stresses are transferred through the entire stack of low angle helical plies before they finally encounter a ply-type suitable to withstand them. In this process, the inner helical plies are heavily loaded, and damage is likely to degrade their load-carrying potential. For this reason, it is acceptable that the outer strains predicted for the BL and the W2B configurations show a more relevant deviation with respect to the experimental curve.

For the BC configuration, on the other hand, the stack of circumferential plies is located on the inside of the laminate, therefore allowing the circumferential plies to take on the high tangential stresses where they are highest. This way, only a limited portion of tangential loading reaches the outer helical plies. In turn, these helical plies are expected to experience less damage. The neglect of material degradation due to damage is therefore less relevant for the BC case. In other words, it is reasonable that the simulated tangential deformation in the cylinder is closer to the experimental results for the BC vessel configuration rather than the BL and W2B. Effectively, including damage analysis in the investigation of the BC laminate would only marginally change the outcome, as the BC laminate is less prone to material degradation.

### 5.1.2. Considerations on Stresses and Estimation of Burst

The stress-state of the laminate at 105 MPa internal pressure presented in Figure 5.3 is used to predict the pressure level at which burst will occur.

For all vessel configurations, the highest stresses are found in the stack of circumferential plies in the fiber direction (S1). These stresses derive from the radial loading imposed on the structure, which translates in high tangential stresses in the laminate. The tangential stresses are promptly carried by the circumferential plies, for which the fiber component is conveniently aligned to almost perpendicularly to the longitudinal axis of the vessel. As these are highest on the inside of the laminate, the innermost ply in the stack of circumferentials



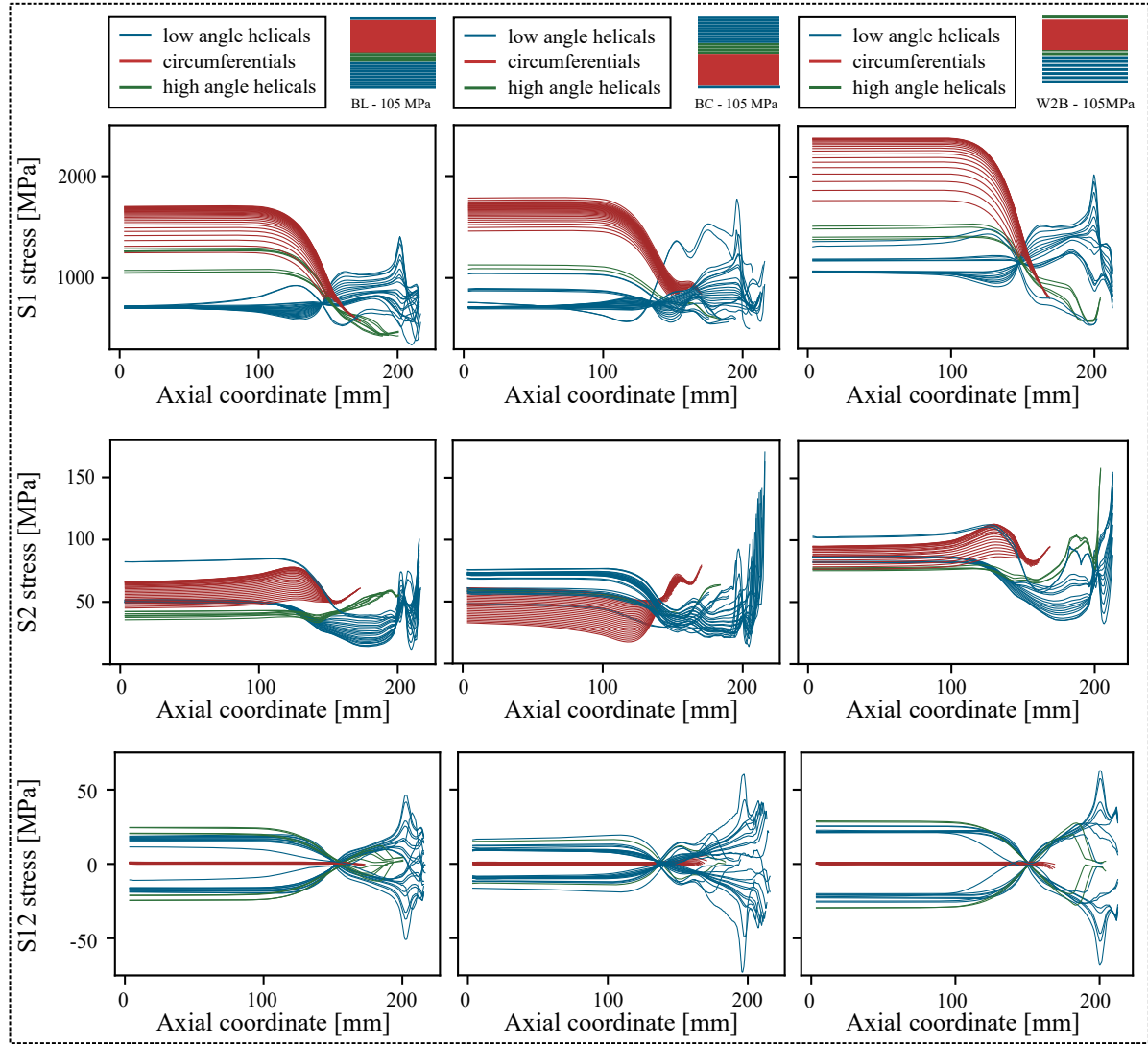


Figure 5.3: Overview of S1, S2 and S12 stresses for the BL, BC and W2B configurations respectively.

is the most heavily loaded. The S1 stresses then decrease towards the outside, reaching the lowest magnitude in the outermost ply. The stress gradient depends on three main aspects:

1. The through-thickness position of each specific ply.
2. The material properties of each specific ply.
3. The orientation of each specific ply.

For previous modelling techniques which did not involve any adjustment of material properties, the strength and stiffness of each ply were kept constant. This means that the stress gradient through the stack of circumferential plies was only dictated by the through-thickness location of each specific ply and its orientation. This resulted in a limited differentiation of stresses through the ply-group. Graphically, this means that the cylinder stresses of the innermost and outermost circumferential plies were closer to each other. The effect is less drastic for helical plies as, once again, the material properties are only barely increased by compaction. This is conveniently shown in Figure 5.4, where a comparison between S1, S2 and S12 stresses for the non-compacted and the compacted laminate is presented for the BL configuration. A similar behavior is experienced by the BC and W2B vessel types.

A second effect of the adjustment of material properties on the stress-state of the laminate is the magnitude of the highest S1 stress. Figure 5.4 shows that, as the stiffness of each ply increases, the maximum stress

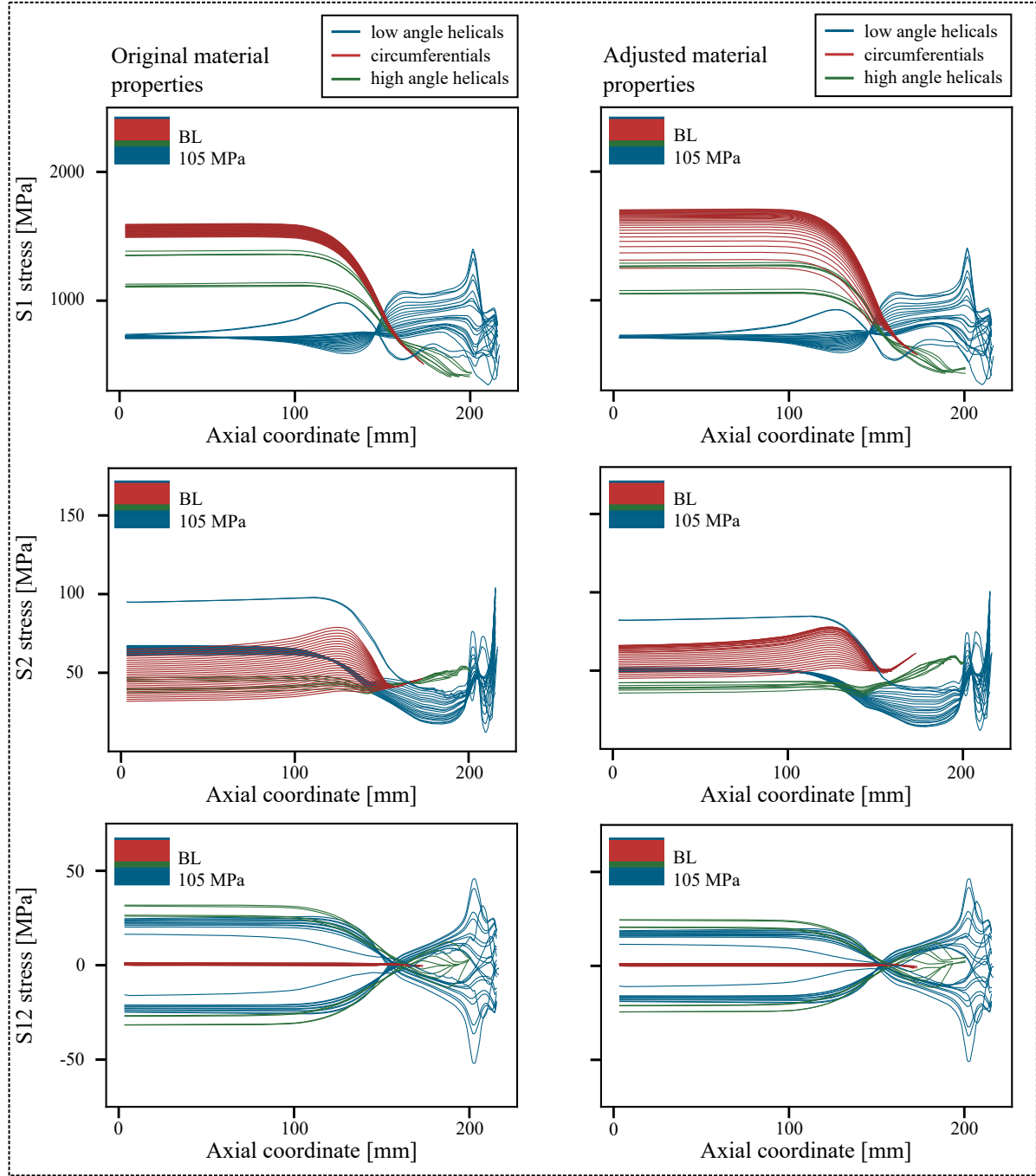


Figure 5.4: Comparison of S1 stresses for the BL vessel configuration with and without heterogeneous material properties, at 105MPa.

that it can carry also increases. In this sense, higher material properties attract higher stresses, eventually leading to a better vessel performance.

The opposite effect is found for S2 stresses, where the stress gradient through the stack of circumferential plies decreases. The effect is reasoned by the required balance of shear stresses: as the fiber component is now able to carry significantly higher stresses, the matrix is less heavily loaded. This effect is less noticeable in the stack of helical plies where the material properties are similar for all layers.

As circumferential plies are loaded in the tangential direction aligned to their fiber direction, the S12 shear stresses are close to null in this ply-group. In fact, S12 stresses are mainly carried by helical plies. Shear stresses are symmetric as the winding of helical plies leads to an even interwoven  $[\pm\alpha]$  laminate. S12 stresses are not significantly affected by the adjustment of material properties, as it was mentioned that helical plies

are only marginally affected. As for the matrix-dominated S2 stresses, the slight decrease in their magnitude recorded for the solid model is mainly due to the fact that now the fiber component is more efficient in carrying longitudinal stresses, decreasing the loading on the matrix.

From the combination of stresses at 105MPa, different methods can be used to estimate the burst pressure. In this context, burst is estimated in terms of first ply failure, meaning that the entire laminate is assumed to fail once one of its plies is damaged. This approximation has some limitations. In reality, as one ply fails, the stresses are re-distributed such that the surrounding plies are temporarily able to carry them. Eventually, this leads to a faster degradation of these surrounding plies, which will themselves fail subsequently until the last ply has finally collapsed. The effect is especially true when failure is associated to compression or shear. When tensile failure is experienced on a UD laminate, on the other hand, all plies are similarly loaded and laminate failure is expected to occur right after first ply failure. Therefore, the stack of circumferential plies is expected to fail almost simultaneously. Load re-distribution will only occur for a very short time, until all plies fail due to the high tangential stresses.

Several criteria can be used to evaluate whether a ply has failed, which describe in more or less detail the failure modes that the laminate can experience. In this research, Puck failure criterion is implemented, which theoretically estimates failure based on four failure modes. These are respectively fiber failure, and inter-fiber failure in mode A (transverse tension), mode B (shear) or mode C (transverse compression). In this study, only the most relevant loading case is considered, i.e. fiber tensile failure.

According to Puck failure criterion, a specific ply experiences fiber tensile failure when the following is valid:

$$F_{FF} = \frac{1}{S^t} \left[ \sigma_1 - \left( \nu_{12} - \nu_{12} m_{\sigma,f} \frac{E_{11}}{E_{11,f}} \right) (\sigma_{22} + \sigma_{12}) \right] \geq 1 \quad (5.1)$$

Here,  $S^t$  is the tensional strength of the fibers. In general, the expression is also valid for compressive fiber failure, meaning that  $S^t$  can potentially be substituted by the compressive strength of the material  $S^c$ . However, the fiber constituent of CPVs is not expected to experience compression, thus only tensile failure is considered.  $\sigma_i$  represent the components of the stress tensor,  $\nu_i$  are the components of the Poisson's ratio in the respective directions, and  $m_{\sigma,f}$  is a material specific factor, often set to 1.3 for CFRP. According to Equation 5.1, the ply fails when its failure factor reaches 1.

To estimate burst, the failure factor  $F_{FF}$  is calculated from the stress-state obtained from simulation at 105 MPa for each ply and at every axial location along the vessel length. The failure envelope is then plotted to observe which areas of the vessel are most critical, and where fiber failure is expected to occur first. The maximum failure index is then extrapolated from the failure envelope, and the respective burst pressure is computed linearly as follows:

$$\text{burst pressure} = \frac{105 \text{ MPa}}{F_{FF,max}} \quad (5.2)$$

The failure envelopes at 105 MPa for the BL, BC and W2B cases are shown in Figure 5.5, alongside the predicted burst computed by means of Equation 5.2. Here, the dotted line represents the failure index at 105 MPa which would lead to failure at the pressure stage at which burst was recorded experimentally. Again, this failure index is computed linearly from Equation 5.2. For convenience, an overview of the burst prediction for each vessel configuration is provided in Table 5.3.

The maximum failure index presented in Figure 5.5 for the BL configuration is rather different than the experimental result. Linear extrapolation leads to a predicted burst pressure of 196 MPa, whereas burst is recorded at 163 MPa during experiment. Similarly as for the strain prediction, this is partly attributable to the neglect of damage in the simulation strategy. This is significant especially for the BL and W2B configurations, where the stack of circumferential plies is located on the outside of the laminate. During pressurization, damage develops through the structure, reducing the load-carrying capabilities of the material and leading to an earlier burst event. In this sense, final failure in reality is expected to occur at lower pressure stages than the simulation may predict.

For the BC case, this effect is less relevant. Here, the stack of circumferential plies is located on the inside of the laminate, preventing the helical plies from being heavily loaded and from experiencing relevant damage. In this case, the circumferentials are fully able to carry the tangential stresses before these reach the outer helical plies, which therefore remain undamaged until high pressure stages. For this reason, neglecting the effects of material degradation does not have a significant impact on the burst estimation of the BC vessel type. However, it should be noticed that according to the failure envelope plotted for the BC configuration in

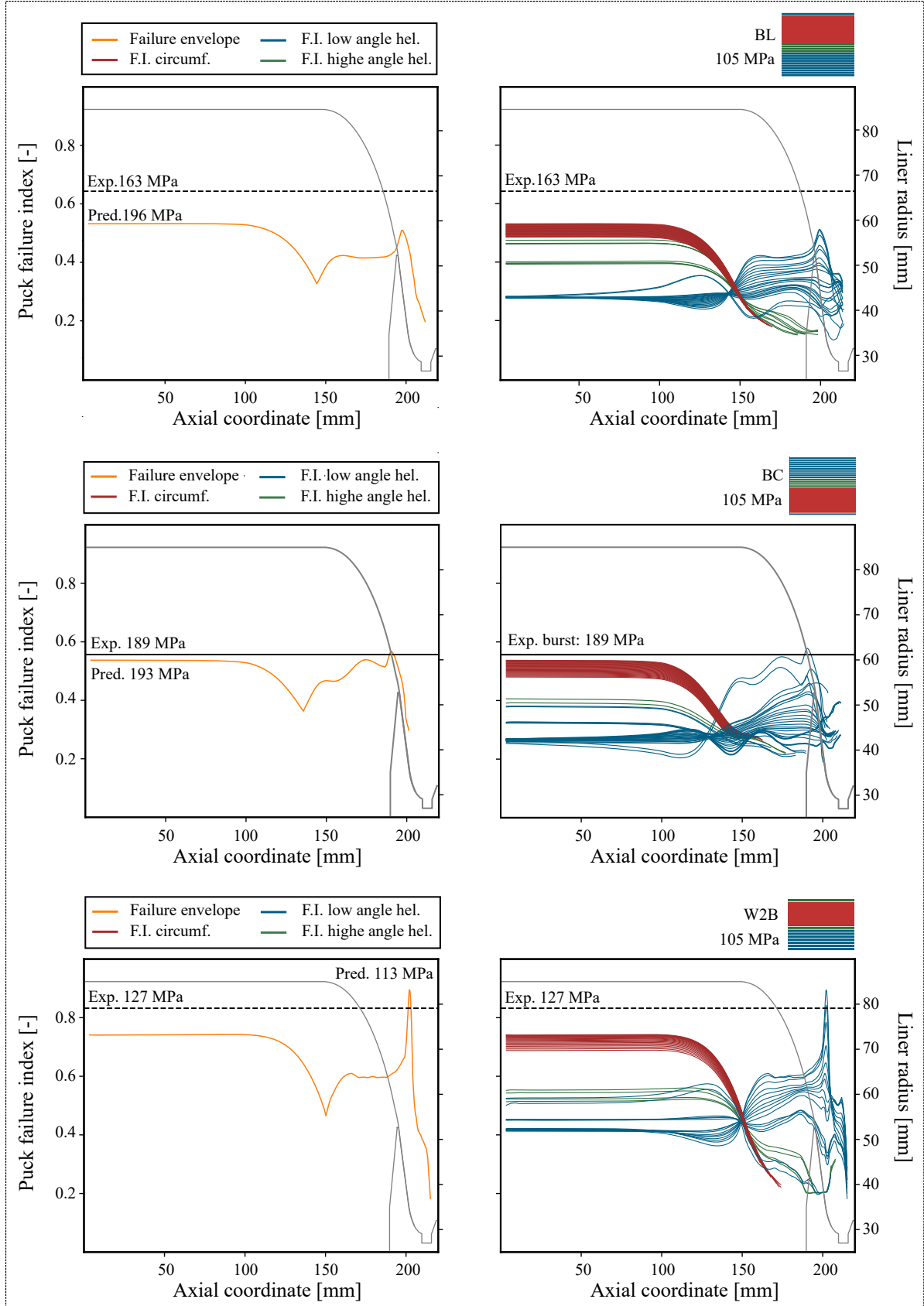


Figure 5.5: Overview of the failure envelope for the BL, BC and W2B configurations according to Puck failure criterion, for the stress-state at 105MPa computed by means of the developed solid model

Figure 5.5, first failure seems to happen in the dome region, where in fact the highest failure index is found in the innermost low angle helical ply. When looking at the per-ply failure indices on the right hand side of the figure, however, one can see that this peak is reached only by a single helical ply. This suggests that failure can be attributed to a local damage which would not lead to burst. In reality, when one ply fails, the stresses are temporarily re-distributed amongst the surrounding plies, until these reach failure as well. Figure 5.5 shows that the stack of outer helical plies experience low failure indices, meaning that they would be able to compensate for the damaged innermost ply and delay dome failure. On the other hand, the high failure index reached in the cylinder is approached by all circumferential plies, suggesting that all plies fail subsequently right after first ply failure. Therefore, the prediction of burst pressure for the BC configuration is computed in the cylinder.

The W2B vessel configuration behaves similarly to the BL layup in the cylinder. Here, the prediction of failure is influenced by the neglect of damage. The high tangential stresses caused by the radial loading are expected to cause fiber fracture in the inner helical plies. For this reason, the burst pressure is overestimated in the cylinder. However, a peak in fiber fracture index is found in the dome, matching the dome burst experienced during testing. Contrarily to the BC case, in the W2B configuration the high peak in the dome is not approached only by a single ply, but rather by the entire stack of inner helical plies. This suggests that failure would not be localized to a single layer, but rather diffused. In turn, load re-distribution after first ply failure would not be sufficient to withstand the high local stresses, eventually leading to burst. For this reason, the dome failure predicted by the solid model seems to be realistic, partly proving the predictive ability of the modelling strategy.

In general, the solid model is able to give a reasonable estimation of outer tangential and meridional strains, and to provide a reliable indication on the failure location. In fact, for all the considered configurations failure is predicted in the location where it was actually recorded during testing. The BL and BC vessels are expected to fail in the cylinder, whereas dome failure is expected to cause final burst for the W2B case. Despite its potential, the solid model is not yet able to estimate the final burst pressure accurately for all vessel types. In this context, the continuum shell model is expected to provide further insights. Damage progression analysis is implemented in its solution, partly mitigating the limitations of the solid model. On the other hand, a few differences exist in the numerical formulation of the two modelling strategies, which eventually lead to some fundamental differences. In the next section, these differences are firstly analyzed in detail, with the purpose to familiarize with the effects of the assumptions that the two modelling strategies rely on. Once these foundations are established, the advantages of considering degradation due to damage in the analysis are studied.

## 5.2. Performance of the Continuum Shell Model

The continuum shell model allows for a relatively simple implementation of the Hashin Rotem failure criterion to account for damage progression through the material. The material properties of each element are degraded iteratively as the failure initiation factor defined in Section 4.3.1 is reached. Before studying the results of such implementation, it is important to give a close look to the results of the constitutively elastic analysis and underline all existing differences between the continuum shell model and the solid model. This way a robust foundation of knowledge is built to understand whether the inclusion of such damage progression analysis gives any advantage to the existing simulation strategy.

### 5.2.1. Prediction of Deformational Behavior

The evaluation of the model performance, once again, begins with the assessment of outer strains. These are presented for the BL, BC and W2B cases in Figure 5.6. Here, the results of the solid model are displayed in light blue, whereas the results of the continuum shell model are presented in green. Finally, in pink are the results of the continuum shell model when the damage propagation is implemented in the solution. An overview is also presented in Table 5.2.

Firstly, the constitutively elastic responses of the solid model and of the continuum shell model are compared. For all vessel configurations, outer meridional strains are slightly higher for the continuum shell formulation. The reason of this trend can be explained by the different element types. The radial loading caused by pressurization creates compressive radial stresses in the matrix component of the laminate which, in turn, experiences compressive through-thickness strains. Due to the Poisson's effect, the radial compressive stresses squeeze the matrix component in the transverse in-plane direction, therefore increasing the in-plane transverse strains. In turn, this leads to an alleviation of stresses and strains in the longitudinal

fiber direction. The solid element formulation is fully able to capture the compressive radial stresses through the laminate thickness thanks to several integration points placed across the thickness of each element. On the other hand, continuum shell elements cannot account for this normal stress component, therefore not including the contribution of radial compressive stresses to the in-plane loading state. For this reason, the constitutively elastic strain responses of the two models show some discrepancies.

For tangential strains, the behavior is slightly different. Tangential strains are mainly dominated by the load-carrying action of circumferential plies. For the BL and BC cases, the ratio between the amount of circumferential plies and the amount of helical plies is rather high, meaning that the effect of compressive radial loading on the matrix in helical plies is only marginal. For this reason, the tangential strains are very similar for the solid and the continuum shell model. For the W2B case, on the other hand, the ratio between circumferential and helical plies decreases, meaning that the influence of matrix compression and the relative transverse stress associated to it has a more significant impact on the determination of tangential strains. For this reason, it is observed in Figure 5.6 that the tangential strains obtained from the solid model do not match the ones obtained from the continuum shell model.

Table 5.2: Overview of outer cylinder strains for the BL, BC and W2B vessel configurations, computed by means of the solid model (without damage) and the continuum shell model (with and without damage).

		Outer tangential strains in cylinder (at 105 MPa)		Outer meridional strains in cylinder (at 105 MPa)	
		Absolute strain [%]	Discrepancy wrt experiment [%]	Absolute strain [%]	Discrepancy wrt experiment [%]
BL	Solid (w/o damage)	0.89	6.3	0.48	23.7
	Continuum shell (w/o damage)	0.89	6.3	0.50	20.6
	Continuum shell (w/ damage)	0.93	2.1	0.58	7.9
BC	Solid (w/o damage)	0.80	4.8	0.46	16.3
	Continuum shell (w/o damage)	0.82	2.4	0.48	12.7
	Continuum shell (w/ damage)	0.85	1.2	0.51	7.2
W2B	Solid (w/o damage)	1.23	5.3	0.71	16.2
	Continuum shell (w/o damage)	1.17	10.0	0.73	14.1
	Continuum shell (w/ damage)	1.20	7.7	0.80	4.7

When material degradation is taken into account, the results improve significantly. This holds for all configurations, although it is more relevant for the BL vessel. The outer strains in this case match the experimental results extremely closely. In the cylindrical region of the vessel, both outer tangential and meridional strains increase, leading to a discrepancy with respect to the experimental data of 2.1% and 7.9% respectively. This improvement is caused by the decrease in stiffness experience by the damaged elements, which leads to an overall increase in strains. A similar effect is visible for the W2B case, for which the discrepancy of meridional strains with the experimental data decreases to 4.7%. The improvement is less drastic for tangential strains, where the discrepancy with the experimental data is 7.7% due to the neglect of radial compressive stresses, particularly relevant for the W2B vessel. In the case of BC, tangential strains show almost full accordance with the experimental data, as the discrepancy is now limited to 1.2%. Meridional strains also correlate rather closely, limiting the discrepancy to 7.2%. It is important to notice that, as expected, the impact of damage on the results is less significant for the BC case than for the BL case. Again, this is reasoned by the location of the stack of circumferential plies with respect to the helical plies.

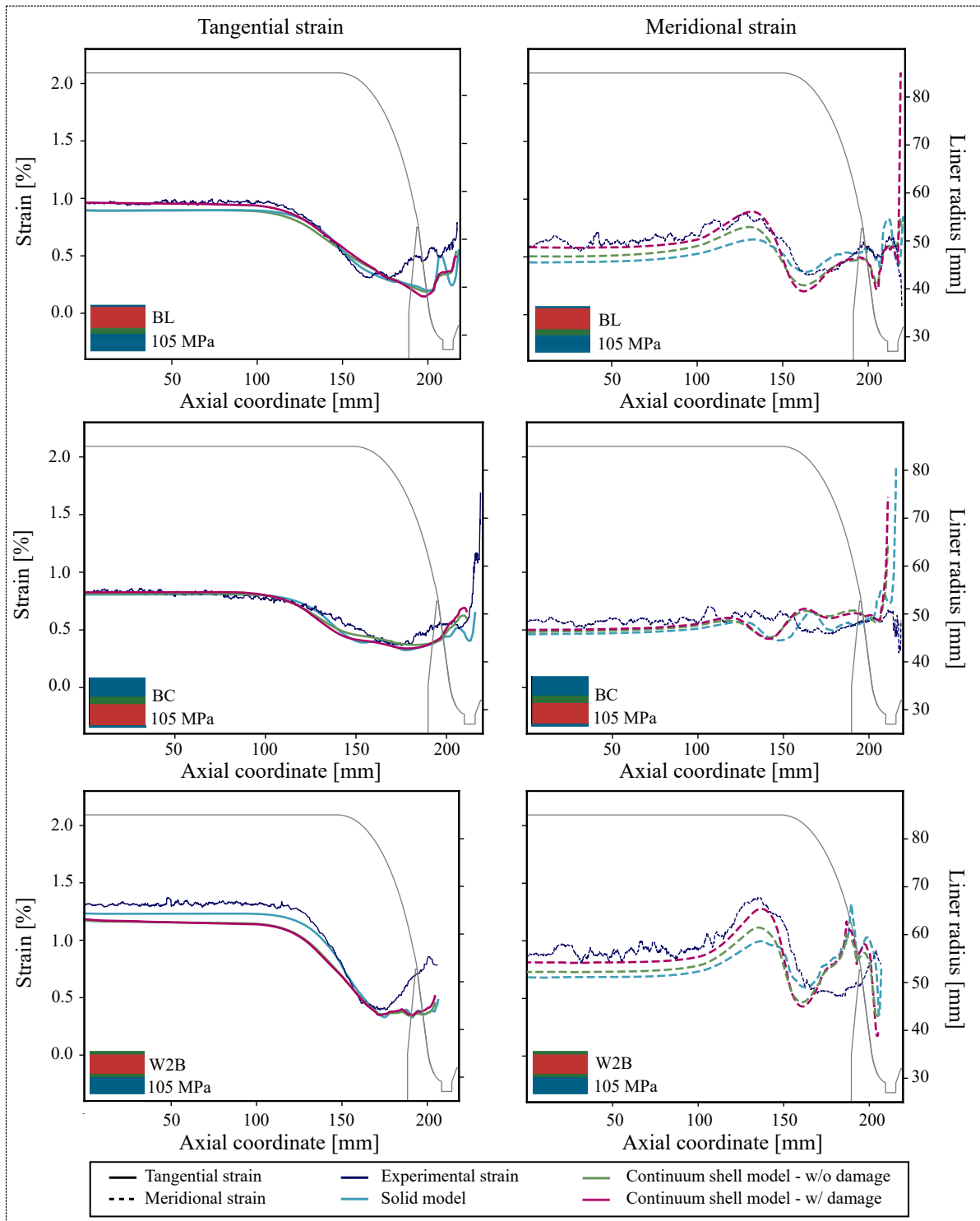


Figure 5.6: Overview of outer tangential and meridional strains at 105MPa for the BL, BC and W2B configurations, as computed by the solid model (without damage) and the continuum shell model (with and without damage).

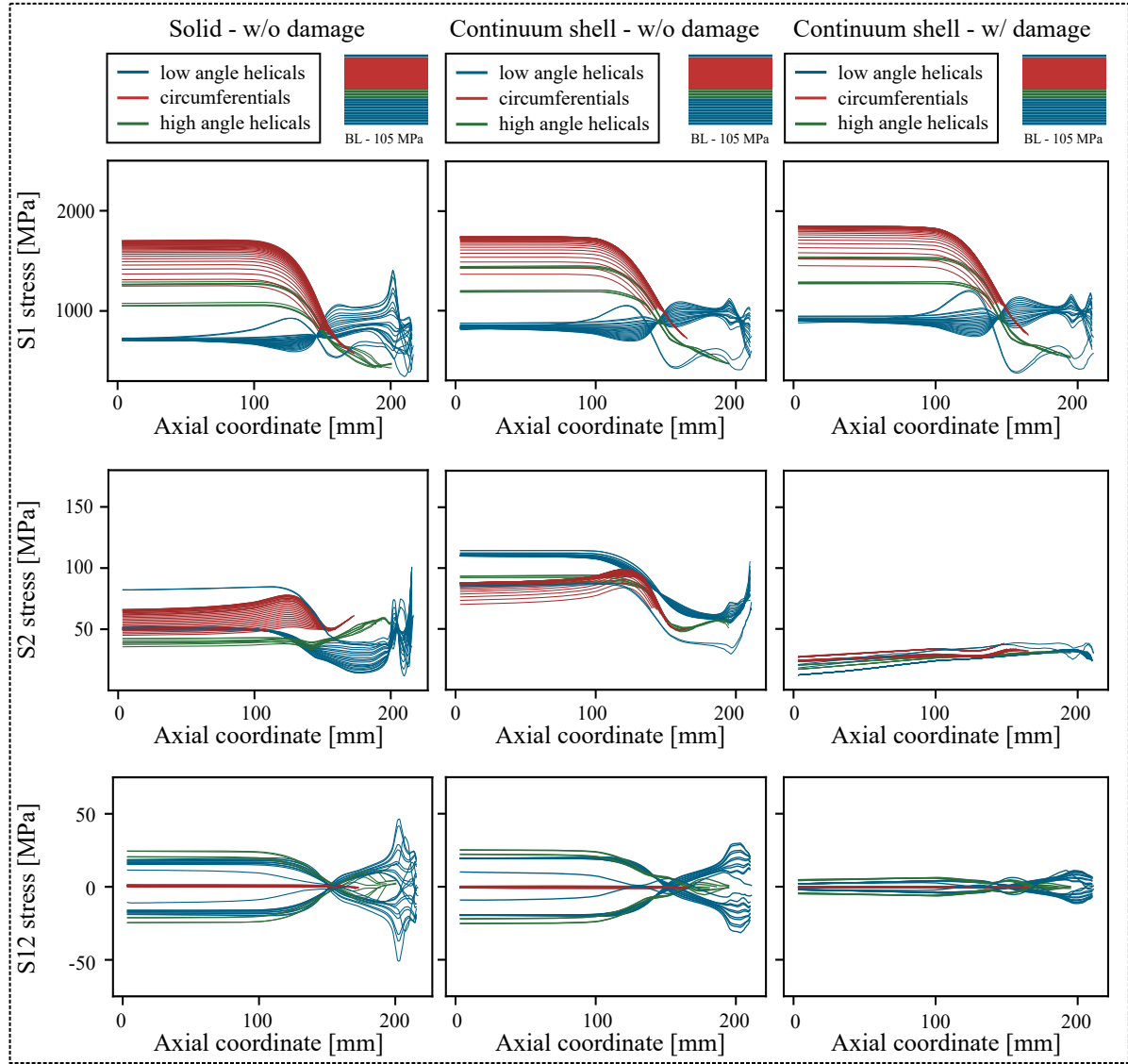


Figure 5.7: Comparison of S1, S2 and S3 per-ply stresses for the BL configuration as computed by the solid model (without damage) and the continuum shell model (without and with damage)

### 5.2.2. Considerations on Stresses and Estimation of Burst

A similar comparison is done in terms of stresses, presented in Figure 5.7 for the BL vessel configuration, in Figure 5.7 for the BC, and in Figure 5.9 for the W2B. All vessel configurations show similar trends.

Again, the differences between the constitutively elastic response of the solid model and of the continuum shell model are tackled first. S1 longitudinal stresses are slightly higher for the continuum shell model, both in circumferential and in helical plies. Furthermore, the stress gradient through the stack of circumferential plies is reduced, meaning that the innermost and outermost circumferential plies experience a more similar stress-state in the continuum shell model. This is attributed to impossibility to capture the compressive radial stress component with continuum shell elements, which also affects the in-plane stress levels. The compressive radial stresses are location-dependent and affect the stress-state of each ply differently: on the inside, the radial compressive stress matches the internal pressure; on the outside, they equal zero. For this reason, a larger spread in tangential stresses in the innermost and outermost S1 stresses exists for the solid model, where the ply-dependent effect of radial compression is taken into account. For the continuum shell model, on the other hand, the spread is less significant as no difference in radial stresses exists between the inner and outer plies, as these are actually null. A similar consideration is valid for the helical plies, although here the impact is less relevant as the material properties of low angle helical properties are close-to-constant, already causing the spread of stresses between inner and outer plies to be only marginal.



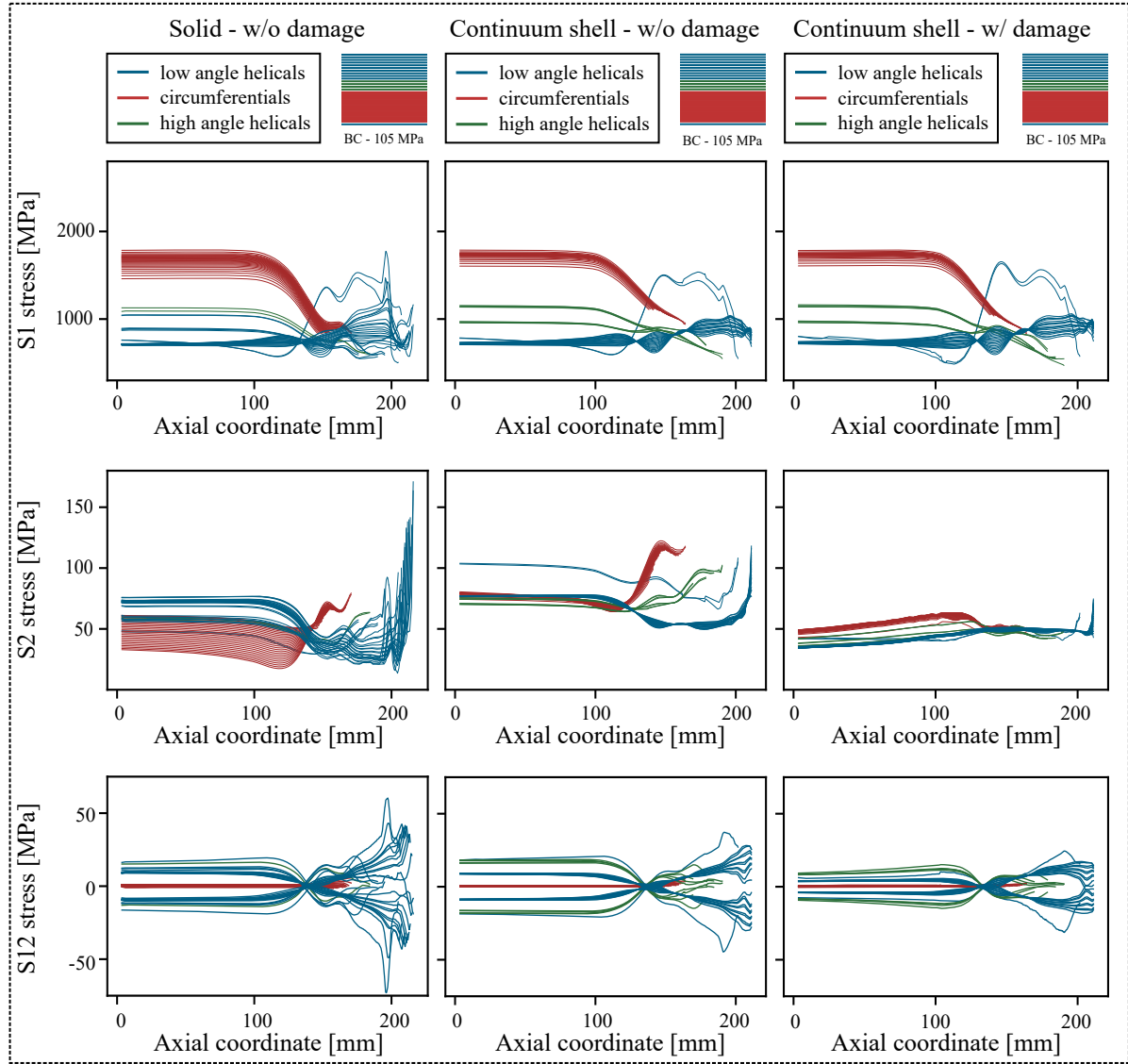


Figure 5.8: Comparison of S1, S2 and S3 per-ply stresses for the BC configuration as computed by the solid model (without damage) and the continuum shell model (with and without damage)

In terms of transverse stresses, the solid and the continuum shell models show different behaviors. Transverse stresses are matrix-dominated, meaning that the impact of the neglect of compressive radial stresses in this case will be significant. Interesting to notice is the transverse loading on the stack on low angle helical plies. When compressive radial loading are included, i.e. in the solid model, the transverse stress of the innermost helical plies decrease. Radial stresses are in fact higher on the inside of the laminate, where they alleviate the in-plane stresses the most. When compressive radial stresses are not included, this alleviation of in-plane stresses is lost. This is the case in the continuum shell model. Shear stresses are also affected by this effect, and appear slightly higher in magnitude for the continuum shell model.

Different considerations should be made for the case when material degradation is taken into account. In terms of longitudinal S1 stresses, a similar trend is found as for the constitutively elastic analysis. This suggests that at the selected pressure stage of 105 MPa the fiber constituent is not yet damaged, and therefore still fully able to withstand the loads. This theory is confirmed when looking at the failure indices for tensile fiber failure plotted for the three vessel types in Figure 5.11, Figure 5.12 and Figure 5.13. Here, it is clear that all failure indices for fiber failure are still well below 1, meaning that no damage initiation nor degradation has yet occurred in the fiber component at 105 MPa internal pressure.

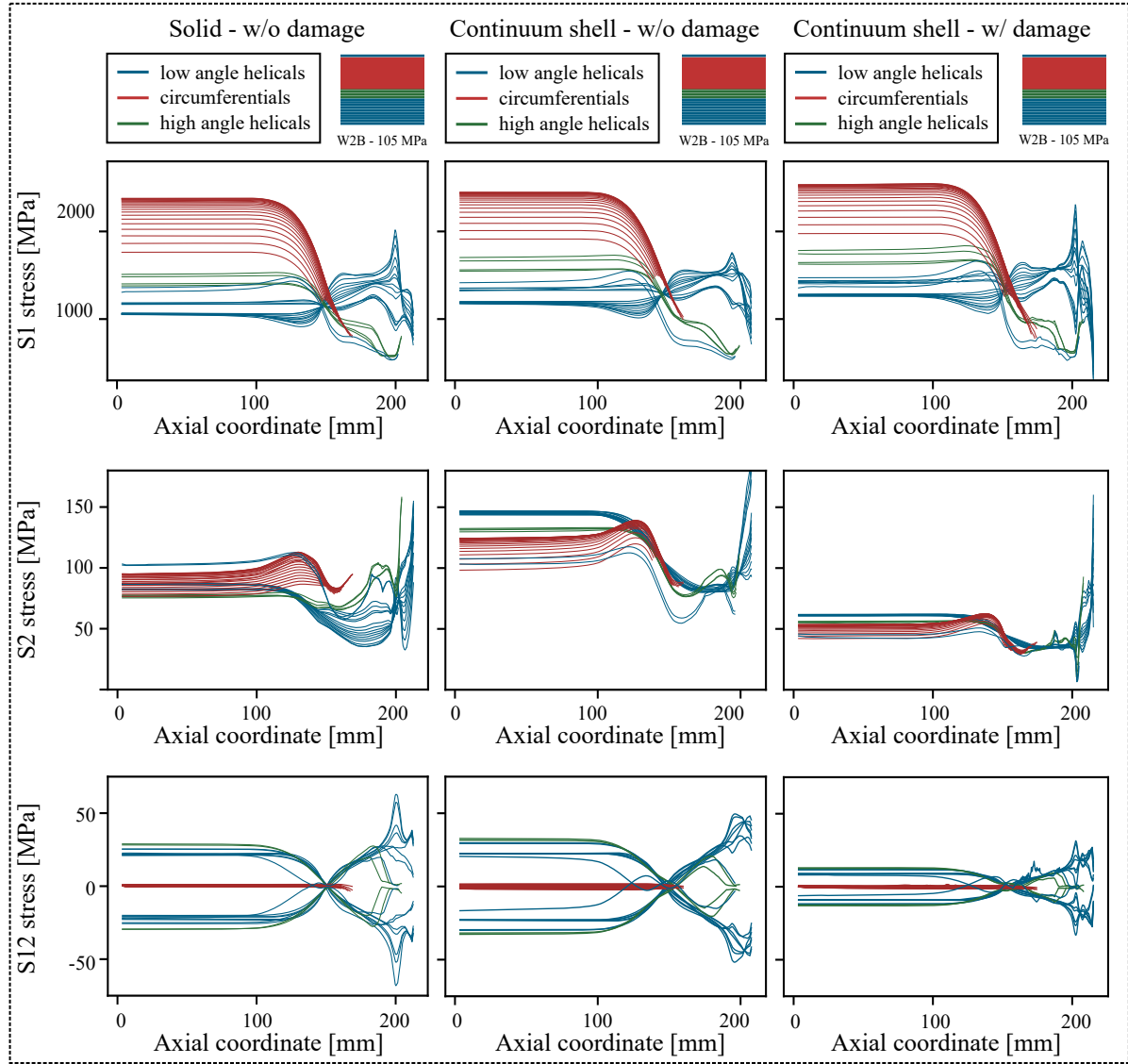


Figure 5.9: Comparison of S1, S2 and S3 per-ply stresses for the W2B configuration as computed by the solid model (without damage) and the continuum shell model (with and without damage)

Transverse stresses, on the other hand, decrease of a full order of magnitude when damage propagation is taken into account. As shown in Figure 5.11, Figure 5.12 and Figure 5.13, matrix failure occurs at very early pressure stages for all vessel types, meaning that at 105 MPa the matrix is fully degraded and incapable of withstanding any load. This has important repercussions also on the S12 shear stress component, which is carried by both the fibers and matrix components. When the material is degraded according to the selected damage progression subroutine, matrix failure is fully accounted for. This means that the laminate is far less capable to carry shear stresses, as now only the fiber component is still undamaged. The drastic decrease in transverse and shear stresses also explains the slight increase in S1 longitudinal stresses in the fiber component, which now have to take on the other in-plane stresses that the matrix is no longer able to carry. An investigation to prove this statement is presented in Appendix B, where the stress-states at 5 MPa are computed for the solid model (where damage analysis is not included) and for the continuum shell model (without and with damage analysis). The investigation shows that at low pressure levels the transverse loading on the matrix is similar for the modelling strategies, suggesting that indeed the reduction of transverse stresses at higher pressure stages is due to the degradation of material properties induced by damage.

Figure 5.11, Figure 5.12 and Figure 5.13 are particularly useful for determining which components experience failure and when. In this sense, they show some insights on the failure sequence of the different layouts. As mentioned, matrix failure occurs far earlier than fiber tension. For all configurations, the failure index for

matrix tensile failure approaches 0.4 on the inside of the cylinder already at 5 MPa internal pressure, and it exceeds 1 at 55 MPa in multiple locations. Insights from microscopy confirm this and show how interfiber fracture develops through the laminate due to matrix tension. An example is presented in Figure 5.10 for a configuration similar to the BL and W2B vessels. The figure shows how the crack propagates uninterrupted between the fibers and through the stack of circumferential plies. The crack is interrupted only when it meets a different reinforcement, i.e. at the interface with the helical plies.

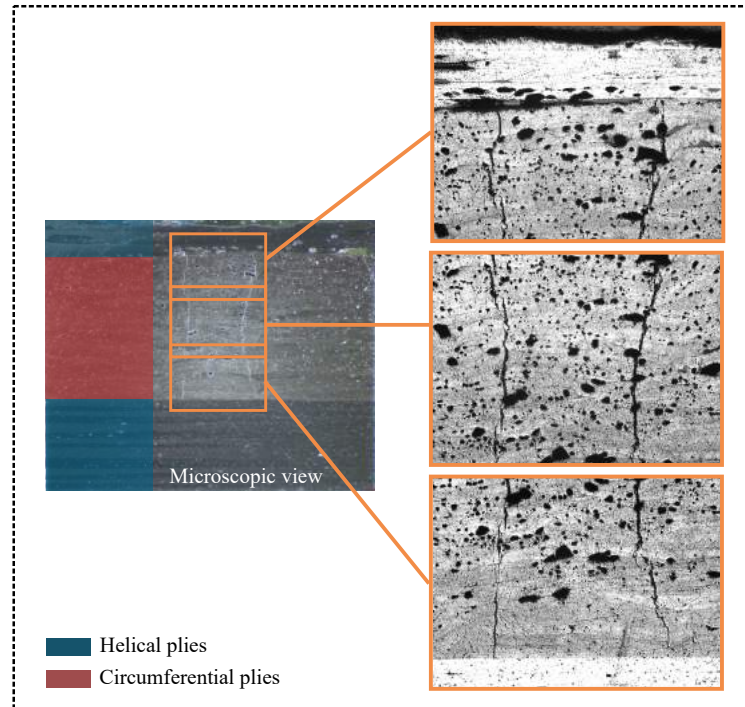


Figure 5.10: Matrix crack propagation through the stack of circumferential plies, due to matrix tensile loading.

The failure index for fiber tensile failure, on the other hand, does not reach 1 in the simulation, and only approaches 0.4 at 105 MPa internal pressure. This suggests that fiber tensile failure occurs at much higher pressure stages. The development of fiber tensile failure depends on the laminate stacking sequence. In case of BL and W2B, the highest fiber failure indices are found in the innermost circumferential ply, as this is heavily loaded in tension due to the high tangential stresses. The stack of helicals underneath, however, are not immune to this critical loading condition. For both cases, at 105 MPa the failure indices rise, suggesting that damage has initiated to degrade the material properties. It should be noted that the sequence is slower in the BL case, as the laminate is thicker and more capable of reinforcing the liner. In case of W2B, the failure indices raise more rapidly. This is confirmed during experiment, as burst is reached at the relatively low pressure level of 126.8 MPa. For this vessel configuration, high failure indices are also found in the dome, suggesting that the simulation provides promising results for the prediction of dome burst.

In case of BC, the fiber tensile failure index increases first in the inner low angle helical ply, as this experiences the highest loading and it is not supported by any additional reinforcement in the same orientation. In order to withstand this extreme loading condition, stresses are transferred to the stack of circumferential plies, which are able to provide the required tangential reinforcement. However, this load-transfer mechanism causes the matrix in the inner ply to be loaded heavily, causing early failure on the inside of the laminate. Once the load is transferred to the circumferential plies, the matrix, typically much weaker than the fibers, is again loaded in tension, leading to high matrix tensile failure indices. Failure then continues to progress outwards, toward the outermost circumferential plies. It should also be noted that in the BC vessel a location of high stress concentration is also found in the inner plies in the cylinder-dome transition region. This is arguably caused by the lack of tangential stiffness on the inside of the laminate, after the circumferential ply drop-off location.

From the stress-state observed in Figure 5.7, Figure 5.8 and Figure 5.9, the procedure presented in Section 5.1.2 is followed to estimate burst pressure. Also in this case, a first ply failure assumption is made,

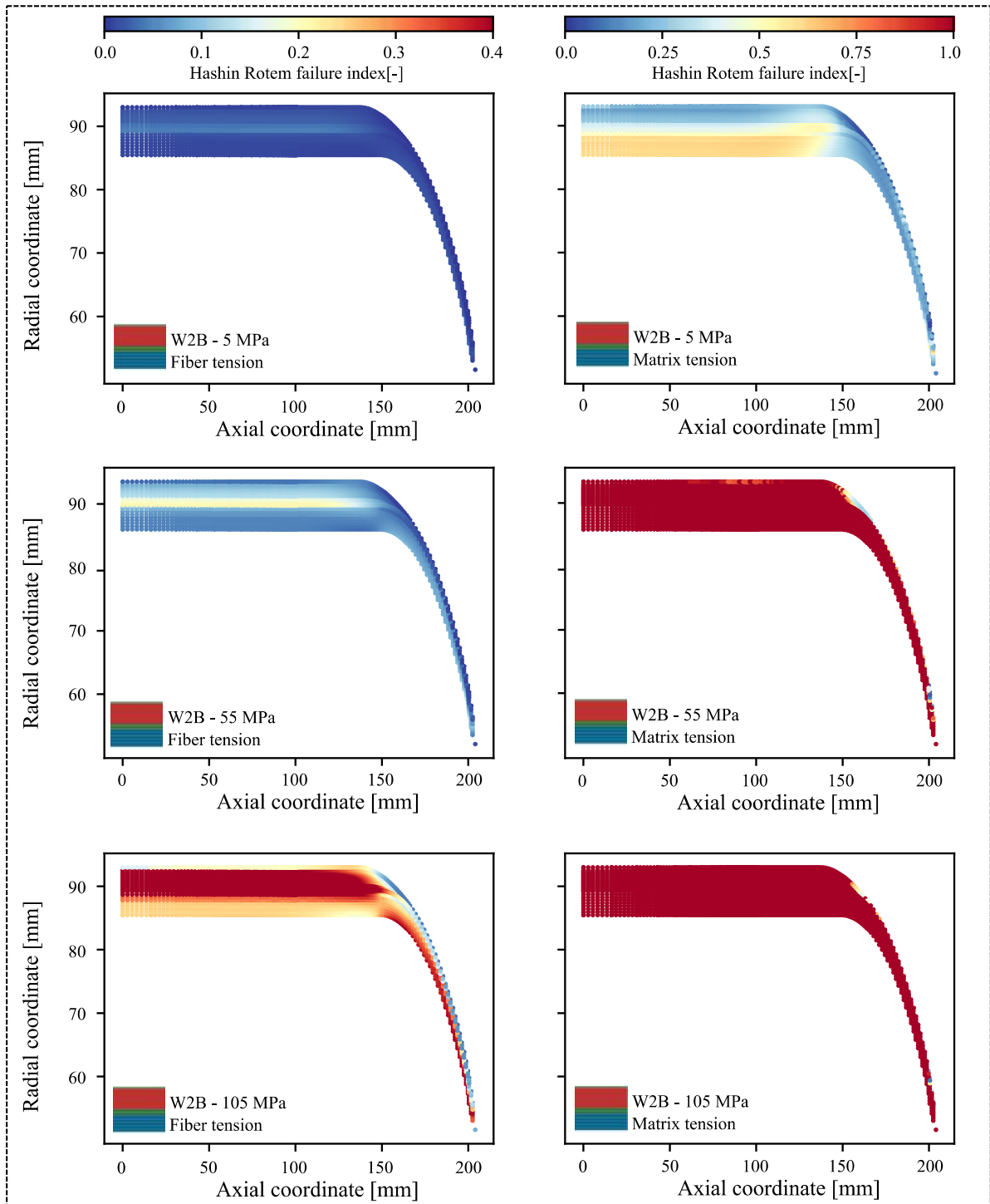


Figure 5.11: Damage sequence for the BL vessel configuration when the Hashin Rotem failure criterion is used to evaluate fiber damage due to tension (left) and matrix tension due to tension (right).

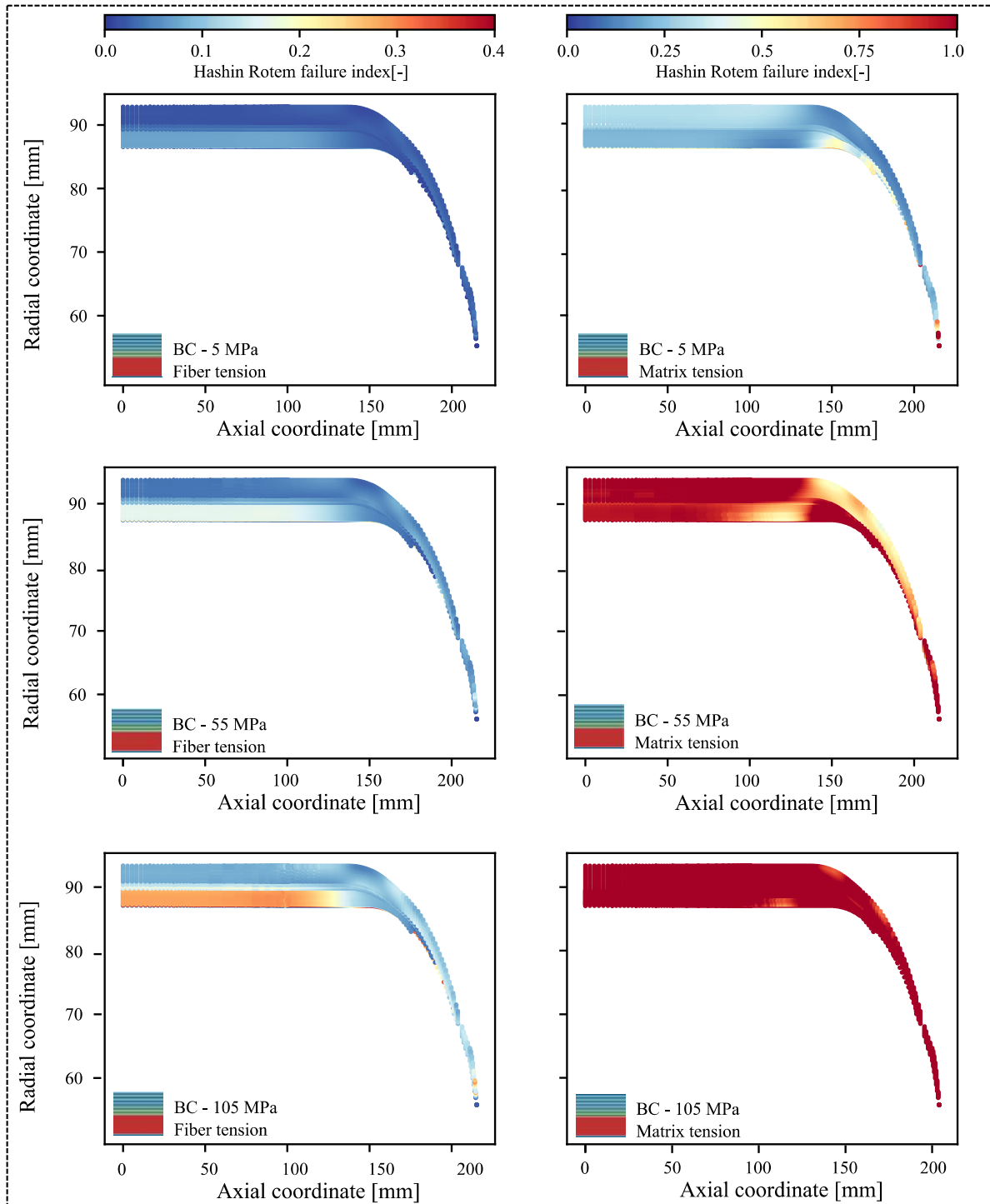


Figure 5.12: Damage sequence for the BC vessel configuration when the Hashin Rotem failure criterion is used to evaluate fiber damage due to tension (left) and matrix tension due to tension (right).

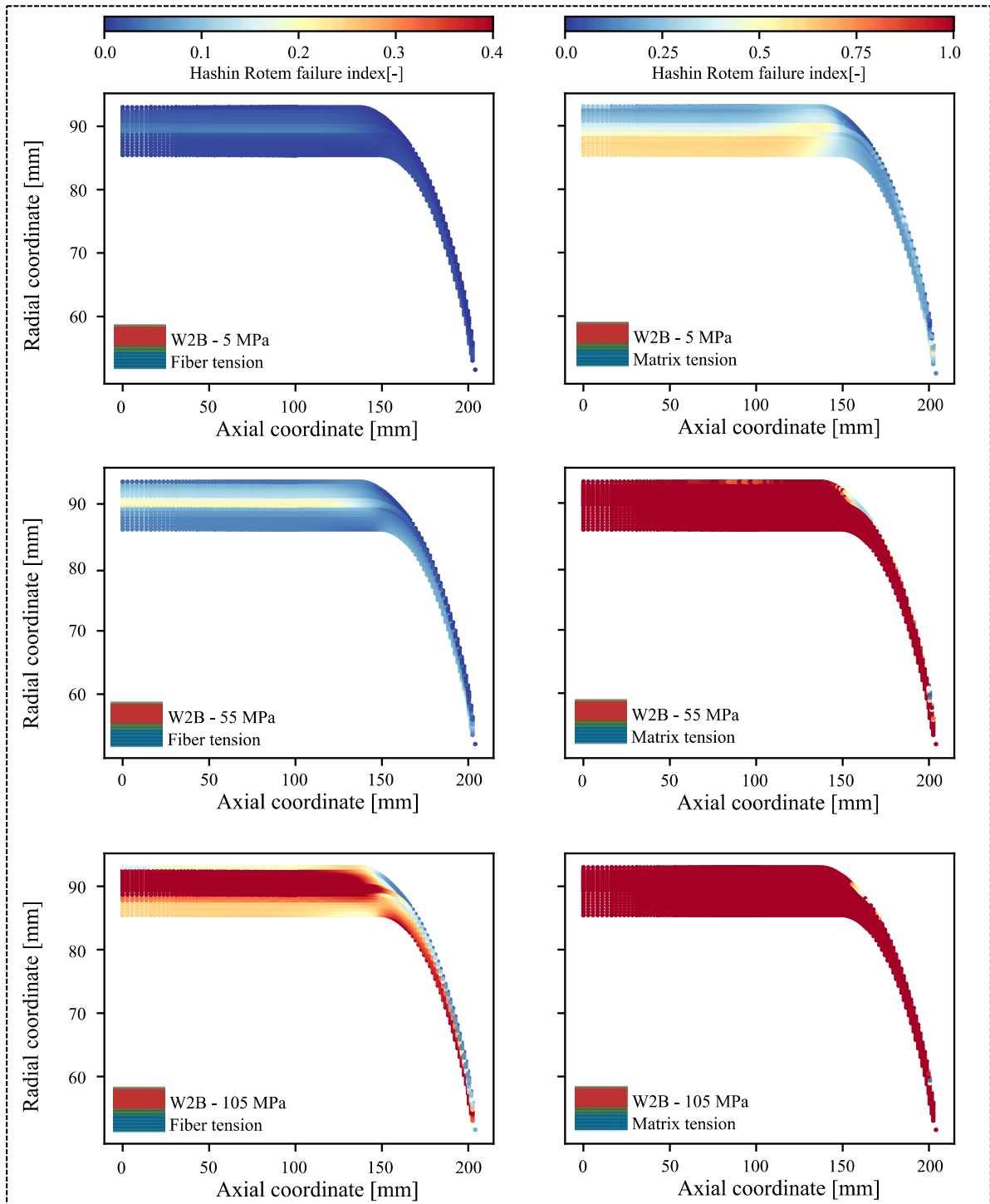


Figure 5.13: Damage sequence for the W2B vessel configuration when the Hashin Rotem failure criterion is used to evaluate fiber damage due to tension (left) and matrix tension due to tension (right).

meaning that the entire laminate is assumed to fail when the first ply fails. In this sense, similarly to what was done for the solid model, the effect of damage after 105 MPa is neglected.

For the constitutively elastic analysis performed by the solid and by the continuum shell models, this assumption translates to the computation of results that do not consider material degradation in any way, neither before nor after the simulated internal pressure level of 105 MPa. On the other hand, for the results of the continuum shell model which consider material degradation by means of Hashin failure criterion, this approach translates to an inclusion of matrix degradation until 105 MPa, and a neglect of fiber degradation until first ply failure, when the entire laminate is assumed to fail at once. This strategy is only valid because it is observed that effectively no fiber damage occurs before 105 MPa, as no failure index exceeds 1 at this pressure stage. This confirms that first ply failure does not occur earlier than 105 MPa, and therefore fiber degradation has not yet started. Furthermore, at this pressure stage, the entire matrix component has already failed, meaning that indeed no subsequent matrix degradation would occur at pressure stages higher than 105 MPa. It should be kept in mind that this is not fully representative of reality. During experiments, as the fracture density in the matrix would keep increasing after 105 MPa, and interlaminar cracks would eventually lead to delaminations. This effect is neglected in the simulation.

In this case, not only the Puck failure criterion is used to estimate the pressure level at which burst will occur, but also a simple maximum stress failure criterion. This is done to mitigate the fundamental difference between the solid model and the continuum shell model, by which radial compressive stresses are neglected in the continuum shell model. As seen in Equation 5.1, the failure index  $f_{FF}$  which describes tensile fiber failure according to Puck failure criterion depends on  $\sigma_3$ , which describes the radial compressive stress. As these are neglected in the continuum shell element formulation, it is decided to apply both failure criteria to quantify the impact of this neglect in the estimation of burst pressure.

The maximum stress failure criterion only relies on in-plane stresses and expresses the failure index  $f_{FF}$  for fiber fracture in tension as:

$$\frac{\sigma_1}{S^I} \geq 1 \quad (5.3)$$

This method allows to check the difference in predicted burst for the solid and continuum shell model only based on the respective stress-state, rather than on the formulation of a selected failure criterions.

As previously explained, the failure indices at the highest simulated pressure stage of 105 MPa are calculated for each ply at each axial location. Then the failure envelope at 105 MPa is plotted to visually grasp an indication of the location where burst is expected to occur. Finally, the pressure stage at which the maximum failure index is expected to reach 1 is computed linearly.

The results for the burst estimation of the BL, BC and W2B configurations are computed by means of Puck failure criterion and maximum stress failure criterion. These are presented in Figure 5.14. The figure shows that the general trend does not change for the two stress failure criteria. In all cases the solid model leads to an overestimation of the estimated burst pressure. As mentioned, this is mainly due to the neglect of any effect of damage, meaning that the material properties do not experience any degradation until failure. The constitutively elastic analysis involving continuum shell elements model provides a similar result, although slightly different when the maximum stress failure criterion is applied. In fact, the continuum shell model results in higher S1 stresses, impacting the result of Equation 5.3. The inclusion of  $\sigma_3$  stresses in the formulation of Puck failure indices, on the other hand, mitigates this discrepancy and alligns the results of the two modelling techniques.

From Figure 5.14, the level of accordance between the simulation and the experimental results increases significantly when including the effects of material degradation due to damage in the determination of the stresses. An overview of all predicted burst pressures is again provided in Table 5.3. The accordance of results is particularly striking for the W2B cases, where damage is predicted in the dome and with a discrepancy in pressure level of only 1.2%. This discrepancy may be caused by many factors, such as imprecisions in the geometrical depiction of the dome, inaccuracies in the definition of the ply angle variations in the dome, or measurement errors in the experimental setup. Furthermore, it should be noted that only a limited amount of vessels is tested for each configuration. For the W2B case, the sample size is 4, therefore still allowing margin for deviations which could be mitigated by performing more tests on the same vessel type.

Including the effects of damage in the simulation helps obtaining a closer estimation for the BL layout as well. Also in this case, the failure location matches the one observed experimentally, i.e. the cylinder. A discrepancy of 10.4% is however still found in the prediction of burst pressure. Despite this being a significant improvement with respect to the previous modelling strategies, this discrepancy may mainly be attributed to

the neglect of the propagation of damage through the fiber component, once fiber fracture is initiated. In fact, the BL configuration is composed of a thick stack of circumferential plies located on the outside of the laminate, meaning that the high tangential stresses travel through the stack of helical plies underneath before reaching the ply type which is able to withstand their high magnitude. Throughout this process, the helical plies on the inside of the laminate are expected to experience significant damage, which effectively alter the load-carrying capabilities of the laminate. Neglecting this effect may therefore have a significant impact on the result. Potentially, the same impact could be expected in the W2B case, as the layups are similar in macroscopic architecture. However, this effect is only relevant for cylinder failure. In the W2B case, the lack of reinforcement in the dome region makes this region critical before this damage-related issue is experienced in the cylinder.

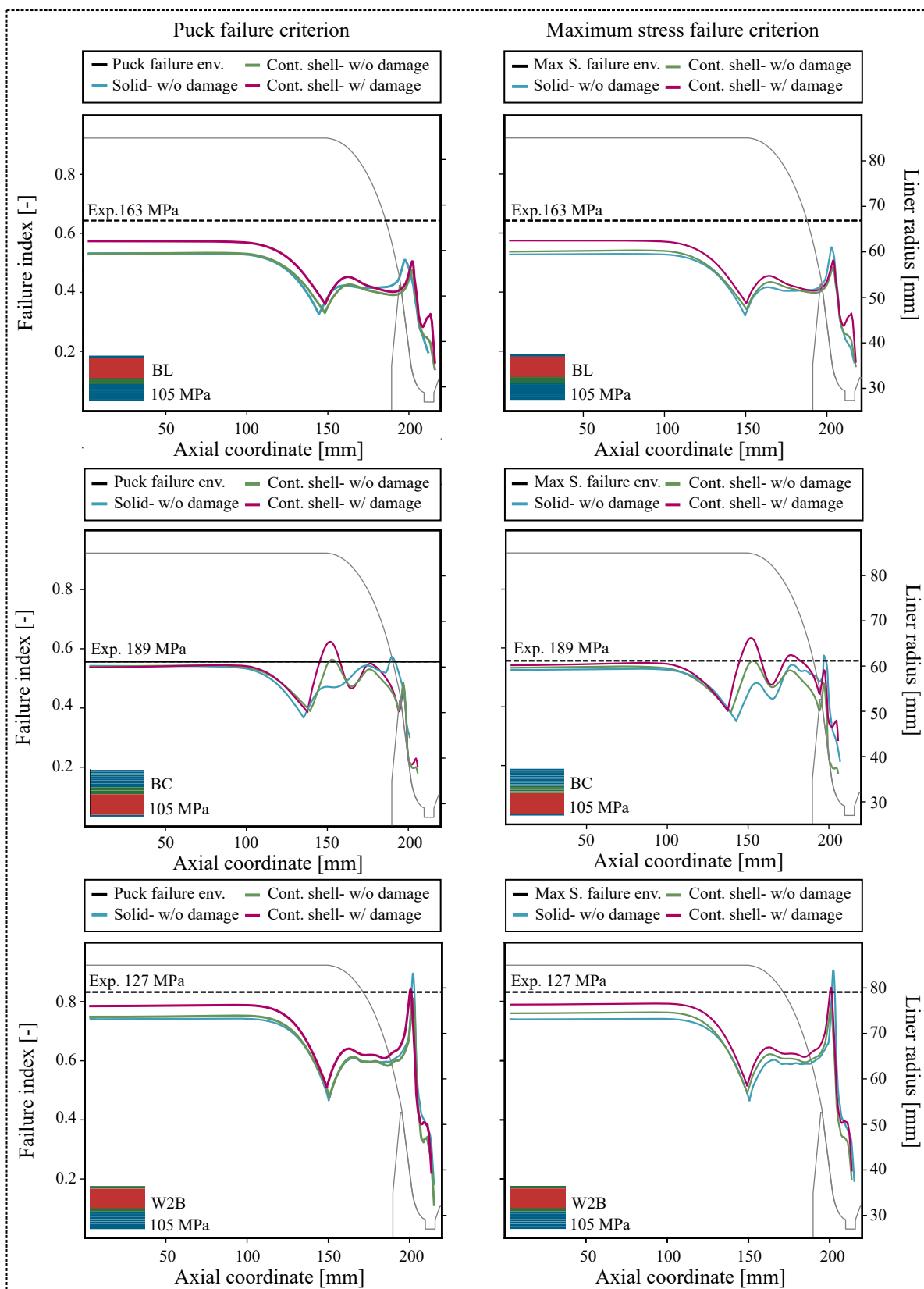
In the case of BC, the burst pressure is predicted very accurately. The discrepancy in burst pressure for cylinder failure is limited to 0.3%. However, the plots presented in Figure 5.14 are more tedious to interpret. Due to the high local stress concentrations found at the cylinder-dome transition region in the innermost ply, a peak in failure index is found at the end of the cylinder, suggesting that failure first occurs at this location. Assessing whether this is really the case is complicated. During burst testing the vessel is found to experience cylinder burst, but establishing whether this really occurred in the cylinder-dome transition region remains difficult. As the laminate is in fact reduced to powder after the explosion, the hypothesis cannot be confirmed nor discarded. On the other hand, it is found that the peak is only reached by the innermost low angle helical ply, suggesting that this local failure would more likely lead to ply failure, rather than burst. With all probabilities, immediately after the first ply failure of the innermost helical ply, the stack of circumferential would reach the critical failure index of 1. Due to the diffused high failure indexed, this would lead all circumferential plies to fail simultaneously, more likely resulting in burst. The per-ply failure indices supporting the hypothesis of a local ply failure in the innermost helical ply are found in Appendix C. In any case, as it is not possible to determine with certainty the location of failure, the prediction reported in Table 5.3 includes in parenthesis the burst pressure reached in the cylinder-dome transition region.

Table 5.3: Comparison between measured burst pressure and predicted burst pressure, obtained from the results of the solid and continuum shell models. The data in parenthesis for the BC configuration refers to the local failure in the cylinder-dome transition region experienced by the innermost low angle helical ply (see Appendix C).

		Puck failure criterion		Maximum stress failure criterion	
		Burst pressure [MPa]	Discrepancy wrt experiment [%]	Burst pressure [MPa]	Discrepancy wrt experiment [%]
BL	Solid (w/o damage)	196.4	20.2	197.3	20.7
	Continuum shell (w/o damage)	195.9	19.9	193.0	18.1
	Continuum shell (w/ damage)	180.5	10.4	179.4	9.8
BC	Solid (w/o damage)	193.0	2.1	193.3	2.3
	Continuum shell (w/o damage)	192.0	1.7	191.9	1.7
	Continuum shell (w/ damage)	189.3 (172.8)	0.3 (8.4)	189.3 (173.4)	0.3 (8.1)
W2B	Solid (w/o damage)	113.0	11.0	113.0	11.0
	Continuum shell (w/o damage)	119.5	5.6	118.4	6.6
	Continuum shell (w/ damage)	125.2	1.2	125.3	1.2

For simplicity, all further discussions in this document refer to the burst estimation according to Puck failure criterion.





### 5.3. Evaluation of Computational Time

Figure 5.15 shows an overview of the wallclock times for all the investigated configurations for the following simulation strategies:

- The previous simulation benchmark. It consists of a solid model which does not consider any material degradation as result of damage propagation;
- The solid model, which does not consider any material degradation as result of damage propagation;
- The continuum shell model which does not consider any material degradation as result of damage propagation;
- The continuum shell model which considers material degradation as result of damage propagation.

In all cases, the same system of 4 core processors is used for the analysis. The comparison is done by keeping both the angle of revolution of the geometry and the level of partition constant in all models. Specifically, a revolution angle of 5 degrees is chosen; the through-thickness partitioning is done per-ply-group, leading to 4 through-thickness elements in all models; the axial discretization is standardized to 121 cells along the length of the half-vessel.

The developed simulation strategies lead to extreme improvements in terms of computational time, with respect to the previous benchmark. As presented in Chapter 3, the time reduction is mainly achieved thank to the reduction in model size. This is obtained by generating stacked solids of revolution which only span for a limited revolve angle, in this case set to 5 degrees. In comparison, all previous simulation strategies developed at cellcentric GmbH spanned an angle of 90 degrees, leading to much higher computational times.

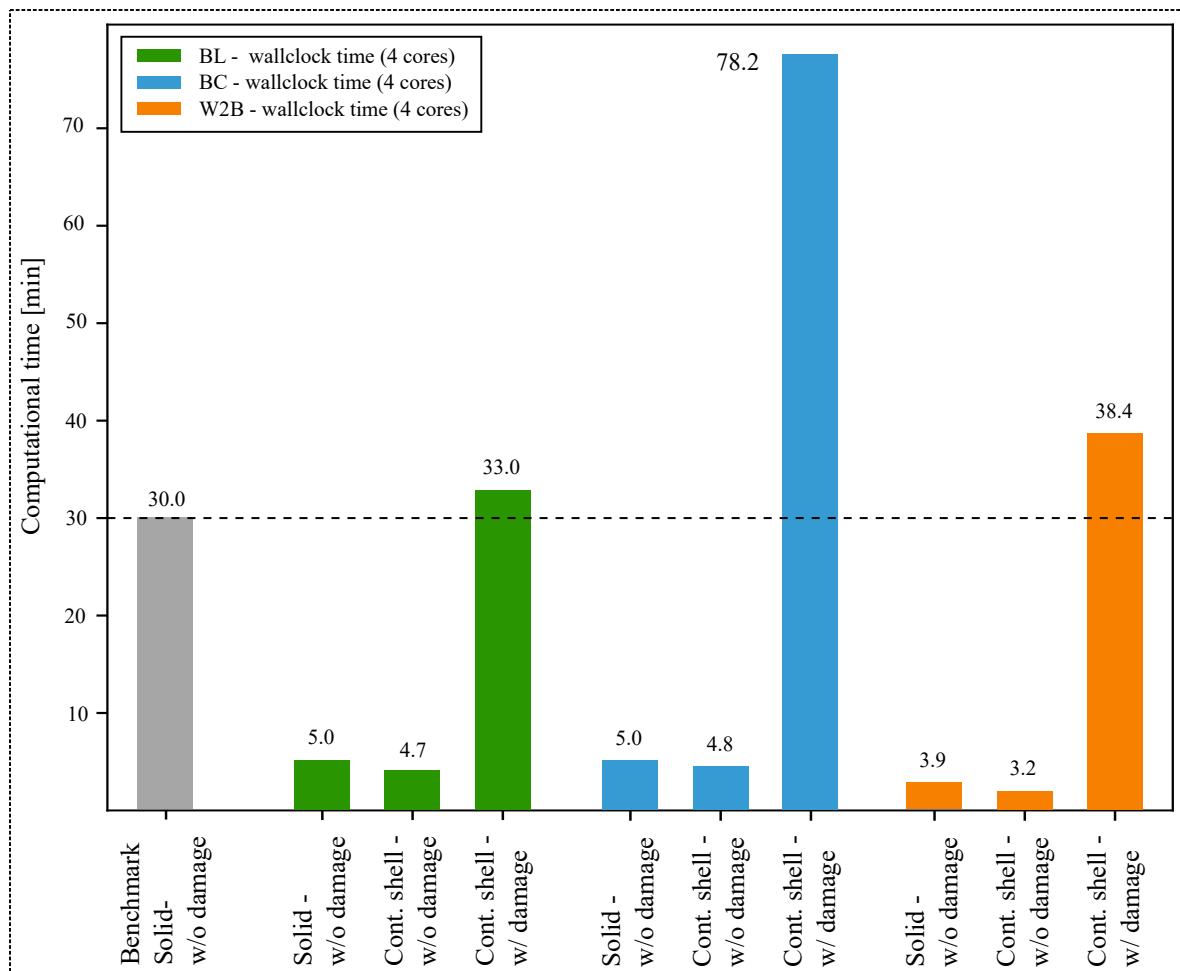


Figure 5.15: Overview of computational times of all developed modelling strategies for the investigated layouts.

When damage is not considered, the solid model and the continuum shell model lead to similar computational times. This is expected, as the thickness of the material is discretized similarly for the two element formulations. The computational time is slightly lower for the W2B case. This is intuitive as the laminate is thinner, therefore leading to a smaller model size.

When Hashin Rotem failure criterion is implemented in the solution to account for material degradation due to damage, the computational time increases significantly. This is expected, given that now the material performance is re-calculated at every iteration simulating the new degraded material properties.

For the BL and W2B configurations, the computational time now exceeds 30 minutes. In this case, the W2B case is slightly more expensive as this configuration experiences more damage. This makes the stiffness matrix less stable and full convergence more difficult to achieve. A separate consideration holds for the BC case, for which the computational time almost doubles that of BL and W2B. In case of BC, convergence is difficult to achieve arguably due to the direct application of the load on the highly degraded elements of the innermost low angle helical plies. Figure 5.12 shows that this layer is highly damaged even at low pressure stages. In some cases, this leads to excessive element distortion which may translate in convergence issues. The stability of the model is also complicated by the sudden change in stiffness caused by the stack of circumferential plies located right above. In turn, this combination of effects requires significant manual adjustment to match the properties of the as-manufactured CPV. This leads to the high computational time presented in Figure 5.12. Further discussions on how to address this issue are presented in Chapter 6.

# 6

## Model Applicability for the Design of CPVs

CPVs are sophisticated and complex structures and their full understanding is yet to be achieved. Critically-loaded areas are often over-designed to avoid unpredicted failure. This, however, results in high costs. Continuing to investigate CPVs is important, with the final objective to obtain an optimized layup. This shall fulfill all structural requirements without a massive weight increase. Although this objective exceeds the scope of this investigation, meaningful effort is done to expand the level of understanding of CPVs during pressurization, and to provide a solid foundation for future research. The modelling framework is meant to be used within industrial settings, to facilitate the development of CPVs by providing a realistic representation of the laminate response at low computational time. This chapter is therefore intended as a manual, shedding light on how to implement the developed modelling strategies for different design purposes.

The extensive database of experimental results available at cellcentric GmbH offers the unique opportunity to test the simulation on multiple configurations and, to some extent, to assess its replicability. However, the potential of the framework reaches further than the BL, BC and W2B vessels. The method is highly reproducible, which allows to contribute to the development of CPVs actively. In fact, it can be re-applied to different configurations to predict the CPV behaviour consistently. Thanks to this consistency, the simulation tool is useful for design purposes, to analyze a variety of configurations. Section 6.1 summarizes the different potentials of the model.

The application of the numerical framework to different cases requires a critical evaluation of the proposed adjustment strategies. The level of accuracy in the depiction of the geometry and material composition of the investigated vessels proves that the adjustments are, to some degree, not layup-dependent and valid for a variety of type IV tanks. However, it is found that these adjustments influence the CPV configurations to different extents. This is discussed in Section 6.2.

The performance of the simulation tool is not only evaluated based on how accurately it can predict reality. For it to be useful, it must also be fast. In fact, the automotive industry is characterized by short development phases and quick design choices. The importance of minimizing the computational time is further discussed in Section 6.3, where alternatives to reduce the simulation expenses are presented.

### 6.1. A Twofold Potential

This research has the purpose to improve the pre-existing simulation strategies by decreasing the computational costs and improving the accuracy of predicted outer strains and estimated burst pressure. Furthermore, it aims to anticipate failure both in the cylinder and in the dome regions. Within the automotive industry, these aspects are crucial.

Limiting computational time is extremely important throughout preliminary design phases. At this time, decisions must be taken quickly to evaluate the feasibility of a specific solution and to decide whether a technology is worth further investigations.

Increasing accuracy, on the other hand, is fundamental at later stages throughout detailed design phases. Usually, these include optimization studies to minimize material usage and costs. This can only be achieved when a close prediction of the structural behavior is reached, to avoid over-designing. Eventually, a thorough reproduction of the mechanical response of the CPV will also grant a reduction of the safety margins, again scaling down the requirements on the structure.

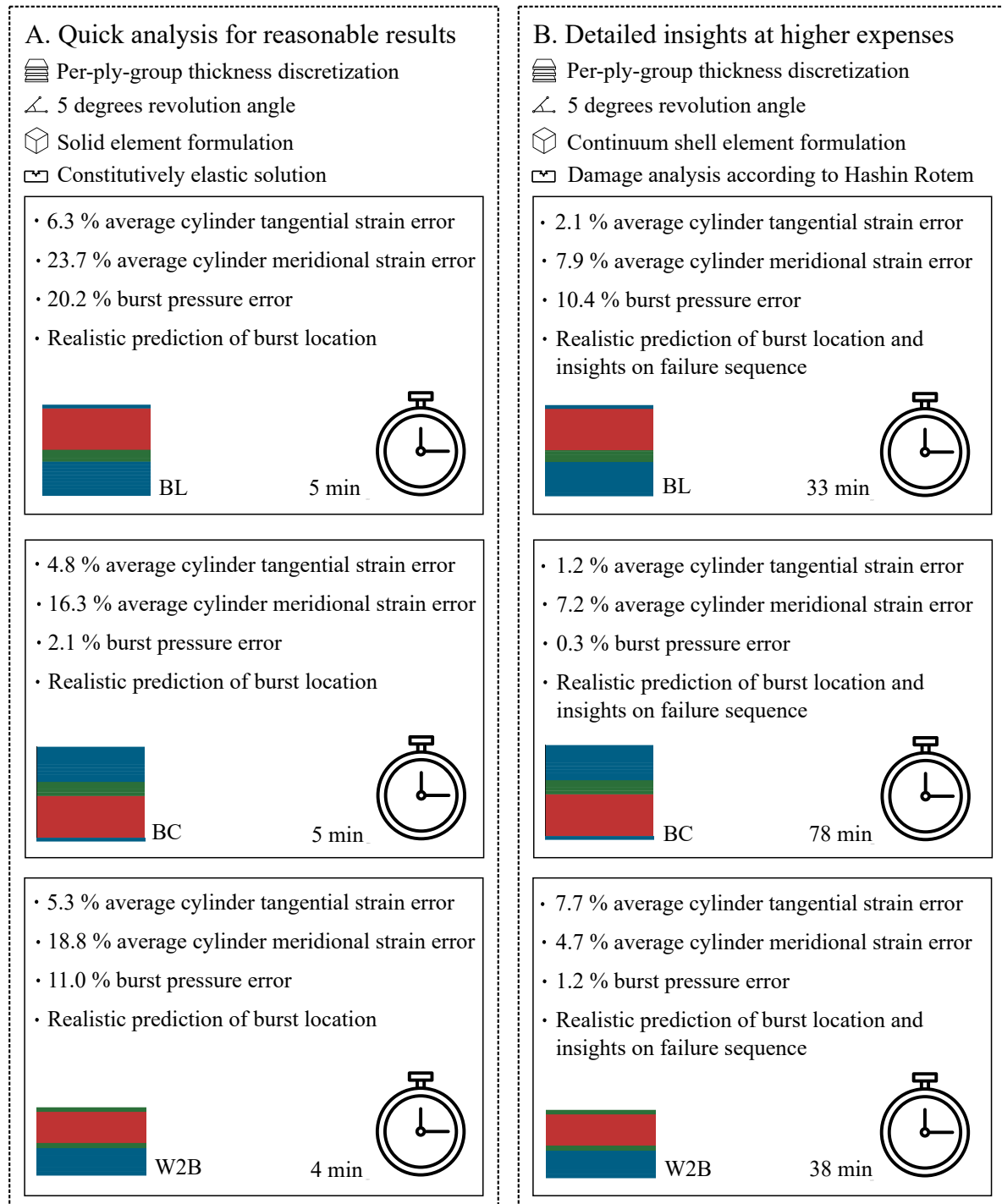


Figure 6.1: Schematic of results for the BL, BC and W2B configurations to show the twofold potential of the modelling strategy.

In this context, the developed modelling technique has a twofold potential. The user has the freedom to choose which element formulation to utilize according to the specific design context. The choice is requested before the model generation step and it requires minimum user input. The achievements of options are presented graphically in Figure 6.1 for the BL, BC and W2B configurations. A brief description is provided below:

- Option A - leads to reasonably accurate results at extremely low computational times. This numerical approach improves the prediction of outer strains significantly when compared to the benchmark. For

the BL case, for example, it reduces the discrepancy with the experimental results from 13.6% to 6.3% for outer tangential strains, and from 28.6% to 23.7% for outer meridional strains. Burst pressure, in this case, is predicted with an accuracy of 79.8%. The main advantage of this model is its low computational expense. For this example, it runs in 5 minutes, thus 6 times faster than the benchmark. Both models rely on a solid element formulation.

- Option B - leads to significantly improved results that are not only capable of predicting closely the vessel behavior, but also provide insights regarding the initiation and evolution of interfiber failure. For the BL case, the discrepancies with the experimental data further reduce to 2.1% for outer tangential strains, and to 7.9% for outer meridional strains. Burst pressure is also estimated more closely, leading to an accuracy of 89.6% for this configuration. These improved results, however, come at higher computational costs: the simulation runs in 33 minutes for the BL example. Despite being slower than the solid model, the computational time of the continuum shell model is comparable to that of the less-accurate previous benchmark. For the latter, however, the effect of damage was not considered in any way.

It should also be noted that this model is able to predict both cylinder and dome failure with remarkable accuracy, depending on the vessel configuration. The lowest discrepancy is achieved for the BC case, for which cylinder burst is predicted with a negligible error of 0.3% with respect to the experimental result. One of the most important successes of the study is the high accuracy achieved in the prediction of dome burst for the W2B configuration. In this case, the error in burst pressure is limited to 1.2%. Dome burst is rarely predicted numerically, due to the complexity of the doubly-curved geometry which is tedious to recreate. Its material composition is also highly unknown. For this reason, the accomplishment of this prediction is promising, because it proves that dome burst can be tackled. A tool which is able to predict dome burst has the potential to improve the understanding of this region and allow to tune the amount of material accordingly, avoiding over-designing.

The two models can also be used in unison to verify each other. When applied on new configurations for which experimental data is not available, Option A can serve as quick confirmation of the trends in deformational behavior gathered by means of the more time-consuming Option B.

Figure 6.1 shows a schematic summary of the performance of the two modelling techniques. Of course, when analyzing these outcomes, one should keep in mind that the experimental data also has limitations. These are linked to the limited amount of tested vessels, and to the inaccuracies which may arise due to a slightly decalibrated test setup or due to manufacturing defects.

Although the figure is limited to the three configurations in analysis, the trend is expected to hold for a much wider variety of vessels. Therefore, regardless of the vessel type, it is advised to select either one of the modelling techniques based on the required speed and accuracy of the specific application. If quick results are needed, Option A is preferred. Option B is useful when high accuracy is required.

Finally, further tuning can be applied by refining the level of discretization of both models. As all pre-processing steps are fully parametrized, the tool is already predisposed to allow such refinement. However, it should be noted that the increasing the level of partitioning does not only lead to more accurate results, but also to significantly higher computational times. This is investigated in detail in Appendix A.

## 6.2. Adjustment of Vessel Properties on Different Vessel Configurations

In Chapter 4, several strategies are proposed to ensure that the simulated laminate definition matches that of the filament wound vessel. It is important to quantify the impact that these adjustments have on different vessel configurations and in different areas of the vessels. This clarifies how they would affect a wider variety of configurations.

The first adjustment is done to the geometry of the tank. Matching the simulated vessel shape to that of the filament wound CPV is of crucial importance. This is directly related to the stiffness of the structure, it has an impact on the load distribution and it regulates the formation of highly concentrated stresses.

The developed simulation tool utilizes two methods to adjust the geometrical definition of the vessel. On one hand it modifies the thickness build-up of each ply at its turnaround point to smoothen the vessel contour. On the other hand it applies Kang's model [31] to account for the effects of compaction during winding.

The first approach is of utmost importance in the dome region, where helical plies reach their turnaround point and switch direction, generating a balanced laminate. The smoothening of the vessel contour does not

only lead to an accurate prediction of the dome profile, but it also alleviates some numerical inconsistencies found in this region. These are caused by the sudden increase in stiffness that the predicted peak-like thickness accumulation leads to. Numerical models are in general not compatible to sudden stiffness changes between subsequent elements. These give origin to unrealistic element deformations and important convergence issues. The result is high computational times and unreasonable results. The application of such adjustment method is beneficial for all three investigated layups, as for all the prediction of Composicad is not capable of calculating the thickness build-up of helical plies at their turnaround location. In addition to the thicker profile caused by the turnaround of low angle helical plies, the location around the boss neck may also include thick accumulations of resin which do not carry any load. These develop from the curing process, when the vessel is rotated and resin tends to flow towards the boss. In turn, matching the simulated vessel contour to the filament wound vessel may lead to an overestimation of the load-carrying material of this area. In fact, the adjustment does not distinguish between the matrix and the fiber component. It is advised that for vessel configurations composed of a high amount of helical plies, the estimation of the vessel contour at the boss neck is revised.

The adjustment of the vessel geometry is crucial also in the cylindrical region of the vessel. Here, the presence of circumferential plies leads to high levels of compaction. In turn, this results in a drastic thickness reduction. The compaction model implemented in this research is capable to capture this phenomenon, which depends on the orientation of each specific ply and on the stacking sequence. Therefore, this adjustment method is ready to be consistently applied to potentially any vessel configuration. Compaction, however, does not only affect the vessel geometry but also its material composition. When the laminate is compacted, the air voids dispersed in the resin are squeezed out of the material. The removal of voids from the laminate effectively improves the load-transfer capabilities of the matrix constituent, resulting in enhanced material properties. When simulating this effect for a large batch of configurations, the following implications must be taken into account:

- The level of compaction varies per plies, and therefore each ply will have a different thickness and different material properties. This is inherently accounted for in the developed model.
- Different areas of the vessels are not compacted to the same extent. The stack of circumferential plies in the cylinder guarantees high levels of compaction. These are missing in the dome region, leading to a more porous laminate. The adjustment of material properties is based on the level of compaction reached by each ply in the cylinder, meaning that the material properties of the laminate in the dome region are slightly overestimated. This should be kept in mind when analyzing vessel configurations that are critically loaded in the dome. In general, it is recommended to use this model in a conservative manner in this region. In reality, dome burst may occur prematurely if a further adjustment of material properties in the dome area is not performed.
- Vessel configurations with the same layup composition experience different levels of compaction depending on the stacking sequence. For instance, this is the case of BL and BC. Due to the through-thickness location of the stack of circumferential plies, the BL and BC laminates are compacted differently, resulting in different fiber volume contents and material properties. When considering a larger set of vessel configurations, one should keep in mind that the evaluation of compaction and the respective adjustment of the laminate material composition must be done for every configuration separately.

The simulation tool adjusts the vessel geometry and its material composition in the pre-processing phase, meaning that no additional computational time is added to the simulation. This is particularly convenient in industrial settings, where a large batch of vessels data can be prepared and stored in compact *.json* files for future simulations. These files include dictionaries that collect all the geometrical and material information on the CPV prior pressurization in an organized fashion. This approach has been efficiently implemented throughout this research and can be extended to include in the database a variety of configurations.

Once the model is generated in Abaqus and the internal pressure loading is applied, its material composition is updated iteratively as damage propagates, as explained in Chapter 4. The implementation of material degradation due to damage is highly dependent on the vessel configuration.

As introduced in Chapter 5, stacking sequences where the circumferential plies are located on the inside of the laminate are less affected by the implementation of damage. This is due to the strategic location of the circumferential plies which are placed where the critical tangential stresses are highest. In turn, this prevents the helical plies from being heavily damaged, resulting in a less-degraded material definition. This

is for example the case of BC, for which the inclusion of material degradation due to damage is found to not significantly improve the simulation results. The opposite holds for BL and W2B. In general, the inclusion of material degradation in the simulation will have an impact on the prediction accuracy whenever damage is largely developed. This typically occurs in two cases. Firstly, when large deformations occur. This may be the case in the dome or at the cylinder-dome transition region, due to the local decrease of tangential stiffness. Secondly, when loads need to be transferred from highly compliant layers to stiffer layers.

### 6.3. Minimizing Computational Time

The full potential of the developed model becomes apparent in relation to the low computational time it achieves. As presented in Chapter 5, the reduction of the model volume and its efficient partitioning reduce the computational time to up to 83% as compared to the previous benchmark which relies on the same solid element formulation. The main difference between the two is the angle of revolution by which the laminate contour is revolved. This equals 90 degrees for the benchmark model developed by Johman [32], as opposed to 5 degrees for the new simulation strategy. Further reducing the angle of revolution is unadvised, as numerical instabilities are found at the boundaries as shown in Chapter 3. The revolution angle of 5 degrees is therefore chosen to consistently be able to extract the results along an uncontaminated path, which is confidently far from the boundary.

In case higher computational efficiency is required, it is therefore advised to change the model element definition rather than reducing the angle of revolution any further. An attempt in this directions has been performed throughout this investigation by substituting solid and continuum shell elements with axisymmetric elements. In this case, the planar dimensions of the element reduce to zero, potentially decreasing the computational time significantly. Despite its convenience, this strategy requires a completely different definition of the vessel layup. As this implementation exceeds the scope of this study, it was decided not investigate the different layup formulation further, but rather to describe the material properties of the vessel based on those of the equivalent laminate. In this sense, for every axial location along the vessel length the equivalent material properties are calculated and attributed to the respective element. Therefore, no layup was assigned to the geometry. The result is an extremely fast model, which runs in less than 1 minute. The outer tangential and meridional strains for the BC case are plotted in Figure 6.2, which also shows the experimental data. A comparison of the computational time of the axisymmetric model and the solid model is included in the figure. The following limitations should however be noted. Firstly, the material definition of the axisymmetric model is inaccurate, and it neglects the layered structure of the laminate. Furthermore, the axisymmetric model at its current status is not able to capture any through-thickness effect, nor to account for material degradation due to damage. In other words, the material definition of this model is rudimental and should be further refined if higher computational efficiency is needed. Finally, it should be kept in mind that this element type does not allow for a straight forward implementation of a damage progression subroutine.

When damage is included in the analysis, the most easily-implementable and computational efficient strategy involves continuum shell elements. However, this leads to an increase of computational time, as compared to the equivalent solid model which does not involve any damage analysis. As shown in Figure 5.15, distinct trends are observed for the analyzed configurations. As the damage variable of each element increases and the equivalent stresses that the laminate can carry decrease, the computational time typically rises. This is due to multiple reasons.

Firstly, the iterative calculation of the stiffness matrix requires time. To give an example, the W2B vessel is less stiff than the BL case and it experiences failure at an earlier pressure level. Therefore, at the simulated internal pressure of 105 MPa, its laminate is more damaged. The stiffness matrix requires re-calculation starting from early in the integration, effectively resulting in higher computational times. For this reason, the W2B configuration takes longer to converge, despite having a smaller volume than the BL configuration. In general, vessels that experience higher level of damage tend to take longer to converge.

A second source of convergence issues is the instability of the updated stiffness matrix and the respective unrealistic element deformation. For example, the struggle to converge becomes extreme for BC configuration, for which the computational time more than doubles that of BL. In the case of BC, the innermost low angle helical ply experiences high levels of damage due to the thin reinforcement it provides internally. This thin solid is also placed in proximity to a region of sudden increase in stiffness: the interface with the stack of circumferential plies. This results in numerical instabilities that cause significant element deformations. A finer partitioning helps to mitigate this issue, as it smoothens the stiffness gradient through the thickness. Alternatively, extensive manual tuning of the element stiffness are needed to prevent excessive element de-



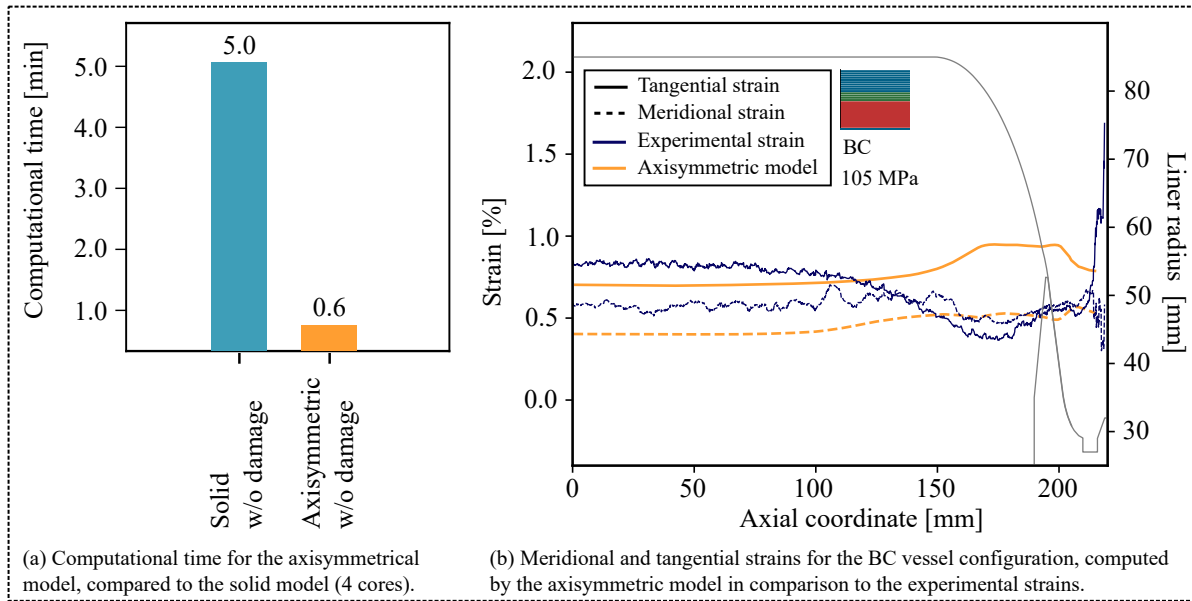


Figure 6.2: Overview of the computational time and strain response of the axisymmetrical model.

formations.

In general, it can be concluded that to closely predict the true behavior of CPVs to account for the effects of damage, a variable amount of manual adjustments is required for each vessel. The higher the amount of adjustments, the higher the computational time. To apply the model efficiently, it is therefore recommended to avoid the implementation of material degradation due to damage if the laminate is subjected to sudden changes in stiffness between its elements.

The stacking sequence already provides some insights on whether the inclusion of the damage progression subroutine is useful. The presence of a stack of circumferential plies on the inside of the laminate (as it is for example for the BC configuration) suggests that damage does not impact the vessel behavior substantially in the cylinder. The circumferential plies are capable of carrying the high tangential stresses before they reach and damage the stack of helical plies. In other words, the cylinder of the BC configuration is meant to experience less damage as the tangential reinforcement is placed exactly where needed. When this is the case, the inclusion of damage in the analysis is less effective, as it leads to a significant increase in computational time without necessarily improving the results. It should however be noted that, in case of large deformations, the impact of damage is more relevant. For instance, this may occur for similar configurations in which the circumferential tapering is steeper, or in which the dome has a weaker reinforcement.

Finally, when the innermost plies are not indicated to carry the critical loading, as for the BL and W2B cases, the implementation of a damage progression subroutine is highly recommended. This affects the material definition of the vessel significantly, therefore making the increase in computational time worthy. For these reasons, regardless of the design phase that one is tackling, it is fundamental to firstly analyze the vessel qualitatively to make sure that the selected modelling strategy is appropriate for the application.

## Conclusions and Outlook

### 7.1. Summary

The gradual shift towards carbon-neutral means of transport has led the automotive industry to the development of fuel cell electric vehicles (FCEV) as alternative to internal combustion engines (ICEs). A crucial element of every fuel cell system is the hydrogen storage structure which most often consists of a Type IV composite pressure vessel (CPV). CPVs are not new to the automotive industry and are technologically ready for use. However, the carbon fiber reinforced polymer CFRP material used for these tanks is costly and its reduction would be highly beneficial for the economic viability of the system. The challenge is how to reduce material usage without compromising the structural integrity and safety of the vessel. Good understanding of the structural behavior of CPVs is necessary to achieve this purpose.

This report presents the development of a robust and computationally efficient numerical model for the analysis of CPVs. The objective of the tool is to obtain an accurate prediction of the structural response of CPVs to internal pressurization, and to lower the time required for the analysis of these complex components. The applicability of the simulation strategy is assessed on three vessel configurations, with the purpose to evaluate its systematic prediction of the deformational behavior of CPVs and its ability to forecast the appropriate burst pressure and location.

#### 7.1.1. Numerical Framework

The developed numerical framework relies on the rudimental laminate architecture generated by the winding software Composicad. This provides a preliminary estimation of the vessel geometry based on the motion of the winding robot. This estimation however requires several adjustments to match the shape of the manufactured CPV. The laminate contour is firstly modified to account for the thickness accumulation of helical plies at their turnaround point and to smoothen the dome profile. An analytical model is then applied to account for the effects of compaction during winding. Following the example of previous studies, the thickness decrease caused by compaction is estimated according to the model proposed by Kang et al. [31]. Compaction does not only affect the laminate geometry, but also its material properties. As each ply experiences a different level of compaction based on its orientation and its position through the thickness, the consolidation level varies. The porosity gradient leads to heterogeneous material properties. An engineering solution which relies on the assumptions of classical lamination theory (CLT) is developed to adjust the material properties of each ply and compensate for the reduced stiffness caused by the thickness reduction.

Once the geometry and material composition are adjusted to match the filament wound CPV, the laminate information is used to recreate the vessel in the Abaqus software. The model generation is fully parametrized, allowing the analysis of various vessel configurations. A method to reduce the model size is developed to ensure fast computation. Adequate level of accuracy is achieved by partitioning the vessel geometry along its longitudinal axis and through the thickness.

Within the Abaqus environment, two models are developed. The first one is based on solid elements and it provides reasonably accurate results at low computational expenses. Furthermore, it allows to directly compare the model performance to that of the previous benchmark. The second one, more sophisticated, is built on continuum shell elements. This accounts for material degradation due to damage propagation according to Hashin Rotem failure criterion. However, it comes at higher computational costs.

According to the specific application, the user may initiate either one of the finite element (FE) methods. In any case, both element formulations require similar pre- and post- processing steps, meaning that regardless of the selected modelling strategy, the model generation and the data extraction do not require any manual adjustment.

The numerical framework is tested on three vessel configurations. The BL and the BC configurations have the same layup composition but differ from each other in terms of stacking sequence. They are selected to assess the capability of the model to predict cylinder failure. The addition of the W2B configuration to the set represents one of the greatest challenges of the research. This configuration has experienced dome burst in experimental settings. Dome burst is difficult to predict, due to the doubly curved geometry and the material heterogeneity of the region which make the simulation particularly tedious. Testing the numerical model on the W2B vessel thus allows to assess to which extent this is able to predict this complex failure behavior.

### 7.1.2. Results and Applicability

Both modelling techniques provide interesting insights on the mechanical response of CPVs. The solid model runs in less than 5 minutes for all the investigated configurations, reducing the computational time with respect to the equivalent previous benchmark of more than 83%. It also provides reasonably accurate results in the depiction of the deformational behavior, especially when the circumferential plies are located on the inside on the laminate as for the BC configuration. In this case, they are able to carry the critical tangential stresses where they are highest, i.e. in proximity of the liner. This leads to close accordance of outer strains to the experimental data gathered by means of digital image correlation (DIC). Discrepancies are limited to 4.8% for outer tangential strain and 16.3% for outer meridional strains. Cylinder burst is estimated with an accuracy of 97.9%.

When the circumferential plies are located on the outside of the laminate, however, the innermost helical plies are damaged by the heavy tangential loading. This is the case of the BL and W2B configurations. The insights provided by the continuum shell model here are more useful, as it accounts for the progressive degradation of material. In both cases, significant strain accordance is found in the tangential and in the meridional direction: the maximum discrepancy with experimental data is limited to 7.9%. Furthermore, cylinder burst is predicted with 89.6% accuracy for the BL configuration. For the W2B vessel, remarkable accuracy is found in the estimation of dome burst, predicted with an accuracy of 98.8%. Despite being more computational expensive than the solid model, the continuum shell model is deemed as fast as its solving time is comparable to that of the previous benchmark, which did not involve any damage analysis.

For this reason, both modelling approaches are useful and fulfil a twofold purpose. The automotive industry is characterized by short development phases. In this context, the solid model may provide for quick and reasonably accurate results to take fast decision in a preliminary design setting. On the other hand, the continuum shell model is useful in detailed design phases, where computational efficiency can be partly traded for more precise behavioral predictions and insights on the failure of the matrix and fiber components.

## 7.2. Conclusions

The research questions formulated initially are briefly answered below, in view of the achievements and the limitations of the study.

*1. How can existing simulation frameworks be extended to achieve low computational cost and high accuracy of results in the depiction of the structural behaviour of CPVs?*

Previous numerical studies mainly focused on either very precise simulations of the vessel response, or on computational efficiency. The former came at high computational costs; the latter often led to inaccurate results. To mitigate both limitation, this study combines a series of analytical and numerical adjustments.

High accuracy is achieved by adjusting the vessel geometry and material composition analytically. This is meant to simulate the architecture of the filament wound CPV realistically. When these modifications are applied to the model, the prediction of the deformational behavior improves significantly as compared to previous frameworks. Discrepancies between the predicted and experimental outer tangential strains, for example, decrease from 13.6% to 6.3% for the BL configuration. The accuracy of the prediction increases even further when material degradation due to damage is included in the numerical analysis. For the same example, the discrepancy in outer tangential strains for the BL case further decreases to 2.1%, matching the experimental data remarkably. Similar trends are also found for the other investigated configurations.

Another numerical adjustment to increase the accuracy of the model is the refinement of the mesh, specifically increasing the through-thickness discretization. However, the impact of this adjustment is found to be rather limited. This suggests that the standard per-ply-group discretization implemented in the model already includes a sufficient number of integration points. Therefore, avoiding finer meshes is preferred to limit the computational expenses of the model.

High computational efficiency is achieved by reducing the model size drastically as compared to previous frameworks. In doing so, a series of modifications to the geometrical parameters and boundary conditions are implemented in Abaqus, which allow to reduce the amount of elements in the simulation without reducing its resolution. For instance, reducing the angle of revolution to 5 degrees leads to a reduction of computational time up to 83% with respect to the benchmark, which is based on a 90 degrees revolution.

Additionally, the full-parametrization and the automation of all pre- and post-processing steps speeds up the model generation and the data extraction significantly. This makes the modelling strategy interesting for further investigations.

### *2. Which parameters influence the simulated laminate response and how can these be adjusted to achieve a realistic prediction of the deformational behavior and burst of CPVs?*

Accounting for manufacturing effects is fundamental to simulate the behavior of CPVs during pressurization. Capturing the mechanical response of the vessel is only achievable through an accurate depiction of its geometry and material properties. In this sense, it is important that the properties of the simulated vessel match those of the manufactured CPV.

The cylindrical region is highly affected by the effects of compaction, which are neglected by the geometrical estimation provided by Composicad. Compaction influences both the geometry of the cylinder and its material properties. From a mere geometrical perspective, accounting for the reduced cylinder thickness allows to better capture the deformational behaviour of the vessel. However, the most substantial improvement is achieved when the material properties are adjusted per ply to account for the variable level of consolidation through the thickness. Not accounting for this effect leads to a drastic underestimation of the laminate stiffness, which leads to inaccuracies in the prediction of outer strains. Adjusting the strength properties accordingly is then necessary to prevent a premature burst estimation due to the higher stress levels.

The thickness reduction is less relevant in the dome region, where the compacting effect of the circumferential layers is not present. Here, another parameter is crucial. That is the thickness accumulation at the turnaround point of helical plies. This is particularly important for high angle helical plies, which contribute to the tangential stiffness of the dome region. Representing this thickness accumulation closely does not only allow to match the manufactured vessel shape, but also to avoid numerical instabilities in the prediction of outer strains. These instabilities mainly arise from the sudden and subsequent peaks in thickness estimated by Composicad, which translate into unrealistic local stiffnesses. Evaluating the relevance of the thickness accumulation of low angle helical plies is less intuitive, as the experimental data in this area becomes scattered and difficult to interpret. In any case, the depiction of the dome geometry requires further studies as multiple manufacturing effects are not taken into account in this investigation.

Another decisive aspect is the propagation of damage through the laminate. When the structure experiences damage, its load-carrying capabilities decrease. Although the relevance of this effect depends on the vessel configuration, an appropriate approximation of how damage initiates and evolves in the composite results into a more accurate depiction of the laminate behavior during pressurization. Furthermore, it sheds light on the failure sequence, facilitating the proper interpretation of the numerical results.

### *3. Based on the correlation between the observed vessel performance and the numerically simulated response, how accurately can burst pressure and failure location be predicted?*

The developed framework is able to predict burst both in the cylinder and in the dome. The prediction of cylinder failure is tested on the BL and BC configurations, which differ from each other only for stacking sequence. It is observed that the level of accuracy in the prediction of burst pressure depends on this difference. In fact, the model is able to estimate the burst pressure with an outstanding precision of 99.7% for the BC configuration. However, the accuracy is limited to 89.6% for the BL case. Although the framework includes some important adjustments of the material composition of the structure, it seems to not be fully able to reproduce all the effects that arise through the laminate during pressurization. As mentioned, the BL configuration is highly subjected to damage. This may lead to delaminations and other failure phenomena

which are not accounted for in the simulation.

The prediction of dome burst is tested on the W2B vessel configuration. The model provides a very accurate estimation of burst pressure, which deviates from the experimental result of only 1.2%. Furthermore, the failure location is predicted precisely, as first ply failure occurs in the dome region. The result is very promising as it proves that dome burst can be predicted to some extent, offering the possibility to minimize the use of material in this area. However, the model should be tested on a larger set of vessel configurations to prove its predictive ability. In addition, further insights on the dome material composition may lead to a further improvement of the prediction of dome burst. Specifically, the estimation of ply orientations in this area is still rudimentary, as well as the adjustment of the vessel contour in proximity of the boss neck.

*4. How can the developed tool be applied for design purposes, to simulate the deformational behavior and burst of CPVs?*

The model has a twofold potential. The solid element formulation allows to obtain reasonably accurate results at low computational costs. This is convenient within the automotive industry, where quick yet meticulous design decisions are needed at early stages of the development phase.

Despite providing a realistic depiction of the deformational behavior of the filament wound CPV, the solid model is not capable of reproducing the evolution of material properties during pressurization. Including such effects requires high computational time, especially for three-dimensional solid elements. The continuum shell element formulation provides a solution to this issue. In fact, the evaluation of material degradation due to damage is much more efficient for this element type. In this sense, the continuum shell model is complementary to the solid model, as it leads to very accurate results at relatively low computational costs. The second potential of the model becomes therefore apparent in the context of detailed design investigations, where more precise predictions are needed.

The convenience of the simulation tool also arises from its high replicability, definitely useful in design applications. This replicability is guaranteed by the full parametrization of the method, which allows to analyze different vessel configurations. Its ability to predict different failure types is an advantage, because it proves that the model can be widely applied regardless of the observed CPV behavior. Nevertheless, this statement requires further investigation, as effectively only a few configurations have been tested. In any case, the developed framework provides a solid basis for the analysis, which has the potential to lead to a significant reduction of composite mass especially in the dome region. Due to the complex geometry and material composition of this area, dome burst is difficult to predict and usually avoided at all costs. In turn, the vessel is often overdesigned, resulting in excessive material weight and high costs. Once the ability of the model to predict dome burst is proven, this may lead to a drastic reduction in local reinforcement, as the adequate amount of material required in the area would be more clear. For this reason, the developed modelling framework has a great potential for the optimization of CPV structures.

### 7.3. Recommendations for Future Research

The research presented in this document constitutes the conclusion of the work on CPVs done over the last few years first at Daimler AG and then at cellcentric GmbH. During this endeavor, the understanding of CPVs has deepened remarkably through several projects, spanning in content and application. Although the work of the research group is concluded, the work on CPVs most definitely is not. Therefore, a series of recommendations for future studies is provided.

#### **Insights on Dome Definition**

The dome is the least intuitive area of the vessel. Firstly, it is advised to perform more testing on vessel configurations that experience dome burst, to prove whether the tool is consistent in the prediction of this failure type. Despite the significant effort done throughout this study to capture some of the effects that lead to dome burst, this area of the vessel is still tedious to analyse. It is recommended to look more closely into the manufacturing effects that influence its geometry and material composition to achieve a thorough understanding of the dome. A more detail investigation on the ply orientations is needed to track how helical plies approach 90 degrees at their turnaround point. This would allow to better approximate the stiffness of this region. Furthermore, the thickness accumulation of low angle helical plies should be represented more accurately by taking into account the filament path and the respective diameter at the polar opening. The impact of these

parameters on the performance of the vessel is still largely not understood. Moreover, current adjustments of the local contour are based on experimental data, to match the simulated laminate to the profile obtained by means of stripe light projection. Trends relating the manufacturing variables to the vessel geometry should be found to guarantee a proper representation of the dome of CPVs consistently. Insights on these variables can potentially lead to a better understanding of the region, resulting in important reductions of material usage and costs.

#### **Estimation of Material Properties**

The analytical adjustment of material properties performed in this study shows that the material definition of the laminate is crucial in the determination of its mechanical response. The method, however, is an engineering approach. In future research a different adjustment methodology should be investigated, based on a physical reasoning. Furthermore, the adjustment should be extended to achieve a better representation of the material composition in the dome region. Here, the inaccuracy of the estimated ply orientations leads to uncertainties on the achieved level of compaction. Furthermore, a thorough experimental investigation on the porosity through the thickness in different areas of the vessel would shed light on the true composition of the laminate. Finally, the implementation of material degradation due to damage requires additional information on the energy released due to fracture, and on the composite resistance to damage propagation, i.e. the fracture toughness of its components. This data is taken from literature for the purpose of this investigation. It is therefore advised to conduct an experimental research to obtain more accurate properties, and to study how these affect the mechanical response of the CPV after damage initiation.

#### **Details on the Failure Behavior**

The numerical framework accounts for longitudinal and compressive failure of both the matrix and the fiber component. However, it neglects any effect such as bridging between fibers and delaminations, which may lead to higher compliance. Such effects can be accounted for by refining the analysis to a per-ply discretization and including cohesive elements between the different layers. Although on the one hand implementing these features would likely increase the computational expenses of the simulation, it would also capture additional failure mechanisms which are not limited to the investigated failure modes.

#### **Numerical Robustness in Damage Analysis**

Convergence issues are experienced when the effects of material degradation due to damage are included in the analysis. These are mainly caused by the large deformation encountered by some elements when these three conditions apply simultaneously: these elements are highly damaged; the load is applied directly on the nodes of these elements; these elements are placed in proximity of sudden change in stiffness. In turn, this results in high computational time. It is advised to perform a sensitivity analysis on the impact of preventing the large element deformations on the model stability. Furthermore, a mesh refinement study should be carried out to study the effects of a more gradual through-thickness stress gradient.

#### **Reduction of Computational Time**

One of the greatest achievements of the developed method is its computational efficiency. In fact, the model is built in such way to achieve an optimal combination between high accuracy and low computational time. Additional time reductions may be achieved with a thorough understanding of the numerical effects that cause instabilities during the analysis of damage propagation. Further investigations may be able to reduce the computational costs of the simulation even further by considering different numerical element formulations. A first attempt in this direction is made by generating the rudimentary axisymmetric model presented in Section 6.3, although a deeper investigation is needed.

#### **Development of an Optimized Layup**

The numerical framework is so far limited to pre-selected vessel configurations. The user input is in fact required to generate the initial geometry of the CPV in Compositcad. Ideally, a procedure which optimizes the vessel layup would be highly useful for the development of efficient CPVs. A valid approach would be to first calculate the structural requirements in terms of stiffness and strength along the vessel length. Then, to develop an analytical model to define an optimum layup which satisfies these structural requirements at each location. Finally, the optimized vessel would have to be translated into a winding sequence suitable for manufacturing. The model described in this document can then be used for verification, and to check the effects that tuning some of the manufacturing variables has on the optimized structure.

# A

## Appendix: Mesh Refinement Study

The simulation of damage propagation presented in Chapter 4 improves the prediction of the deformational behavior and the estimation of burst. However, its performance is dependent on the resolution of the model. For this reason, a mesh refinement study is performed to investigate the influence of a finer discretization on the results.

The BL vessel configuration is chosen for this investigation as it is the one that benefits the most from the inclusion of the damage progression analysis. Three configurations are chosen, which differ from each other in terms of through-thickness discretization. The number of elements through the group of low angle helical plies increases progressively to improve the resolution of both the cylindrical and the dome region of the vessel simultaneously. In any case, each solid of revolution only includes one ply type, to avoid sudden changes in stiffness within the same element:

- Original partition: it consists of a per-ply-group partition. This is the configuration analyzed so far in the report. It consists of 4 solids of revolution, one for each ply-group. This results in 4 elements through the thickness in the cylindrical region of the vessel, 2 reaching the boss neck.
- Partition A: it includes a double partition of low angle helical plies. In this case, the innermost group of low angle helical plies is split into 2 solids of revolution to increase the number of through-thickness elements in the cylindrical region to 5, and in the dome to 3.
- Partition B: it comprises a fine partition of low angle helical plies. The innermost group of low angle helical plies is split into 5 solids of revolution to increase the number of through-thickness elements in the cylindrical region to 8, and in the dome to 4.

The results of the three models are compared in terms of precision in the prediction of outer strains at 105 MPa internal pressure, accuracy in the estimation of burst pressure and computational efficiency.

The outer strain results are displayed in Figure A.1(a). The stress-state at 105 MPa is then used to predict the burst pressure, also shown in Figure A.1(a). In this case, Puck failure criterion is implemented according to a first ply failure approach, which assumes fiber tensile failure as cause of burst. The comparison in estimated burst pressure is presented in Table A.1.

Table A.1: Overview of predicted burst pressure for the three partitioning methods

	Predicted burst pressure	
	Pressure [MPa]	Discrepancy wrt experiment [%]
Original partition	180.5	10.4
Partition A	178.4	9.4
Partition B	176.9	8.6

Finally, a comparison in computational time is necessary to evaluate whether increasing the through-thickness partition of the geometry is beneficial, or, in other words, if the increased accuracy justifies the computational costs. The results are graphically depicted in Figure A.1(b).

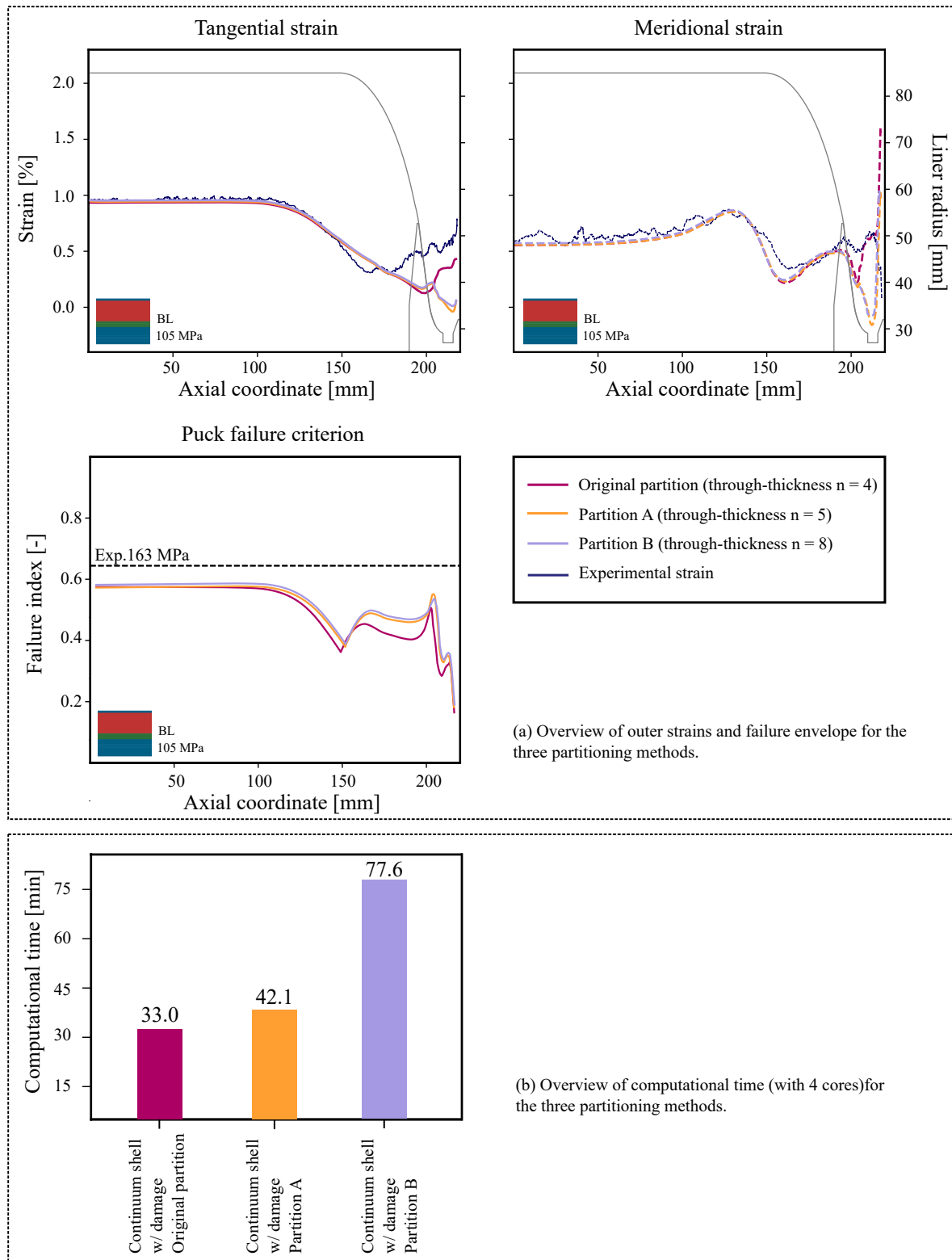


Figure A.1: Results of the mesh refinement study, including strains and failure envelope (a), and computational time (b).

In conclusion, increasing the through-thickness partition is beneficial as it reduces the discrepancy between simulation and experimental results. However, this comes at high computational costs, unjustifiable for this application. The per-ply-group discretization offers a reasonable compromise: it runs at relatively low computational time, and it leads to good accordance with the experimental data.



# B

## Appendix: Investigation on Matrix-Dominated Stresses

The hypothesis that at 105 MPa internal pressure the matrix has completely failed is presented in Chapter 5 as the reason for the decreased transverse and shear stresses obtained from the damage progression analysis. To verify whether this is truly the case, the stresses at lower pressure stages are investigated. If indeed the decrease in matrix-dominated stresses is due to the inclusion of damage, when the laminate is almost fully undamaged the stress-state should be similar for the constitutive elastic analysis and for the model that includes material degradation.

Figure B.1 shows the stress-state at 5 MPa resulting respectively from the solid model (which does not include any material degradation) and from the continuum shell model (without and with material degradation). Apart from the pressure levels and the magnitudes of the predicted ply stresses, Figure B.1 differs from Figure 5.7 because of the trend followed by the transverse and shear stresses. At low pressure levels, the matrix is fully able to carry these stresses. These have have similar trends for the two continuum shells models in Figure B.1. The differences with respect to the solid model are to attributed to the different formulation of solid and continuum shell elements described in Chapter 5. At high pressure level, on the other hand, the load-carrying capabilities of the matrix are compromised by the widely diffused tensile matrix failure. This reduces all matrix-dominated stresses in Figure 5.7, as the matrix is not able to withstand any loading.

In conclusion, the hypothesis is confirmed: at early stages of pressurization the two continuum shell models are equivalent, as both the matrix and the fiber constituents are able to the stresses which develop through the laminate. As the pressure increases, matrix tensile failure occurs and spreads widely. This decreases the load-carrying capabilities of the matrix, effectively decreasing the transverse and shear stresses that the laminate can withstand. For all investigated configurations, the matrix has almost fully failed in tension at already 55 MPa internal pressure, as shown in Chapter 5. Fiber failure, on the other hand, occurs later. Therefore, at 105 MPa the fiber constituent is still fully able to withstand the high longitudinal stresses. These actually increase, to mitigate the lack of reinforcement provided from the failed matrix.

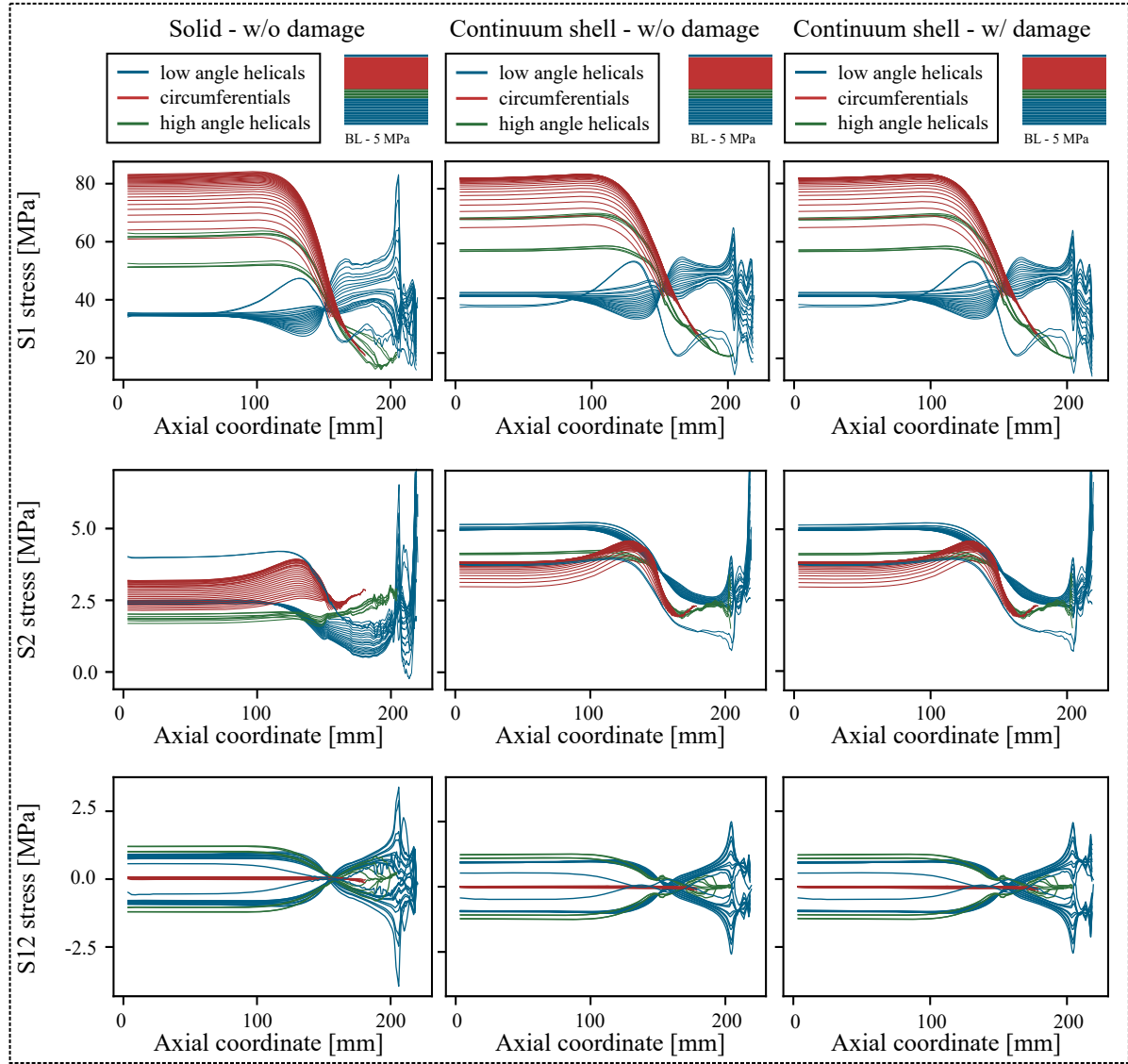


Figure B.1: Comparison of S1, S2 and S3 stresses at 5 MPa for the BL vessel configuration. Each column represents respectively the results obtained with the solid model (without damage) and the continuum shell model (without damage and with damage).

# C

## Appendix: Investigation on Per-ply Failure Indices and Considerations on Burst

The prediction of burst requires further interpretation. For this reason, the failure envelope obtained with the continuum shell model which considers material degradation is plotted again for the BL, BC and W2B configurations in Figure C.1, alongside with the per-ply failure indices according to Puck failure criterion for longitudinal tensile failure. Separate considerations are formulated for the three cases. These are similar to the ones presented in Chapter 5 for the solid model, although this time the achieved level of accuracy allows to dive more deeply into the results.

For the BL case, failure is predicted unambiguously in the cylinder, as here the entire stack of circumferential reaches the highest failure index. The prediction of burst pressure shows a discrepancy of 10.4% with respect to the experimental results, which can be attributed to several effects. Arguably the most relevant one is the high impact that damage has on the stack of inner helical plies, already explained in detail in chapter Chapter 5. In fact, after 105 MPa the degradation of material properties is not continued neglecting all inter- and intralaminar effects which may arise once the matrix has failed. As the approach followed for the calculation of the burst pressure only considered tensile fiber failure, these phenomena are completely excluded from the simulation.

The BC vessel, on the other hand, is less damaged. Here, the stack of circumferential plies is able to withstand the high tangential loads where they are highest. This allows to predict the burst pressure more accurately. However, the model does not give a clear interpretation of the burst location. A high peak in failure indices is found in the cylinder-dome transition region, suggesting that this would be the location of burst. Verifying experimentally whether this is the case is tedious, as burst occurs suddenly pulverizing the vessel. In any case, the per-ply failure indices provide interesting insights on the laminate behavior and allow to formulate some hypothesis. The high peak in failure index found in the cylinder-dome transition region is caused by the high loading of the single innermost low angle helical plies. Local failure of this thin layer, however, is unlikely to lead to the sudden burst observed experimentally. As the remaining low angle helical plies in the layup experience low levels of failure, they would probably be able to carry the loads that the failed ply cannot withstand. In this sense, load re-distribution would delay failure in this region at least for a short period of time, until the remaining low angle helical plies reach the critical failure index. Meanwhile, the stack of circumferential plies in the cylinder is also approaching failure due to the heavy tangential loading. It is likely that soon after the local failure of the innermost low angle helical ply in the cylinder-dome transition region, this group would reach the critical failure index. As the entire stack of circumferential plies is loaded similarly and shows almost equal failure indices, it would probably fail all at once, leading to a sudden burst in the central section of the cylinder. Although plausible, this hypothesis lacks however an experimental validation.

Finally, burst is undoubtedly predicted in the dome region for the W2B vessel, as a high peak which matches almost perfectly the experimental data is found in this region. As opposed to the BC configuration, this peak is approached by all the inner helical plies, reinforcing the hypothesis of dome burst. In this case, when the innermost low angle helical ply reaches the critical failure index, the surrounding plies are already very close to failure and are not able to carry the re-distributed stresses. This would most likely lead to the dome burst observed experimentally.

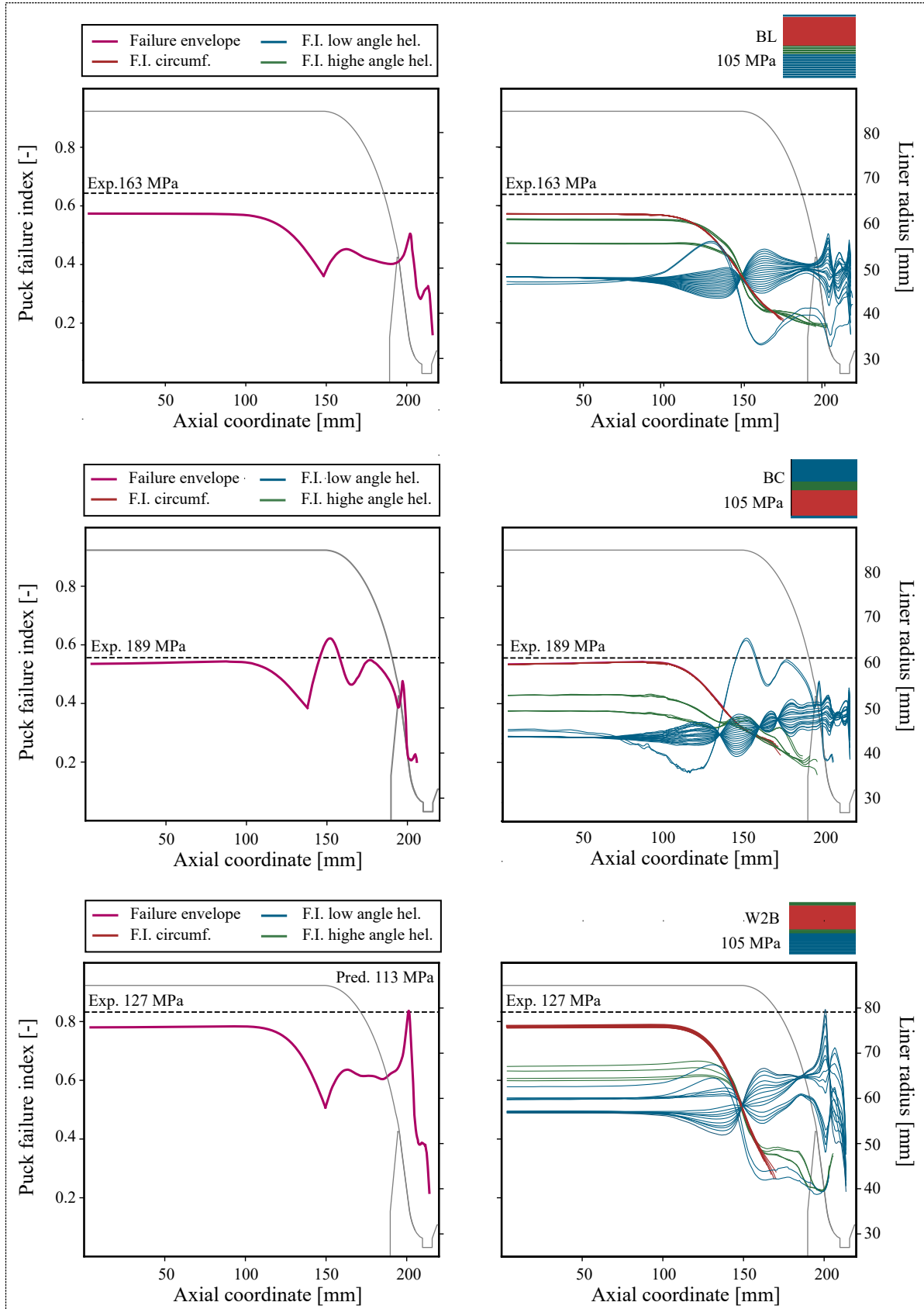


Figure C.1: Overview of failure envelopes and failure indices per-ply for the BL, BC and W2B configurations, according to the continuum shell (with damage).

# Bibliography

- [1] Pod Point UK. Tesla Model S (2019), June 2021. URL <https://pod-point.com/guides/vehicles/tesla/2019/model-s>.
- [2] United States Environmental Protection Agency. US Transportatin Sector - Greenhouse Gas Emissions 1990-2018. URL <https://nepis.epa.gov/Exe/ZyPDF.cgi?Dockey=P100ZK4P.pdf>.
- [3] M. Ehsani, Y. Gao, and A. Emadi. Modern electric, hybrid electric and fuel cell vehicles. *CRC Press, Boca Raton*, 2017.
- [4] E. Rivard, M. Trudeau, and K. Zaghib. Hydrogen storage for mobility: a review. *Materials, Multidisciplinary Digital Publishing Institute*, pages 1–22, June 2019. doi: 10.3390/ma12121973.
- [5] C. P. Fowler, A.C. Orifici, and C. H. Wang. A Review of toroidal composite pressure vessel optimization and damage tolerant design for high pressure gaseous fuel storage. *International Journal of Hydrogen Energy*, October 2017. doi: 10.1016/j.ijhydene.2016.10.039.
- [6] V. V. Vasiliev, A. A. Krikanov, and A. F. Razin. New generation of filament-wound composite pressure vessels for commercial applications. *Composite Structures*, 62(3-4):449–459, 2003. ISSN 02638223. doi: 10.1016/j.compstruct.2003.09.019.
- [7] The official blog of Toyota UK. Toyota Mirai: the safety facts, August 2015. URL <https://blog.toyota.co.uk/toyota-mirai-safety-facts/toyotablog-h2-safety-pict-n2>.
- [8] J. Franzen, S. Maus, and P. Potzel. Hydrogen storage in vehicles. In D. Stolten and B. Emonts, editors, *Hydrogen Science and Engineering*, pages 881–901. John Wiley & Sons, Incorporated, Berlin, Germany, 2016. ISBN 9783527674299.
- [9] H. Barthelemy, M. Weber, and F. Barbier. Hydrogen storage: recent improvements and industrial perspectives. *International Journal of Hydrogen Energy*, 42(11):7254–7262, 2017. ISSN 03603199. doi: 10.1016/j.ijhydene.2016.03.178.
- [10] M. Nebe. In-situ characterization methodology for the design and analysis of composite pressure vessels. *Technischen Universität Dortmund*, pages 5–6, 2020.
- [11] Switzerland. International Standards Organization, Geneva. Gas cylinders - high pressure cylinders for the on-board storage of natural gas as a fuel for automotive vehicles. 2013.
- [12] S. McWorther and G. Ordaz. Onboard type IV compressed hydrogen storage systems - current performance and cost: DOE fuel cell technologies office record 13010.
- [13] Economic Commission for Europe of the United Nations (UN/ECE). Regulation no 134, uniform provisions concerning the approval of motor vehicles and their components with regard to the safety-related performance of hydrogen fuelled vehicles.
- [14] EU 406/2010. Commission Regulation (EU) No 406/2010 of 26 April 2010 implementing Regulation (EC) No 79/2009 of the European Parliament and of the Council on type-approval of hydrogen-powered motor vehicles.
- [15] D. Leh, B Magneville, P. Saffré, P. Francescato, R. Arrieux, and S. Villalonga. Optimisation of 700 bar type IV hydrogen pressure vessel considering composite damage and dome multi-sequencing. *International Journal of Hydrogen Energy*, 40(38):13215–13230, 2015. ISSN 03603199. doi: 10.1016/j.ijhydene.2015.06.156.
- [16] S. T. Peters. *Composite Filament Winding*. ASM International, Materials Park, United States, 2010. ISBN 9781615038527.

- [17] F. Schen. A filament-wound structure technology overview. *Materials Chemistry and Physics*, 42(2): 96–100, February 1995. doi: 10.1016/0254-0584(95)01554-X.
- [18] S. Pandita, N. Shotton-Gale, and M. Shafiq Irfan. Clean wet-filament winding - Part 1: design concept and simulations. *Journal of Composite Materials*, 47(3):379–390, February 2013. doi: 10.1177/0021998312440474.
- [19] S. Koussios and A. Beukers. Filament winding: design, materials, structures and manufacturing processes. *Wiley Encyclopedia of Composites*, 2(2):1–16, 2012.
- [20] D. Cohen, S. C. Mantell, and L. Zhao. The effect of fiber volume fraction on filament wound composite pressure vessel strength. *Composites Part B: Engineering*, 32(5):413–429, 2001. ISSN 13598368. doi: 10.1016/S1359-8368(01)00009-9.
- [21] D. Leh, P. Saffré, P. Francescato, and R. Arrieux. Multi-sequence dome lay-up simulations for hydrogen hyper-bar composite pressure vessels. *Composites Part A: Applied Science and Manufacturing*, 52:106–117, 2013. doi: 10.1016/j.compositesa.2013.05.007.
- [22] L. Zu, S. Koussios, and A. Beukers. Design of filament-wound domes based on continuum theory and non-geodesic roving trajectories. *Composites Part A: Applied Science and Manufacturing*, 41(9):1312–1320, 2010. doi: 10.1016/j.compositesa.2010.05.015.
- [23] L. Zu, S. Koussios, and A. Beukers. Design of filament-wound isotenoid pressure vessels with unequal polar openings. *Composites Part A: Applied Science and Manufacturing*, 92(9):2307–2313, 2010. doi: 10.1016/j.compstruct.2009.07.013.
- [24] S. Koussios, O.K. Bergsma, and A. Beukers. Filament winding: determination of the wound body related parameters. *Composites Part A: Applied Science and manufacturing*, 35(2):181–195, 2004.
- [25] C. C. Liang, H. W. Chen, and C. H. Wang. Optimum design of dome contour for filament-wound composite pressure vessels based on a shape factor. *Composite Structures*, 58(4):469–482, 2002. ISSN 02638223. doi: 10.1016/S0263-8223(02)00136-8. URL [https://doi.org/10.1016/S0263-8223\(02\)00136-8](https://doi.org/10.1016/S0263-8223(02)00136-8).
- [26] R. Wang, W. Jiao, W. Liu, and F. Yang. Slippage coefficient measurement for non-geodesic filament-winding process. *Composites Part A: Applied Science and Manufacturing*, 43(3):303–309, 2011. doi: 10.1016/j.compositesa.2010.12.002.
- [27] J. De Cavalho, M. Lossie, D. Vandepitte, and H. van Brussel. Optimization of filament wound parts based on non-geodesic winding. *Composites Manufacturing*, 6(2):79–84, 1995.
- [28] R. Wang, W. Jiao, W. Liu, and F. Yang. A new method for predicting dome thickness of composite pressure vessels. *Journal of Reinforced Plastics and Composites*, 29(22):3345–3352, 2010. ISSN 0731-6844. doi: 10.1177/0731684410376330.
- [29] L. Zu, H. Xu, H. Wang, B. Zhang, and B. Zi. Design and analysis of filament-wound composite pressure vessels based on non-geodesic winding. *Composite Structures*, 207:41–52, 2019. ISSN 02638223. doi: 10.1016/j.compstruct.2018.09.007.
- [30] P. Mertiny and F. Ellyin. Influence of the filament winding tension on physical and mechanical properties of reinforced composites. *Composites: Part A*, 33(12):1615–1622, October 2002. doi: 10.1016/S1359-835X(02)00209-9.
- [31] C. Kang, Y. Shi, B. Deng, T. Yu, and P. Sun. Determination of residual stress and design of process parameters for composite cylinder in filament winding. *Advances in Materials Science and Engineering*, 2018, January 2018. doi: 10.1155/2018/1821342.
- [32] A. Johman. MSc Thesis on the Development of a Computationally Efficient Modelling Framework for Type IV Pressure Vessels. *Technical University of Delft*, January 2021.
- [33] H. Fukunaga and M. Uemura. Optimum design of helically wound composite pressure vessels. *Applied Science Publishers Ltd.*, 1(1):31–49, 1983. ISSN 0018-9219. doi: 10.1016/0263-8223(83)90015-6.

- [34] M. Hojjati, V. Safavi Ardebili, and S. V. Hoa. Design of domes for polymeric composite pressure vessels. *Composites Engineering*, 5(1):51–59, 1995. doi: 10.1016/0961-9526(95)93979-6.
- [35] M. Madhavi. Design and analysis of filament wound composite pressure vessel with integrated-end domes. *Defence Science Journal*, 59(1):73–81, 2009. doi: 10.14429/dsj.59.1488.
- [36] L. Wang, C. Zheng, S. Luo, S. Wei, and Z. Wei. Continuum damage modeling and progressive failure analysis of carbon fiber/epoxy composite pressure vessel. *Composite Structures*, 134:475–482, 2015. doi: 10.1016/j.compstruct.2015.08.107.
- [37] L. Wang, C. Zheng, S. Wei, and Z. Wei. Micromechanics-based progressive failure analysis of carbon fiber-epoxy composite vessel under combined internal pressure and thermomechanical loading. *Composites Part B: Engineering*, 89:77–84, 2016. ISSN 13598368. doi: 10.1016/j.compositesb.2015.11.018.
- [38] B. Magneville, B. Gentilleau, S. Villalonga, F. Nony, and H. Galiano. Modeling, parameters identification and experimental validation of composite materials behavior law used in 700 bar type IV hydrogen high pressure storage vessel. *International Journal of Hydrogen Energy*, 40(38):13193–13205, 2015. doi: 10.1016/j.ijhydene.2015.06.121.
- [39] S. Lin, Yang L., Xu H., Jia X., Yang X., and Zu L. Progressive damage analysis for multiscale modelling of composite pressure vessels based on Puck failure criterion. *Composite Structures*, 225, 2020. ISSN 113046. URL <https://doi.org/10.1016/j.compstruct.2020.113046>.
- [40] P. Balicevic, D. Kozak, and T. Mrcela. Strength of pressure vessels with ellipsoidal heads. *Journal of Mechanical Engineering*, 54(10):685–692, 2008.
- [41] J.M. Whitney. On the use of shell theory for determining stresses in composite cylinders. *Journal of Composite Materials*, 5(340):340–353, January 1971. ISSN 03080161. doi: 10.1177/002199837100500304.
- [42] B. W. Tew. Preliminary design of tubular composite structures using netting theory and composite degradation factors. *Journal of Pressure Vessel Technology*, 117, 1995. doi: 10.1115/1.2842141.
- [43] R. M. Gheshlaghi, M. H. Hojjati, and H. R. M. Daniali. Analysis of composite pressure vessels. *Springer, Dordrecht*, 2006. doi: 10.1007/1-4020-4972-2\_165.
- [44] D. K. Roylance. Netting analysis for filament-wound pressure vessels. *Composites division army materials and mechanics research center*, Technical Report. AAMMRC TN 76-3, 1976.
- [45] R. A. Chaudhuri, K. Balaraman, and V. X. Kunukkasseril. Admissible boundary conditions and solutions to internally pressurized thin arbitrarily laminated cylindrical shell boundary-value problems. *Composite Structures*, 86:385–400, January 2008. doi: 10.1016/j.compstruct.2007.12.008.
- [46] L. Parnas and N. Katirci. Design of fiber-reinforced composite pressure vessels under various loading conditions. *Composite Structures*, 58(1):83–95, 2002. ISSN 02638223. doi: 10.1016/S0263-8223(02)00037-5.
- [47] C. Kassapoglou. *Design and analysis of composite structures*. John Wiley and Sons Ltd, May 2013. ISBN 978-1-1185-3693-3. doi: 10.1002/9781118536933.
- [48] H. Fukunaga and M. Uemura. Coupling effect in laminated composite cylinder under internal pressure. *Journal of the Society of Materials Science, Japan*, 28(315):1146–1152, 1979.
- [49] M. Xia, H. Takayanagi, and K. Kemmochi. Analysis of multi-layered filament-wound composite pipes under internal pressure. *Composite Structures*, 53(4):483–491, 2001. ISSN 02638223. doi: 10.1016/S0263-8223(01)00061-7.
- [50] L. Zu, J. Wang, and S. Li. Analysis of multi-layered thick-walled filament-wound hydrogen storage vessels. *International Journal of Hydrogen Energy*, 39(36):21083–21096, 2014. ISSN 03603199. doi: 10.1016/j.ijhydene.2014.10.075.
- [51] P. Seide and R. A. Chaudhuri. Triangular finite element for analysis of thick laminated shells. *International Journal for Numerical Methods in Engineering*, 24(8):1563–1579, 1987.

- [52] D. S. Son and S. H. Chan. Evaluation of modeling techniques for a type III hydrogen pressure vessel (70 MPa) made of an aluminum liner and a thick carbon/epoxy composite for fuel cell vehicles. *International Journal of Hydrogen Energy*, 37(3):2353–2369, 2012. doi: 10.1016/j.ijhydene.2011.11.001.
- [53] D. Leh, P. Saffré, P. Francescato, R. Arrieux, and S. Villalonga. A progressive failure analysis of a 700-bar type IV hydrogen composite pressure vessel. *International Journal of Hydrogen Energy*, 40(38):13206–13214, 2015. ISSN 03603199. doi: 10.1016/j.ijhydene.2015.05.061.
- [54] J. P. Berro Ramirez, D. Halm, J. C. Grandidier, S. Villalonga, and F. Nony. 700 bar type IV high pressure hydrogen storage vessel burst – Simulation and experimental validation. *International Journal of Hydrogen Energy*, 40(38):13183–13192, 2015. ISSN 03603199. doi: 10.1016/j.ijhydene.2015.05.126.
- [55] A. S. Soriano. MSc Thesis on Analysis Strategies for As-Manufactured Composite Pressure Vessels. *Technical University of Delft*, August 2020.
- [56] F. A. Leone, A. C. Bergan, and C. G. Davila. CompDam - Deformation Gradient Decomposition (DGD). v2.5.0, 2019. URL [https://github.com/nasa/CompDam\\_DGD](https://github.com/nasa/CompDam_DGD).
- [57] M. Nebe, T. J. Asijee, C. Braun, J. M. J. F. Van Campen, and F. Walther. Experimental and analytical analysis on the stacking sequence of composite pressure vessels. *Composite Structures*, 2020. doi: 10.1016/j.compstruct.2020.112429.
- [58] N. S. Reddy. Theory and analysis of elastic plates and shells. *CRC Press*, 2007.
- [59] ISO 527-4:1997. *Plastics - Determination of tensile properties - Part 4: Test conditions for isotropic and orthotropic fiber-reinforced plastic composites*. ISO/TC 61/SC 13 Composites and reinforcement fibres, 1997.
- [60] ISO 14129:1997. *Fibre-reinforced plastic composites - Determination of the in-plane shear stress/shear strain response, including the in-plane shear modulus and strength, by the plus or minus 45 degrees tension test method*. ISO/TC 61/SC 13 Composites and reinforcement fibres, 1997.
- [61] Z. Hashin and A. Rotem. A fatigue criterion for fiber-reinforced materials. *Journal of Composite Materials*, 7:448–464, 1973.
- [62] M. R. Abir, M. Ridha, T.E. Tay, and H. Lee. On the relation between failure mechanism and compression after impact (CAI) strength in composites. *Composite Structures*, 182:242–250, 2017. doi: 10.1016/S1359-8368(99)00067-0.